

**Physical Conditions in the Broad Line Region of $z \sim 3$
Quasars:
A Photoionization Method to Derive r_{BLR} and M_{BH} ♣**

C. Alenka Negrete¹ and Deborah Dultzin¹

Instituto de Astronomía, Universidad Nacional Autónoma de México, Mexico

Paola Marziani²

INAF, Astronomical Observatory of Padova, Italy

and

Jack Sulentic³

Instituto de Astrofísica de Andalucía, Spain

Received _____; accepted _____

To appear in ...

⁰Based on observations made with ESO Telescopes at Paranal Observatory under programme ID 078.B-0109(A)

¹anegrete@astroscu.unam.mx, deborah@astroscu.unam.mx

²paola.marziani@oapd.inaf.it

³sulentic@iaa.es

ABSTRACT

We present high S/N UV spectra for eight quasars at $z \sim 3$ obtained with VLT/FORS. The spectra enable us to analyze in detail the strongest emission features in the rest-frame range 1400-2000 Å of each source (CIII]λ1909, SiIII]λ1892, AlIIIλ1860, SiIIλ1814, CIVλ1549 and SiIVλ1397). Previous work indicates that a component of these lines is emitted in a region with well-defined properties i.e., a high density and low ionization emitting region). Flux ratios AlIIIλ1860/ SiIII]λ1892, CIVλ1549/AlIIIλ1860, SiIVλ1397/ SiIII]λ1892, CIVλ1549/SiIVλ1397 and SiIIλ1814/ SiIII]λ1892 for this region permit us to strongly constrain electron density, ionization parameter and metallicity through the use of diagnostic maps built from CLOUDY simulations. Reliable estimates of the product density times ionization parameter allow us to derive the radius of the broad line region r_{BLR} from the definition of the ionization parameter. The r_{BLR} estimate and the assumption of virialized motions in the line emitting gas yields an estimate for black hole mass. We compare our results with estimates obtained from the $r_{\text{BLR}} - \text{luminosity}$ correlation customarily employed to estimate black hole masses of high redshift quasars.

Subject headings: galaxies: active — galaxies: high-redshift — quasars: general — quasars: emission lines

1. Introduction

1.1. Interpreting Quasar Spectra

Measuring relevant physical parameters from the observed broad-line spectra of quasars is still an open challenge. Identification and intensity measurements of the strongest emission lines has made possible a rough inference of the typical conditions of the emitting gas since the earliest days of quasar spectroscopy. The very first quasars of intermediate redshift discovered in the 1960s showed a fairly high ionization spectrum, with prominent lines of C IV λ 1549, and He II λ 1640 in addition to strong Balmer lines of the low-redshift quasars. Photoionization by the central continuum source was considered the preeminent heating mechanism of the emitting gas. Significant C III] λ 1909 emission suggested electron densities (n_e) in the range $10^9 - 10^{10} \text{ cm}^{-3}$. The observed intensity ratio C III] λ 1909/C IV λ 1549 indicated ionization parameter (defined by Eq. 1 later in this paper) values of the order of 10^{-1} . This photoionization scenario was successful in explaining at least some quasar optical and UV spectra (see the review by Davidson and Netzer 1979 for a synopsis). More recent work emphasized the existence of several problems with this simple scenario. Low ionization lines (LILs), and especially Fe II are too strong to be explained by a photoionized region of moderate density and column density (see for example Dumont and Mathez 1981; Joly 1987; Collin-Souffrin et al. 1988; Dumont and Collin-Souffrin 1990). These authors stressed that the LILs required a denser, low-temperature environment.

We unfortunately lack a simple well-defined diagnostic measure of physical conditions in the broad line region. One strategy for estimating electron density

in astrophysical sources involves using two emission lines of the same ion, and with similar energies above the ground level, but with different radiative transition probabilities A_{ki} . In practice one often chooses two lines from the same term where one forbidden/semi-forbidden transition is associated with another that is semi-forbidden/permitted in order to ensure very different values of A_{ki} (for example, [SiII] λ 1882 and [SiII] λ 1892). This technique is not straightforwardly applicable to the broad lines of quasars, precisely because the lines are broad, suitable candidates are too closely spaced in wavelength, and density is at least an order of magnitudes higher than the critical density for the forbidden transitions used in spectra of planetary nebulae and HII regions. In addition the S/N and the resolution of quasar spectra are usually not very high.

Feibelman and Aller (1987) used the CIII] λ 1909/ [SiII] λ 1892 ratio to study the rather high-density environment typical of symbiotic stars ($n_e \sim 10^{7-10} \text{ cm}^{-3}$). In this case we have two semi-forbidden (intercombination) resonance lines with significantly different transition probabilities (see Table 1). The lines are emitted by two iso-electronic species with somewhat different ionization potentials (11 eV for C⁺ vs. 8 eV for Si⁺). The ionic fraction is dependent on the relative abundance of silicon-to-carbon (to be assumed) as well as on the ionization structure within the emitting region (to be computed). Using lines of different ions introduces additional potentially serious sources of uncertainty. It is perhaps not surprising that most workers believe that n_e in the BLR cannot be reliably estimated using quasar spectra. Strong CIII] λ 1909 emission would imply that n_e cannot be very high ($n_e \sim 10^{11-13} \text{ cm}^{-3}$). Very high density was invoked to explain the rich low ionization spectrum (especially FeII) seen in the spectra of most quasars. Several

lines in the UV spectrum of I Zw 1 point towards high density at least for the LIL emitting zone: prominent FeII, relatively strong AlIII λ 1860, and detection of CIII λ 1176 (Baldwin et al. 1996; Laor et al. 1997b). The region where these lines are produced cannot emit much CIII] λ 1909. But is CIII] λ 1909 really so strong in most quasars? BLR conditions are certainly complex and a single emitting region is not sufficient to explain both LILs and high ionization lines (HILs).

1.2. Quasar Systematics

Quasar spectra are not all alike. There are significant differences in line intensity ratios and broad line profiles from object to object (Bachev et al. 2004; Marziani et al. 2010). More importantly, these differences can be organized in a systematic way as has been realized since the early 1990s (Boroson and Green 1992). Since then several authors stressed the importance of the so-called eigenvector 1 (E1) of quasars (e.g. Gaskell et al. 1999). Sulentic et al. (2000, 2007) expanded the E1 trends into a 4-dimensional space involving optical, UV and X-ray measures. They also defined spectral types along a sequence occupied by AGN in an optical plane involving FeII and FWHM H β parameters. Objects at extreme ends of the E1 sequence are very different at almost all wavelengths and median spectra computed in spectral bins within this plane emphasize systematic changes in broad line properties (Sulentic et al. 2002, 2007). The differences have motivated the suggestion of a possible dichotomy between Narrow Line Seyfert 1 (NLSy1s) like sources and broader line objects that include almost all radio-loud quasars. The most effective divider of the two quasar types appears to be at FWHM of the H β

broad component $H\beta_{\text{BC}} \approx 4000 \text{ km s}^{-1}$ for low-to-moderate luminosity sources (Marziani et al. 2009). This corresponds to Eddington ratio $L/L_{\text{Edd}} \sim 0.2 \pm 0.1$ (Marziani et al. 2003b).

The distinction between NLSy1-like objects (hereafter Population A sources with $\text{FWHM}(H\beta) \leq 4000 \text{ km s}^{-1}$) and the rest of quasars (Population B with $\text{FWHM}(H\beta) \gtrsim 4000 \text{ km s}^{-1}$) is of special relevance here. Pop. A sources show relatively low equivalent width lines with e.g. the $\lambda 1900$ blend $\sim 30 \text{ \AA}$. A close analysis of the $\text{CIII}] \lambda 1909$ blend in the prototypical NLSy1 I Zw 1 shows strong $\text{SiIII}] \lambda 1892$, and $\text{AlIII} \lambda 1860$ blended with rather weak $\text{CIII}] \lambda 1909$ along with prominent $\text{FeIII}(\text{UV34})(\lambda 1895.5, \lambda 1914.0, \text{ and } \lambda 1926.3)$ and FeII blends (Laor et al. 1997b; Vestergaard and Wilkes 2001). The $\text{CIII}] \lambda 1909$ line is apparently so weak that $\text{FeIII} \lambda 1914$ may be the most prominent feature at $\lambda \approx 1910 \text{ \AA}$ (cf. Hartig & Baldwin 1986). This interpretation is confirmed by detailed deblending of a source (SDSS J120144.36+011611.6) that can be considered a high luminosity analog of I Zw 1 (§7.1).

Median composite UV spectra of low- z quasars show that $\text{AlIII} \lambda 1860$ and $\text{SiIII}] \lambda 1892$ are more prominent in 4DE1 spectral types A2 and A3. Bins A1, A2, A3 are defined in terms of increasing $\text{FeII} \lambda 4570$ (see Fig. 1 of Sulentic et al. 2002). I Zw 1, although belonging to the extreme type A3 (Bachev et al. 2004) is not unique as a NLSy1, since the fraction of Pop. A sources in bin A3 and A4 is $\approx 20 \%$ of all Pop. A sources in the sample of Zamfir et al. (2010). A significant number of extreme NLSy1 are not classified as quasars in SDSS and must be collected from the

galaxy catalog (Hu et al. 2008).

1.3. Emission Line Diagnostics and BLR Properties

Emission lines and line ratios are used in diagnostic maps to estimate temperatures and electronic densities in galactic and extragalactic photoionized regions. Examples include HII-regions and galaxies with HII-region nuclear spectra where electron densities are less than $n_e \approx 10^4 \text{ cm}^{-3}$. This method has been successfully applied to the narrow line region (NLR) in AGN. Application to the broad line quasars has yielded results that are difficult to interpret. One recent exception is the work by Matsuoka et al. (2008) who succeeded in analyzing the partly ionized region thought to emit most of the LILs in quasar spectra. They suggest that OI 8446 and the CaII triplet are emitted by dense, low ionization gas probably located in the periphery of the BLR. If the electron density and ionization conditions are known it is possible to derive, with additional assumptions, the distance of the BLR emitting region from the central continuum source (as stressed earlier also by Baldwin et al. 1996).

The physical conditions of photoionized gas can be described by electron density n_e , hydrogen column density N_c , metallicity (normalized to solar), shape of the ionizing continuum, and the ionization parameter U . The latter represents the dimensionless ratio of the number of ionizing photons and the electron density n_e or, equivalently, the total number density of hydrogen n_H , ionized and neutral.¹

¹In a fully ionized medium $n_e \approx 1.2 n_H$. We prefer to adopt the definition based on n_H because

Both U and n_{H} are related through the equation

$$U = \frac{\int_{\nu_0}^{+\infty} \frac{L_{\nu}}{h\nu} d\nu}{4\pi n_{\text{H}} c r^2} \quad (1)$$

where L_{ν} is the specific luminosity per unit frequency, h is the Planck constant, ν_0 the Rydberg frequency, c the speed of light, and r can be interpreted as the distance between the central source of ionizing radiation and the line emitting region. Note that $U n_{\text{H}} c$ is the ionizing photon flux

$$\Phi(H) = \frac{Q(H)}{4\pi r^2}. \quad (2)$$

If we know *the product of* n_{H} and U , we can estimate the radius r of the BLR from Eq. 1. The dependence of U on r_{BLR} was used by Padovani & Rafanelli (1988) to derive central black hole masses assuming a plausible average value of the product $n_{\text{H}} \cdot U$. The typical value of n_{e} was derived at that time from semiforbidden line CIII] λ 1909 which implied that the density could not be much higher than $n_{\text{e}} \approx 10^{9.5} \text{ cm}^{-3}$ (Osterbrock & Ferland 2006). Padovani (1988) derived an average value $\langle U \cdot n_{\text{e}} \rangle \approx 10^{9.8}$ from several sources where r_{BLR} had been determined from reverberation mapping, and for which the number of ionizing photons could be measured from multiwavelength observations. The average value was then used to compute black hole masses for a much larger sample of Seyfert 1 galaxies and low- z quasars (Padovani & Rafanelli 1988; Padovani, Burg & Edelson 1989). Wandel, Peterson & Malkan (1999) compared the results of the photoionization method with the ones obtained through reverberation mapping, found a very good correlation

it is the one employed in the CLOUDY computations.

for the masses computed with the two methods, and concluded that “both methods measure the mass of the central black hole.”

1.4. Outline of the paper

The importance of the product $U \cdot n_{\text{H}}$ goes beyond knowledge of the physical conditions in the BLR if it can lead to estimates of BLR radius and black hole mass. This paper identifies suitable emission line ratios that overcome some of the major problems in the analysis of emission lines of quasars. It also defines a photoionization method that can be applied to even the highest redshift quasars making use of high S/N near-IR spectroscopic data. In §2 we present the spectra of 8 pilot sources obtained with the VLT/FORS; in §3 we discuss data reduction; In §4 we describe our method of fitting broad emission line profiles; in §5 we give a phenomenological interpretation of the profile fits; in §6 we describe a method for deriving BLR physical conditions and give the results of our fits; in §7 we discuss two sources not belonging to our sample that show extreme behavior and that are helpful to understand more common quasar spectra; in §8 we give the results for the photoionization method; in §9 we derive the radius of the BLR (its distance from the ionizing source) and the mass of the black hole for each quasar in our sample; in §10 we discuss our results; finally, in §11 we summarize our results and the prospect of a more extended application of our method. All the computations were made considering $H_0 = 70 \text{ km s}^{-1} \text{ Mpc}^{-1}$ and a relative energy density $\Omega_{\Lambda} = 0.70$ and $\Omega_{\text{M}} = 0.3$.

2. Observations

Data were obtained between Nov. 2006 and Jan. 2007 using the VLT2/FORS1 telescope operated in service mode. FORS1 is the visual and near UV focal reducer and low dispersion spectrograph of the Very Large Telescope (VLT) operated by European Southern Observatory (ESO) (Appenzeller et al. 1998). Our VLT sample consists of 8 quasars with $z \sim 3$. In Figure 1 we show the spectra uncorrected for redshift. Tab. 2 provides a log of observations that is organized as follows.

Column 1: object name, Col. 2: apparent B magnitude, Col. 3 redshift, Col. 4: line(s) used for redshift estimation: a) $\text{O I } \lambda 1304.8$, b) $\text{C III }]\lambda 1909$; Col. 5: absolute B magnitude, Col. 6 flux at 6 cm taken from FIRST (Far InfraRed and Submillimetre Telescope), Col. 7: date (refers to time at start of exposure), Col. 8: Digital Integration Time, Col. 9: number of exposures with integration time equal to DIT, Col. 10: airmass at the beginning of each exposure, Col. 11 S/N in the continuum around 1700\AA .

The observation of one of our 8 quasars, J00521-1108, yielded only a low S/N spectrum which we retain because observed features in the blend at $\sim 1900\text{\AA}$ are clear enough to fit the individual lines. Two sources, J01225+1339 and J02287+0002, are BAL quasars. We will keep them separate because $\text{C IV } \lambda 1549$ is severely affected by absorption.

3. Data Reduction

Data were reduced using standard IRAF tasks. All spectra were wavelength and flux calibrated in the observed frame and then corrected for Galactic extinction. Flux correction was applied using meteorological data provided by ESO. The observed flux was multiplied by the inverse of the light lost computed from the ratio seeing over slit width in arcsec. Correction to rest frame requires estimating the redshift z which is not a trivial task as outlined below. Rest frame correction also involved scaling the specific flux in flux per unit wavelength interval by a factor $(1 + z)^3$. Measurements were carried out on the rest-frame spectra. It is necessary to describe below two important aspects of the data reduction.

3.1. A & B Atmospheric Bands Correction

The A or B atmospheric band falls on top of the 1900Å blend in many of the spectra. This is an important region for this study especially because it involves SiIII]λ1892, AlIIIλ1860, and SiIIλ1814. In order to remove these absorption features we created an A+ B band template from standard star spectra used as specific flux calibrators. We scaled this template to find a best fit. Fig. 1 shows the A and B absorption correction where we make a line identification to illustrate which lines are affected. In cases where the A or B bands overlap a weak line like SiIIλ1814 the effect is considerable and measures of SiIIλ1814 should not be considered at all or with extreme care. This happens for sources J00103-0037, J03036-0023, and J20497-0554. In cases where one of the bands overlaps a stronger line like

SiIII] λ 1892 or AlIII λ 1860, the correction was good enough to permit accurate measures.

3.2. Redshift Estimate

Normally one uses strong narrow emission lines to set the rest frame in a quasar. In our case no strong narrow lines are available so we consider the peaks of Ly α , CIV λ 1549 and CIII] λ 1909. The Ly α peak is affected by absorption and CIV λ 1549 is a HIL feature often showing blueshifts and/or asymmetries (Gaskell 1982, Espey et al. 1989, Corbin 1990, Tytler & fan 1992; Marziani et al. 1996; Richards et al. 2002, Baskin & Laor 2005; Sulentic et al. 2007). This is especially true in Pop. A sources. CIII] λ 1909 is blended with SiIII] λ 1892 and FeIII that is especially prominent in this region and could well affect the peak. Pop. B sources show a rather weak Fe spectrum making the CIII] λ 1909 peak a more reliable z estimator.

Our best option is to use the low ionization line OI λ 1304 whenever it is strong. However it is blended with low ionization SiII $\lambda\lambda$ 1304,1309 ($^2P_{3/2,1/2}^0 - ^2S_{1/2}$). Both OI λ 1304 and SiII $\lambda\lambda$ 1304,1309 are broad lines and in Pop. B sources might show large redshifts or even significant blueshifts. Simulations in the (n_H, U) region of interest show OI λ 1304 \approx 2 SiII λ 1304,1309 and this is confirmed in the spectrum I Zw 1 where OI λ 1304 and SiII $\lambda\lambda$ 1304,1309 are resolved. The two components of the SiII $\lambda\lambda$ 1304,1309 doublet are set to the same intensity (i.e., we assume an optically thick case). We model the blend OI λ 1304 + SiII $\lambda\lambda$ 1304,1309 with 5 Gaussians; the three components of the OI feature are produced by Bowen fluorescence mechanism,

and should show ratios consistent with their transition probabilities. Generating a model spectrum in IRAF (lines broadened to 4000 km s^{-1}) yields a rest frame peak wavelength of $1304.8 \pm 0.2 \text{ \AA}$ (in vacuum) which we use as a reference for our VLT spectra assuming that there is no hint of systematic BC shifts as is the case for all Pop. A sources (the majority in our sample) and many Pop. B sources (Marziani et al. 2003a).

Examination of Fig. 2 reveals that the peak of $\text{OI}\lambda 1304$ in source J00521-1108 is not observed clearly. We use $\text{CIII}] \lambda 1909$ to set the rest frame in this case. There are other sources J00103-0037, J02287+0002, J02390-0038 and J20497-0554 where the redshift estimation using both $\text{OI}\lambda 1304$ and $\text{CIII}] \lambda 1909$ are not in good agreement. The largest disagreement was found for J02287+0002. Redshifts obtained for the three remaining quasars, J01225+1339, J03036-0023 and J23509-0052, were obtained from $\text{OI}\lambda 1304$. Fig. 3 shows the deredshifted VLT-FORS spectra for our sample of 8 quasars.

4. Data Analysis

4.1. Methodological Considerations on Multicomponent Fits

The SPECFIT IRAF task (Kriss 1994) allows us to fit the continuum, emission and absorption line components, FeII and FeIII blends, etc. We fit two spectral ranges: (1) $1450\text{--}1680 \text{ \AA}$ for analysis of $\text{CIV}\lambda 1549$ and (2) $1750\text{--}2050 \text{ \AA}$ for analysis of the 1900 \AA blend. Significant FeII and FeIII emission are expected close to and underlying the 1900 \AA blend. Study of the 1900 \AA blend is especially difficult in

quasars because the lines are broad and the blending severe. We therefore need to take advantage of several previous results.

4.2. FeII and FeIII Emission

Our approach is completely empirical and employs an FeII + FeIII template taken from templates successfully used in previous works. Our FeII template is based on a CLOUDY simulation and is not very far from the preferred model of Bruhweiler & Verner (2008).

FeIII lines are common and strong in the vicinity of CIII] λ 1909 as is evidenced by their presence in average LBQS (Francis et al. 1991) and SDSS (Vanden Berk et al. 2001) spectra. They appear to be strong when AlIII λ 1860 is also strong (Hartig and Baldwin 1986). Vestergaard & Wilkes (2001) produced an FeIII template based on the UV spectrum of IZw 1. Since then, Sigut et al. (2004) have modeled the FeIII BLR spectrum. See also Verner et al. (2003) for a plot of emission around 1900 Å. Ly α pumping enhances FeIII (UV 34) λ 1914.0 (Johansson et al. 2000) and this line can be a major contributor to the blend right on the red side of CIII] λ 1909 (see Fig. 2 of Vestergaard & Wilkes). We reproduced the option B of the empirical FeIII template of Vestergaard & Wilkes (2001), taking advantage of the line identifications from Ekberg (1993). When detected we can use FeII UV 191 to set a rough FeII level while the feature at 2080 Å is helpful for a more precise estimation of the intensity of FeIII. The continuum was fitted using the regions around 1450Å (1750 and 1960Å) that are relatively free of FeII emission (Vanden Berk et al. 2001). We used the same power-law to describe the continuum at both

the C^{IV}λ1549 and 1900Å regions.

4.3. Line Components

We base our SPECFIT analysis on several previous observational results. The most important ones are as follows:

- Sulentic et al. (2002) gridded the broad component of FWHM $H\beta_{BC}$ versus $R_{FeII} = W(FeII\lambda4570blend)/W(H\beta_{BC})$ parameter plane into bins of fixed Δ FWHM = 4000 km s⁻¹ and $\Delta R_{FeII} = 0.5$. Quasar spectra in different bins are different in many measures. As mentioned earlier, the largest differences are found between NLSy1-like objects, Pop. A, and broader sources of Pop. B with FWHM($H\beta$) \gtrsim 4000 km s⁻¹. The gridding of Sulentic et al. (2002) is valid for low z (<0.7) quasars. At higher z an adjustment must be made since no sources with FWHM $H\beta_{BC} < 3500$ km s⁻¹ exist above luminosity $\sim 10^{48}$ ergs s⁻¹ (Marziani et al. 2009).
- Median spectra were computed for spectral bins from the atlas of Marziani et al. (2003a) who found that $H\beta$ can be described by a Lorentz function in Pop. A sources and by the sum of 2 Gaussians in Pop. B sources (unshifted + broader redshifted components) (Zamfir et al. 2010; Marziani et al. 2010).
- A careful FeII subtraction reveals a blue-shifted $H\beta$ component in some bin A3 sources (i.e. the strongest FeII emitters; Zamfir et al. 2010).
- C^{IV}λ1549 (HIL) and $H\beta$ (LIL) profiles show significant differences in Pop.

A. Large $\text{CIV}\lambda 1549$ blueshifts ($\lesssim -1000 \text{ km s}^{-1}$) are observed in Pop. A *only* (Sulentic et al. 2007). HIL and LIL profiles are more similar in Pop. B sources.

- We do not have $\text{H}\beta$ observations for our high- z objects since there are no near IR spectra. We use the results of Marziani et al. (2003b, 2010): they show that the BC of $\text{SiIII}\lambda 1892$, $\text{AlIII}\lambda 1860$ and $\text{CIV}\lambda 1549$ lines is similar to the one of $\text{H}\beta$, including the FWHM and profile shape, either Gaussian or Lorentzian. The similarity helps us to define whether an object is Population A or B in this paper.

These observational results point toward three different components in broad line profiles (see Marziani et al. 2010) which can be described as follows:

1. A broad component (BC) showing a roughly symmetric profile with FWHM in the range $1000\text{-}5000 \text{ km s}^{-1}$. It is consistent with the component identified by Matsuoka et al. (2008). This broad component dominates LILs in Balmer lines of Pop. A sources while it becomes less prominent in Pop. B. The profile is best modeled by a Lorentzian function in Pop. A sources while Pop. B profiles are better described by a Gaussian (Marziani et al. 2003b).
2. A very broad component (VBC), as seen in LILs and HILs of most pop B sources but is absent from Pop. A profiles. The VBC can be modeled as a Gaussian ($\text{FWHM} \sim 10000 \text{ km s}^{-1}$) often with a significant shift to the red. It can be called a defining property of Pop. B sources (Marziani et al. 2010). **This component is clearly identified in the $\text{CIV}\lambda 1549$ line of Pop. B**

objects, and is also appreciable on the red side of $\text{CIII}\lambda 1909$ of Pop. B objects J00103-0037 and J02390-0038.

3. A blueshifted broad component (BBC), defined as the residual emission in the $\text{CIV}\lambda 1549$ line after subtracting a scaled BC Lorentzian profile (Marziani et al. 2010). This blueshifted component is often prominent in $\text{CIV}\lambda 1549$ and $\text{Ly}\alpha$ of Pop. A sources. It is much less intense in radio-loud Pop. B sources (Marziani et al. 1996; Punsly 2010; Richards et al. 2010). We model this profile as a blueshifted Gaussian. The Gaussian approximation is probably inappropriate especially if the BBC is strong: this component is believed to be produced in a partially-obscured radial flow, not in a virialized emitting system. **In the present work we do not even try to fit the blueshifted in the doubly ionized lines. It is quite obvious from the fits that a possible contribution of this component would be negligible.**

Baldwin et al. (1996) presented a similar analysis. Their Fig. 2 organizes spectra in a sequence that is roughly corresponding to E1, going from $\text{AlIII}\lambda 1860$ -strong sources to objects whose spectra show prominent $\text{CIII}\lambda 1909$ along with weak $\text{AlIII}\lambda 1860$ (Bachev et al. 2004). Two of the three line components they isolated correspond to the ones we consider in this paper: a blue-shifted feature, and a more symmetric, unshifted and relatively narrow component that we call LIL-BC. Less obvious is the correspondence of a third feature, although it appears to be the redshifted part of what we call the VBC.

Several improvements have been introduced since the paper of Baldwin et al. 1996. These improvements are expected to make our analysis easier. First, the definition of a template of FeIII emission (Vestergaard & Wilkes 2001), along with the possibility to model FeII in the 1400–2000 Å spectral region with CLOUDY (Verner et al. 1999, 2004). The analysis of spectra along the E1 sequence allows one to see trends that make the interpretation of the emission line blends easier (Marziani et al. 2010).

4.4. Expected emission from the various components

We looked for evidence of three possible components as described above: BC, VBC and BBC only for the most intense HILs: C IV λ 1549 and Si IV λ 1397. We did not include the contributions of the BBC for the doubly-ionized lines. In the case of Pop. A sources, we indeed assume that the BC contains the vast majority of the light. In the case of Pop. B sources we consider the contribution of the VBC. The Al III λ 1860 doublet shows no evidence of either a BBC or VBC. There is no obvious BBC for Si III] λ 1892 in the blend. There is evidence of a VBC of C III] λ 1909 extending on the red side of the blend, and this is taken into account. Moreover, we expect that the Al III λ 1860 doublet is emitted exclusively in the BC, the region where Fe II is also emitted. This is empirically confirmed by the aspect of the 1900 blend in many sources, where we do not see any evidence of BBC nor VBC. We remark that the

$\text{Al III } \lambda 1860$ doublet is relatively unblended, and that a BBC feature as strong as in $\text{C IV } \lambda 1549$ would not easily escape visual detection. The same is also true for $\text{Si III } \lambda 1892$. Several fits that included BBC in $\text{C III } \lambda 1909$ yielded 0 intensity, implying a large $\text{C IV } \lambda 1549 / \text{C III } \lambda 1909$ (Marziani et al. 2010). The $\text{Si IV } \lambda 1397 + \text{O IV } \lambda 1402$ blend closely resembles the shape of $\text{C IV } \lambda 1549$, suggesting that BBC is relevant, especially for $\text{Si IV } \lambda 1397$ ($\text{O IV } \lambda 1402$ is expected to give a minority contribution to line emission at the high density derived for the BC; any $\text{O IV } \lambda 1402$ contribution to the BBC is not relevant to our method). BBC is very weak or undetectable in the vast majority of the $\text{H}\beta$ profiles analyzed in Marziani et al. 2010 (but see Zamfir et al. 2010 for several cases of $\text{H}\beta$ BBC), while prominent in $\text{Ly}\alpha$; the $\text{Ly}\alpha / \text{H}\beta$ ratio in this component is high. In summary, BBC is visually strong in $\text{Ly}\alpha$, $\text{C IV } \lambda 1549$, and $\text{Si IV } \lambda 1397$. $\text{He II } \lambda 1640$ in BBC is needed for a self-consistent fit of the $\text{C IV } \lambda 1549 + \text{He II } \lambda 1640$ blend. The VBC of $\text{Si III } \lambda 1892$ is poorly constrained, but in the fits where $\text{C III } \lambda 1909$ VBC is visible, we always find $\text{Si III } \lambda 1892 < \text{C III } \lambda 1909$, consistent with the high ionization level expected in the VBC region. Some $\text{Si IV } \lambda 1397$ VBC emission is assumed in the Pop. B fits. No VBC emission is expected in $\text{Al III } \lambda 1860$ and Fe II . These constraints help also to make the fits less ambiguous.

The absence of a VBC makes the decomposition of Pop. A spectra easier. As said earlier, the Fe II intensity scale of the template (but Fe II is in general weak) is anchored to the UV 191 intensity; similarly the Fe III intensity is set by a feature external to the 1900 Å blend (2080

Å). There is no evidence of BBC of $\text{Al III } \lambda 1860$ and $\text{Si III } \lambda 1892$; the $\text{Al III } \lambda 1860$ doublet profile is mostly unblended and defines the LIL-BC. The additional complication here is the $\text{Fe III } \lambda 1914$ line whose intensity is affected by $\text{Ly}\alpha$ pumping. Since the shift and FWHM are assumed the same for all lines (and templates) in the 1900 blend, the only free parameters in addition to shift and FWHM are the intensities of 6 components, including the two from the templates, and $\text{Si III } \lambda 1814$ and $\text{Al III } \lambda 1860$ that are not heavily blended. The `SPECFIT` analysis is especially helpful to measure in a non-subjective way, taking all constraints into account, the two parameters that are most affected by the blend: the intensity of $\text{Si III } \lambda 1892$ and $\text{C III } \lambda 1909$ (we repeat that any $\text{Fe III } \lambda 1914$ contribution in excess to the one of the adopted template is included in the estimated $\text{C III } \lambda 1909$ intensity).

In the case of Pop B, the presence of a VBC does not really complicate the fit as a matter of fact. The $\text{C III } \lambda 1909$ line undeniably shows a VBC protruding on the red side of the 1900 blend. In any case, considering that we can expect the VBC to be assimilable to a shifted Gaussian with $\text{FWHM} \sim 10000 \text{ km s}^{-1}$, the unblended part of the $\text{C III } \lambda 1909$ VBC provides a strong constraint. The $\text{Si III } \lambda 1892$ VBC is certainly the most difficult feature to ascertain, as it is buried under $\text{Si III } \lambda 1892$ and $\text{C III } \lambda 1909$ emission. We rely on the `SPECFIT` results, that indicate negligible $\text{Si III } \lambda 1892$ VBC.

4.5. Errors

We identify five sources of error from the conditions for data reduction and methodological considerations described above:

1. A & B atmospheric bands correction (already described in §3.1).
2. Line profile shape, Gaussian or Lorentzian (Pop. A or B). The distinction between Pop. A and B is based on line width with the boundary at FWHM $H\beta \approx \text{km s}^{-1}$ in low luminosity quasars and around $\approx 5000 \text{ km s}^{-1}$ at higher luminosity such as the eight sources presented here. Most of our quasars are unambiguously Pop. A or B because of line width and because Pop. B sources show an $H\beta$ VBC and pop A sources a prominent $\text{CIV}\lambda 1549$ BBC. In these cases only one profile shape (Gaussian or Lorentzian) was fitted.
3. Rest-frame determination using $\text{OI}\lambda 1304$ or $\text{CIII}] \lambda 1909$. In some cases the redshift estimates derived from the two lines do not agree, most likely because of absorptions present in $\text{OI}\lambda 1304.8$ and because this is not a very intense line. The principal impact of uncertainty in the rest frame placement is estimation of the peak wavelength of $\text{CIV}\lambda 1549$. If the line peak differs from $\lambda 1549\text{\AA}$, the BC intensity is diminished and we infer a greater contribution from the blue (BBC) component. Similarly, for the blend 1900\AA , the rest frame shift may increase or decrease our estimate for the strength of $\text{CIII}] \lambda 1909$ with consequent decrease or increase of the $\text{SiIII}] \lambda 1892$ contribution. This additional source of uncertainty affects J00103-0037, J02287+0002 and J20497-0554.

4. FeII intensity (continuum placement). Broad FeII emission can produce a pseudo-continuum affecting our estimates of emission line intensities. SiII λ 1814 is especially affected in our spectra because it is weak. AlIII λ 1860 is similarly affected when it is weak. The effect is less noticeable for CII λ 1549 since expected FeII emission underlying the CII λ 1549 line is weak also for strong FeII emitters.
5. Broad absorption lines (BALs) in quasars principally affect the blue side of CII λ 1549. We also find an absorption feature between FeII λ 1787 and SiII λ 1814 (eg. Fig. 6). In sources J01225+1339 and J02287+0002 we can only set upper limits for line intensities (since we fit unabsorbed components).

There are other sources of error such as small BC shifts and FWHM variations. We assume that the BC of the SiII λ 1892, AlIII λ 1860, SiII λ 1814 and CII λ 1549 line has the same FWHM and wavelength shift, although we allow for variations in their relative flux strengths and adopted profile type (Lorentzian for Pop. A and Gaussian for Pop. B). For FeIII(UV34) and FeII we slightly relax this constraint. The FeIII(UV34) and FeII emission is not very strong and the FWHM of individual features is poorly constrained by SPECFIT. In the case of CIII λ 1909 we need to consider the possibility that the profile is narrower because there might be a contribution from different regions: indeed, the SPECFIT routine usually converges toward a narrower profile if the CIII λ 1909 width is not constrained. The effect depends on the strength of the FeIII λ 1914 feature.

The goal of this study is to estimate diagnostic line ratios. A posteriori, we can say that the estimated line ratios are rather insensitive to the emission component profile shape: assuming a Gaussian or Lorentzian profile yields the same ratio for the strongest lines (i.e., C^{IV} λ 1549, Si^{III} λ 1892, Al^{III} λ 1860) upon which our analysis is based (with an uncertainty of $\sim 10\%$). The same conclusion applies to the redshift uncertainty. Only in the case of J02287+0002 the redshift difference produces a significant effect due to a $\Delta z \approx 0.16$. However, we adopt the fit based on O^I λ 1304: the alternative fit produces line ratios that are of not obvious interpretation and at variance with respect to the other sources. The most serious sources of error remain effects of A/B band overlap for Si^{III} λ 1814 and the presence of a BAL for C^{IV} λ 1549.

5. Results of Line Component Analysis on Individual Objects

In Figures from 4 to 6 we show our best fits for the VLT sample taking into account the considerations described in §4. The fits of Si^{IV} λ 1397 are shown in Fig. 7 and the intensity values and equivalent widths are in Tables 3 and 5. We present here a phenomenological description of the fits. **The line profiles, intensities and line ratios usually follow the trends of Pop. A or B sources, although in some objects there are features that are ambiguous (for example the line shape). In these cases however, we have assigned Pop. A or B type on the basis of the FWHM (see Cols. 5 and 6 of Table 7).**

5.1. Pop. A Objects

- J03036-0023 – We estimate for this source a $\text{FWHM(BC)} \sim 3700 \text{ km s}^{-1}$ and we use a Lorentzian function to fit the broad lines. The peak of $\text{CIV}\lambda 1549$ is blueshifted and requires a strong BBC (Fig. 4(a)). The bump on the red side of $\text{CIV}\lambda 1549$ can be accounted for by $\text{HeII}\lambda 4686$ BC and BBC. There is no evidence for a red shifted component in $\text{CIII}\lambda 1909$ (Fig. 4(b)). $\text{AlIII}\lambda 1860$ is prominent. Unfortunately the blue wing of $\text{SiII}\lambda 1814$ and the red wing of $\text{FeII}\lambda 1787$ are affected by A band absorption.
- J20497-0554 – This source shows $\text{FWHM(BC)} \sim 3800 \text{ km s}^{-1}$. As for J03036-0023, the $\text{CIV}\lambda 1549$ line can be accounted for by an unshifted BC (assumed Lorentzian) of a considerably contribution of a BBC (Fig. 4(c)). We see a prominent $\text{AlIII}\lambda 1860$ line and $\text{FeII}\lambda 1787$ (Fig. 4(d)). $\text{SiIII}\lambda 1892$ is affected by several narrow absorption lines; however, it is obviously strong. The lack of a red wing on $\text{CIII}\lambda 1909$ suggests that no VBC is present.
- J23509-0052 – This source has $\text{FWHM(BC)} \sim 3600 \text{ km s}^{-1}$. $\text{CIV}\lambda 1549$ shows a slight blue asymmetry with a BBC (Fig. 4(e)) required to model it. The contribution of FeII is small and $\text{FeII}\lambda 1787$ is weak (Fig. 4(f)). $\text{CIII}\lambda 1909$ is very strong. $\text{AlIII}\lambda 1860$ is affected by A band absorption; the profile we fit is probably an upper limit. This object could well belong to spectral type A1 that includes Pop. A sources with the lowest $R_{\text{FeII}} (\lesssim 0.5)$.

5.2. Pop. B Objects

- J00103-0037 – This source has a $\text{FWHM(BC)} \sim 4500 \text{ km s}^{-1}$. The red side of $\text{CIV}\lambda 1549$ is blended with $\text{HeII}\lambda 4686$. Fitting a BC with no shift plus a BBC to $\text{CIV}\lambda 1549$ leaves a very large residual on the red side. A very broad redshifted component (VBC) is needed to model the spectrum (Fig. 5(a)). The faint narrow line under $\text{CIV}\lambda 1549$ can be explained as the narrow component (NC) of $\text{CIV}\lambda 1549$ (see Sulentic et al. 2007). The presence of a similar NC in $\text{CIII}\lambda 1909$ could possibly explain the large residual seen ~ 1900 . We specifically note the prominent $\text{CIII}\lambda 1909$ emission and weak (but detected) $\text{AlIII}\lambda 1860$ (Fig. 5(b)). The FeII “bump” at 1787 \AA (UV 191) is appreciable. Fainter FeII emission is relatively unimportant because FeII creates a pseudo-continuum. $\text{SiII}\lambda 1814$ is compromised by A-band absorption. The blend at 1900 \AA includes a $\text{CIII}\lambda 1909$ VBC and the fit indicates $\text{CIV}\lambda 1549 / \text{CIII}\lambda 1909 \text{ (VBC)} \approx 7$ which is reasonable.
- J00521-1108 – This source shows the noisiest spectrum in the sample. We fit a $\text{FWHM(BC)} \sim 5300 \text{ km s}^{-1}$ with $\text{CIV}\lambda 1549$ requiring a large VBC to account for the red wing. (Fig. 5(c)). Absorption features seriously affect the $\text{CIV}\lambda 1549$ profile. The profile of $\text{CIII}\lambda 1909$ is strongly asymmetric due to some sort of absorption on the red side. $\text{AlIII}\lambda 1860$ is weak consistent with pop. B (Fig. 5(d)).
- J02390-0038 – This object has a somewhat atypical Pop. B spectrum due to a

very strong BBC in C IV $\lambda 1549$ (Figure 5(e)). This source has a $\text{FWHM(BC)} \sim 5400 \text{ km s}^{-1}$. Consistent with pop. B we find Fe II $\lambda 1787$ to be weaker than Si II $\lambda 1814$. C III] $\lambda 1909$ is flat topped and has a very similar intensity as Si III] $\lambda 1892$. Both C IV $\lambda 1549$ and C III] $\lambda 1909$ it show red wings indicating VBC emission. The A band absorption lies between Si III] $\lambda 1892$ and Al III $\lambda 1860$ (Fig. 5(f)) producing a possible overestimation of Al III $\lambda 1860$.

5.3. BAL QSOs

- J01225+1339 – C IV $\lambda 1549$ is highly affected by two broad absorption lines (Fig. 6(a)) with blueshifts of 5200 and 10800 km s^{-1} at peak absorption with equivalent widths/FWHM $-12\text{\AA} / 3900 \text{ km s}^{-1}$ and $-25\text{\AA}/5200 \text{ km s}^{-1}$, respectively. The blueshift of the C IV $\lambda 1549$ peak leads us to suspect a large blueshifted BBC emission component. The 1900 \AA blend shows absorptions coincident with Fe II $\lambda 1787$ and the blue side of Si II $\lambda 1814$ which is however unambiguously detected (Fig. 6(b)). Al III $\lambda 1860$ is prominent which implies that this a Pop. A source. The $\text{FWHM(BC)} \sim 4400 \text{ km s}^{-1}$ is consistent with a high-luminosity Pop. A source. **It is also possible that this BAL QSO is an outlier like Mark 231 at low- z (Sulentic et al. 2006), in other words an extreme Pop. A object.** The C III] $\lambda 1909$ is well fitted with a Lorentzian profile. Broad A band atmospheric absorption lies over Si III] $\lambda 1892$.
- J02287+0002 – This object has a very complex spectrum. On one side it has a $\text{FWHM(BC)} \approx 4700 \text{ km s}^{-1}$ **which is typical of low-luminosity Pop. B**

and the lines profiles are better fitted with Gaussians. On the other side, however, it shows features that are typical of extreme Pop. A sources: prominent $\text{FeII}\lambda 1787$, strong $\text{AlIII}\lambda 1860$, no $\text{CIII}\lambda 1909$ VBC (Fig. 6(d)). Considering that the FWHM limit between Pop. A and B is increasing with luminosity, the FWHM(BC) is within the limit of Pop. A. The $\text{CIII}\lambda 1909$ line is not very flat topped but the similar intensities of $\text{CIII}\lambda 1909$ and $\text{SiIII}\lambda 1892$ remind the case of J02390-0038. Also because it has a strong blue-shifted component in $\text{CIV}\lambda 1549$ atypical to Pop. B objects (Fig. 6(c)).

The estimated rest frame of this quasar differs by $\sim 1400 \text{ km s}^{-1}$ using $\text{OI}\lambda 1304$ and $\text{CIII}\lambda 1909$. This is the largest discrepancy in our sample. In order to evaluate the effect of the z discrepancy we performed two fits using both rest frames. Figs. 6(a) and (b) use the $\text{CIII}\lambda 1909$ restframe. In the 1900 \AA blend, we found a contribution of $\text{SiIII}\lambda 1892$ similar to $\text{CIII}\lambda 1909$. If we use the $\text{OI}\lambda 1304$ inferred rest frame we show in Figs. 6(e) and (f) that $\text{CIII}\lambda 1909$ becomes stronger with a resultant decrease of $\text{SiIII}\lambda 1892$. A similar effect occurs for $\text{CIV}\lambda 1549$ broad and blue-shifted components.

The $\text{CIV}\lambda 1549$ BAL shows a blueshift of 9100 km s^{-1} at deepest absorption, a EW of -14 \AA and a FWHM of 4600 km s^{-1} .

Summing up, we are able to assign an A/B identification to all sources in our sample. The two BAL QSOs appear as objects of extreme Pop. A. We remind that the identification of $\text{CIII}\lambda 1909$ in the BAL QSOs and in sources with strong $\text{AlIII}\lambda 1860$ is debatable (Hartig and

Baldwin 1986): strong FeIII 1914 could take the place of most CIII] λ 1909 emission.

6. Estimation of Physical Conditions in the Emitting regions

6.1. CLOUDY Simulations

We computed a multidimensional grid of CLOUDY (Ferland et al. 1998) simulations, (see also Korista et al. 1997) to derive U and n_{H} from our spectral measurements. Simulations span the density range $7.00 \leq \log n_{\text{H}} \leq 14.00$, and $-4.50 \leq \log U \leq 00.00$, in intervals of 0.25. Each simulation was computed for a fixed ionization parameter and density assuming plane parallel geometry. The 2D grid of simulations was repeated twice assuming $N_{\text{c}} = 10^{23}$ and 10^{24} cm^{-2} . Several cases were computed also for $N_{\text{c}} = 10^{25} \text{ cm}^{-2}$. Metallicity was assumed to be either solar or five times solar. Two alternative input continua were used: 1) the standard AGN continuum of CLOUDY which is equivalent to the continuum described by Mathews and Ferland (1987) and 2) the low- z quasar continuum of Laor et al. (1997a). Computed line ratios are almost identical for fixed (U , n_{H}). However the ionizing luminosity differs by more than a factor of 2 for a fixed specific continuum luminosity. The contour plots showing the distributions of CIII] λ 1909/ SiIII] λ 1892, AlIII] λ 1860/ SiIII] λ 1892, SiII] λ 1814/ SiIII] λ 1892, **SiIV] λ 1397/ SiIII] λ 1892**, CIV] λ 1549/AlIII] λ 1860 and CIV] λ 1549/ SiIII] λ 1892 (Fig. 9) are generated from $29 \times 19 = 551$ simulations and assume a standard set of simulations using a Mathews and Ferland (1987) continuum, $N_{\text{c}} = 10^{23} \text{ cm}^{-2}$, and

solar metallicity. The CLOUDY 08.00 computations included a model of the Fe^+ ion with 371 levels. The UV FeII template, described in §4.2 is based on a suitable CLOUDY simulation. Even if a relationship is very likely between the dense low ionization gas producing our diagnostic lines and FeII emission (supported observationally) our diagnostics do not use any FeII computation. The weak line $\text{OI}\lambda 1304$ is used only for rest frame estimation and not for diagnostic considerations.

Apart from the hypothesis of plane-parallel geometry, no inferences are made about the actual distribution, location, and kinematics of the line emitting gas. The assumption of constant density is crude. If gas is distributed in clouds then magnetic confinement appears to be unnecessary to avoid cloud dispersion from pressure imbalance or cloud shear associated with a hot confining medium. Magnetic confinement could make density uniform within the cloud (Rees 1987; Bottorff and Ferland 2000).

6.2. Intermediate Ionization Lines in the Blend at $\lambda 1900$

The ratio $\text{CIII}\lambda 1909 / \text{SiIII}\lambda 1892$ is density dependent because the transition probabilities of the two lines are so different: 114 s^{-1} vs 12600 s^{-1} (see Table 1). The forbidden lines at 1883\AA and 1907\AA have such low transition probabilities that they are collisionally quenched at much lower density and will not be considered. Line ratios like $\text{CIII}\lambda 1909 / \text{SiIII}\lambda 1892$ are useful diagnostics in a rather narrow range of density which depends on the transition probabilities. Above the critical density, emission lines originating from forbidden or semi-forbidden transitions become collisionally quenched, and hence weaker than lines for which collisional effects are

still negligible. CIII] λ 1909 is clearly unsuitable as a diagnostic for $n_e \gg 10^{11} \text{ cm}^{-3}$, as the CIII] λ 1909/ SiIII] λ 1892 $\rightarrow 0$. Feldman et al. (1992) gives critical density of SiIII] λ 1892 $n_e \sim 2 \cdot 10^{11} \text{ cm}^{-3}$. AlIII] λ 1860 is a permitted transition with large transition probability ($A \sim 5 \cdot 10^8 \text{ s}^{-1}$) and has very-high critical density (i.e., its equivalent width goes to zero toward thermodynamic equilibrium, which occurs at very high density, when all line emission is collisionally quenched). Our 2D array of CLOUDY simulations shows that the ratio AlIII] λ 1860/ SiIII] λ 1892 is well suited to sample the density range $10^{10} - 10^{12.5} \text{ cm}^{-3}$. Within this range the SiIII] λ 1892 intensity decreases smoothly by a factor 10; above the upper limit in density, the predicted intensity of SiIII] λ 1892 decreases. This corresponds to the densest, low ionization emitting regions likely associated to the production of FeII.

Intermediate-ionization lines such as CIII] λ 1909, AlIII] λ 1860, SiIII] λ 1892 and SiIV] λ 1397 avoid the issue of collisional ionization (**invoked for the production of low-ionization species by S. Collin and collaborators, as mentioned in the introduction**).

The widely separated doublet AlIII] λ 1860 is expected to be produced entirely in the fully ionized zone (Laor et al. 1997b). CLOUDY simulations confirm this suggestion. Figure 10 (top panel) shows the ionic fraction as a function of the geometrical depth in a cloud (or slab) of fixed column density ($N_c = 10^{23} \text{ cm}^{-2}$) and density ($n_H = 10^{12.5} \text{ cm}^{-3}$). As it can be seen, Al^{++} , Fe^{++} , and Si^{++} share a region of dominance deep in the cloud, close to the end of the Strömgren sphere. Beyond, in the partially-ionized zone (PIZ) there is, as by definition, a significant fraction of ionized hydrogen. The dominant ionic stages of Si and Fe become Fe^+

and Si^+ . It is very appropriate to consider the $\text{AlIII}\lambda 1860 / \text{SiIII}\lambda 1892$ ratio since the two lines are apparently emitted in the very same zones within the gas slab. Available reverberation mapping results may support this interpretation but are rather difficult to extrapolate since they are limited to a handful of low luminosity objects. **The main finding is that $\text{CIII}\lambda 1909$ responds to continuum changes on timescales much longer than $\text{CIV}\lambda 1549$ and other HILs.** This results comes from the analysis of total $\text{CIII}\lambda 1909 + \text{SiIII}\lambda 1892$ in NGC 3783 (Onken & Peterson 2002), from the $\text{CIII}\lambda 1909$ of NGC 4151 (Metzroth et al. 2006) and of NGC 5548. It is intriguing that the $\text{CIII}\lambda 1909$ cross-correlation delay in NGC 5548 (by far the best studied object) is even larger than that of $\text{H}\beta$ (32 ld vs. 20 ld; Peterson et al. 2002; Clavel et al. 1991). For fixed density, lines of higher ionization form at higher photon flux. The C^+ , Al^+ , Si^+ ionization potential are 24, 18, and 16 eV respectively. These comparable ionization potentials are well below the one of HILs, $X^{i-1} \gtrsim 50$ eV. However, the much lower $\text{CIII}\lambda 1909$ critical density implies that the $\text{CIII}\lambda 1909$ line should be formed farther out than $\text{SiIII}\lambda 1892$ and $\text{AlIII}\lambda 1860$ if all these lines are produced under similar ionization conditions.

6.3. The SiII Contribution to the UV Spectrum of Quasars

AGN have a rather rich singly-ionized silicon spectrum in the range 1000-2000 Å, due to several resonant transitions from the ground term $3s^23p^1P^0$ to terms associated to the $3s^13p^2$ ($\lambda 1814$ and $\lambda 1304$), $3s^24s$ ($\lambda 1531$), $3s^23d$ ($\lambda 1263$) electronic

configurations. A feature on the red side of $\text{Ly}\alpha$, at 1263 \AA is detected in several Pop. A sources like I Zw 1 (Marziani et al. 2010).

The $\lambda 1309$ feature is partially blended with the OI triplet associated with a Bowen fluorescence mechanism from $\text{HI Ly}\beta$. The $\lambda 1309$ line is well resolved in sources like I Zw 1 with the extension of the broad $\lambda 1309$ feature suggesting significant SiII emission around $\lambda 1309$. The $\lambda 1531$ feature is blended with $\text{CIV}\lambda 1549$. High S/N spectra of low redshift sources from HST (Laor et al. 1994) as well as for quasars at $z \approx 4$ (Constantin et al. 2002) indicate that the feature is very weak in most sources.

The SiII feature at $\lambda 1814$ is detected in at least four of the five quasars studied by Laor et al. (1994). In the 6 objects used for the E1 sequence of Marziani et al. (2010), it is detected without reasonable doubt in I Zw 1 only. However this has to do more with the poor S/N of the 1900 \AA region than of anything else; good S/N HST spectra show an unambiguous detection in Akn 120 and Mark 509, for example. Early detection of the UV SiII lines from IUE observations suggested collisional excitation and no relevant fluorescence effects (as observed in type Ia supernovæ; Dumont and Mathez 1981). Fluorescence effects and recombination are revealed by optical lines which are emitted through several cascade routes to the ground state. However, a median spectrum of A2 quasars with $S/N \approx 200$ (Zamfir et al. 2010) barely detects any expected emission feature in the range $4000\text{--}6500 \text{ \AA}$. The prominence of the $\lambda 1814$ feature may then be associated to the relatively low temperature believed to exist in the innermost part of the line emitting “cloud”, $T_e \sim 5000 - 8000^\circ \text{ K}$. We may

consider the equivalent width (W) ratio between the doublet lines at 1264 and at 1814 Å both due to a $^2D_{\frac{5}{2}} \rightarrow ^2P_{\frac{3}{2}}$ transition; in the simplest case we have:
 $W_{1263}/W_{1814} \approx (N_{u,1264}/N_{u,1814}) (f_{1264}/f_{1816}) (\lambda_{1264}/\lambda_{1816})^2 \approx 0.485 \frac{f_{1264}}{f_{1816}} e^{-\frac{\Delta E}{kT}} \approx 0.27$
 if $T = 5000^\circ$, where f is the oscillator strength, N_u are the density of the upper electronic levels giving rise to the two lines, and the energy difference between the transitions is $\Delta E \approx 3$ eV.

6.4. Use of SiIV λ 1397, CIV λ 1549 and SiII λ 1814

The same caveats mentioned for the ratio CIII] λ 1909/ SiIII] λ 1892 apply to the AlIII λ 1860/ SiIII] λ 1892 ratio as well. The ground term 1S_0 has energy 16 eV and 24 eV for Si $^{+2}$ and C $^{+2}$ respectively. A dependence on the ionization parameter is expected, as already mentioned. However, given the similarity in the ionization structure of the photo-ionized slab, it is after all not surprising that the ratio AlIII λ 1860/ SiIII] λ 1892 is almost insensitive to the ionization parameter over a wide range of density. We remind that the detection of strong AlIII λ 1860 *alone* already suggests that we are considering very high density emitting gas even if metallicity is super-solar. Simulations indicate that AlIII λ 1860 should increase smoothly with density and be weakest in canonical BLR if the density is $n_H \sim 10^9 \text{ cm}^{-3}$ (cf. Korista et al. 1997).

The ratio AlIII λ 1860/ SiIII] λ 1892 is therefore diagnosing high density gas, while the CIII] λ 1909/ SiIII] λ 1892 ratio covers the domain of $n_H \sim 10^{10} \text{ cm}^{-3}$. The ratio AlIII λ 1860/ SiIII] λ 1892 alone is, generally speaking, insufficient to determine n_H . A second diagnostic ratio is needed to constrain U and to unambiguously derive n_H .

We consider $\text{SiII}\lambda 1814 / \text{SiIII}\lambda 1892$, $\text{CIV}\lambda 1549 / \text{SiIII}\lambda 1892$, $\text{SiIV}\lambda 1397 / \text{SiIII}\lambda 1892$ as three diagnostic ratios suitable for constraining U .

The $\text{SiII}\lambda 1814$ doublet is conveniently placed, although weak or undetectable in most sources. The $\text{SiII}\lambda 1814 / \text{SiIII}\lambda 1892$ ratio is anti-correlated with U in a regular form, as our CLOUDY simulations show, especially for $\log U \lesssim -2$, and for density not much above the critical density of $\text{SiIII}\lambda 1892$. The behavior of the ratio $\text{SiII}\lambda 1814 / \text{SiIII}\lambda 1892$ resembles the distribution of $\text{CIII}\lambda 1909 / \text{CIV}\lambda 1549$ in the plane (n_{H}, U) which shows a very regular dependence and a smooth anti-correlation with U until the collisional quenching of $\text{CIII}\lambda 1909$ sets on. However, the IP of Si^0 is just 8 eV. **The majority of the $\lambda 1814$ doublet is emitted in the partially ionized zone (PIZ) near the hydrogen ionization front.** Fig 10 (bottom panel) shows the behavior of the volume emissivity ϵ times the geometrical depth within an emitting slab of gas as a function of the depth itself. Since the actual line emission is proportional to $\epsilon \cdot h$ reported in Fig. 10, the emission of the $\text{AlIII}\lambda 1860$, and $\text{SiIII}\lambda 1892$ lines is negligible in the PIZ, but the one of $\text{H}\beta$ certainly is not, and may be well dominating if $N_{\text{c}} \gg 10^{23} \text{cm}^{-2}$. Significant emission in the PIZ is expected also for the $\text{SiII}\lambda 1814$ doublet. However, for this latter line, total emission should not depend strongly on column density, since the emissivity becomes very low at $N_{\text{c}} \gtrsim 10^{23} \text{cm}^{-2}$. If higher N_{c} are considered (up to 10^{25}cm^{-2}), ratios including $\text{SiIII}\lambda 1892$, $\text{AlIII}\lambda 1860$, and $\text{SiII}\lambda 1814$ show a very weak dependence on column density, with changes a few percent at worst.

We attempted to isolate a $\text{CIV}\lambda 1549$ and a $\text{SiIV}\lambda 1397$ component that corresponds to the $\text{AlIII}\lambda 1860$ and $\text{SiIII}\lambda 1892$ lines. This can be a small part of

the total $\text{CIV}\lambda 1549$ and of $\text{SiIV}\lambda 1397$ emission, but there is no point to consider the whole $\text{CIV}\lambda 1549$ emission when $\text{CIV}\lambda 1549$ shows a large blueshift and is much broader than $\text{H}\beta$ (Fig. 5 of Sulentic et al. 2000) and $\text{SiIII}\lambda 1892$ and $\text{AlIII}\lambda 1860$ (Fig. 2 of Marziani et al. 2010). Taking into account various sources of ambiguity (mainly uncertainty in the quasar rest frame, S/N, blending with $\text{HeII}\lambda 1640$), the $\text{CIV}\lambda 1549$ BC component **we measure with our fits** is constrained within $\pm 50\%$ at worst. Thus we find significant $\text{CIV}\lambda 1549$ emission from the low-ionization gas, and the basic assumption is that its $\text{CIV}\lambda 1549$ profile is the same as the $\text{AlIII}\lambda 1860$, $\text{SiIII}\lambda 1892$ lines. If one considers the emissivity behavior, $\text{CIV}\lambda 1549$ and $\text{SiIV}\lambda 1397$ are obviously favored within the fully ionized zone.

The ratio of $\text{CIV}\lambda 1549$ and $\text{SiIV}\lambda 1397$ over $\text{CIII}\lambda 1909$ or over $\text{SiIII}\lambda 1892$ increases with ionization parameter in a way that is roughly independent on density until the collisional quenching of the semi-forbidden lines sets on (Fig. 9). The previous considerations are helpful to understand why the $\text{CIV}\lambda 1549$ and $\text{SiIV}\lambda 1397$ ratios provide clear diagnostics of the ionization parameter and seem to be in (at least qualitative) agreement with ratios employing lower ionization lines like $\text{SiII}\lambda 1814/\text{SiIII}\lambda 1892$ that is also mainly sensitive to U . The striking fact that the $\text{CIV}\lambda 1549$ and $\text{SiIV}\lambda 1397$ emission confirms low-ionization supports the hypothesis that the four lines are emitted by the same region. The ratios involving Si only have the obvious advantage that the the determination of the physical parameters is not dependent on metallicity; the drawback of $\text{SiIV}\lambda 1397$ is that this line is weaker and blended with $\text{OIV}\lambda 1402$. However, as already pointed out, the $\text{SiIV}\lambda 1397$

BC intensity should be slightly affected by $\text{OIV}] \lambda 1402$.

7. Results on two Extreme, Elucidating Cases

We analyze two extreme objects – one extreme Pop. A and one extreme Pop. B – with the same methodology we used previously. The aim of this analysis is to help the interpretation of the line components measured on the spectra of the 8 $z \approx 3$ quasars.

7.1. SDSS Weak $\text{CIII}] \lambda 1909$ source: SDSS J120144.36+011611.6

Our project stems from the careful analysis of the I Zw 1 UV spectrum by Laor et al. (1997b), and the evidence of a well-defined trend in the $\lambda 1900\text{\AA}$ blend along the E1 sequence (Aoki & Yoshida 1999, Wills et al. 1999, Bachev et al. 2004, Marziani et al., 2010). The NLSy1 I Zw 1 is known to be a sort of extremum in the E1 sequence: it shows strong FeII and FeIII , prominent $\text{AlIII} \lambda 1860$ and $\text{SiIII} \lambda 1892$ emission. It is an example of the A3 spectral type, whose median 1900\AA blend is shown in Fig. 3 of Bachev et al. (2004). Definitely, these sources are present also at intermediate to high redshift. We describe here the analysis of one source, SDSS J120144.36+011611.6 (Fig. 8), which seems to be a high-redshift, high-luminosity replica of I Zw 1, with broader lines (the FWHM limit of NLSy1s and Pop. A sources is luminosity dependent; see Netzer & Trahtenbrot 2007 and Marziani et al. 2009). These sources are Pop. A, and we assume that the profile of the BC is Lorentzian. Hereafter unshifted Lorentzian part of the line is said to be BC. Pop.

A sources are also free of any VBC, making the analysis of the blend simpler.

Several considerations can be made from Fig. 8.

AlIII λ 1860 The lines less ambiguous to measure are the AlIII λ 1860 doublet because the two lines are less blended with other features, and they are remarkably strong. SiIII] λ 1892 is more heavily blended with CIII] λ 1909 and FeIII. However, the SPECFIT routine allows usually a plausible deconvolution of SiIII] λ 1892, making the AlIII λ 1860/ SiIII] λ 1892 ratio very reliable. FeII and FeIII are obviously strong. We can use FeII UV 191 to set roughly the level of FeII, while the feature at 2080Å is helpful to estimate intensity of FeIII.

FeIII Our SPECFIT analysis produces a very weak CIII] λ 1909 component. A precise measurement of CIII] λ 1909 is cumbersome, since its intensity depends on the actual FeIII emission. The strong feature at λ 1914 could be dominating, and the template may seriously underestimate it (see Vestergaard and Wilkes 2001 for several alternatives in the empirical FeIII emission of I Zw 1). In any case the residual CIII] λ 1909 emission is small, suggesting that the λ 1900 blend, once believed to be mostly CIII] λ 1909, is actually almost void of CIII] λ 1909 emission in these A3-type sources.

SiII λ 1814 The SiII λ 1814 line is well visible in the spectrum of SDSS J120144.36+011611.6 and can be used as a substitute of CIV λ 1549 to measure the ionization parameter. The ratio SiII λ 1814/ SiIII] λ 1892 is mainly sensitive to the ionization parameters, as it is the ratio CIV λ 1549/ SiIII] λ 1892. The ratio

$\text{SiII}\lambda 1814 / \text{SiII}\lambda 1892$ has the considerable advantage of being weakly dependent on metallicity. If metallicity is known (see also §8.1), the ratio $\text{CIV}\lambda 1549 / \text{AlIII}\lambda 1860$ should be in principle preferred since $\text{AlIII}\lambda 1860$ is emitted through a permitted resonance transition while $\text{SiII}\lambda 1814$ is emitted in the collisionally excited, partially-ionized zone (PIZ).

CIV $\lambda 1549$ We fit $\text{CIV}\lambda 1549$ with a Lorentzian component that is unshifted + a $\text{CIV}\lambda 1549$ BBC. Note that the lack of shift in $\text{AlIII}\lambda 1860$ and $\text{SiII}\lambda 1892$ imposes a strong, determinant condition on the strength of the Lorentzian-component in $\text{CIV}\lambda 1549$. It is important to stress that some $\text{CIV}\lambda 1549$ BC emission is expected to be present according to our array of simulations. The ratio $\text{CIV}\lambda 1549 / \text{AlIII}\lambda 1860$ is rather modest, as we can easily see even by eye. We note in passing that the width of BBC is $\approx 10000 \text{ km s}^{-1}$, with a peak blueshift indicatively of -6000 km s^{-1} , significantly larger than the one measured on the $\text{CIV}\lambda 1549$ of I Zw 1 by Marziani et al. (2009).

SiIV $\lambda 1397$ We fit $\text{SiIV}\lambda 1397$ with a Lorentzian component that is unshifted + a BBC (that may include $\text{SiIV}\lambda 1397$ and $\text{OIV}\lambda 1402$ contribution). Results that are consistent with the ones of $\text{CIV}\lambda 1549$. The ratio $\text{SiIV}\lambda 1397 / \text{SiII}\lambda 1892$ has the advantage that is almost independent on metallicity. In principle, the crossing point between the $\text{SiII}\lambda 1814 / \text{SiII}\lambda 1892$ and $\text{SiII}\lambda 1814 / \text{SiII}\lambda 1892$ can set a metallicity independent point in the (n_{H}, U) plane. If the accuracy of the $\text{SiII}\lambda 1814$ intensity is good then this point can be used to retrieve information on

metallicity (§8.1).

We consider the measured line ratios in the plane U vs. n_{H} (initially assuming metallicity equal to solar), and see where they cross. We find very high density and low ionization (Fig. 11).

7.1.1. Along the E1 Sequence: A More Complex Scenario

Looking at the fit solution (Fig. 8(b)), it seems that our spectrum has almost no $\text{CIII}] \lambda 1909$. In many ways this is not surprising. The physical solutions in the (U, n_{H}) plane of Fig. 11, points toward very low ionization ($U \sim 10^{-3} - 10^{-2}$) and high density ($n_{\text{H}} \gtrsim 10^{12} \text{cm}^{-3}$). At such high values of n_{H} we expect that $\text{CIII}] \lambda 1909$ is collisionally quenched, and no significant emission. The ratio $\text{CIII}] \lambda 1909 / \text{CIV} \lambda 1549$ is expected to be just $\sim 10^{-2}$ in the dense LIL-BLR. Therefore we can say that sources like SDSS and I Zw 1 are extreme because all of the $\lambda 1900 \text{\AA}$ blend is emitted by very low ionization, dense gas.

However, as soon as we move away from spectral types A3+ along the E1 sequence, we see that the prominence of $\text{AlIII} \lambda 1860$ diminishes greatly. The emission disappears altogether at the other end of the E1 sequence, where several lobe-dominated radio-loud sources are found. For most quasars we see that $\text{CIII}] \lambda 1909$ is rather strong and unmistakably present. At a first glance this complicates the interpretation of the spectrum. However, one has to consider that $\text{CIII}] \lambda 1909$ can be emitted only by gas of much lower n_{H} than that of the region where the bulk of $\text{SiIII}] \lambda 1892$ and $\text{AlIII} \lambda 1860$ is emitted. Our simulations show

that $\text{AlIII}\lambda 1860$ intensity grows smoothly as a function of density in the ionization parameter range of interest $-3 \lesssim \log U \lesssim -1$. This said, and considered the smooth trend we see from A3 to B1⁺, the most reasonable conclusion is that a dense region emits significantly whenever $\text{AlIII}\lambda 1860$ emission is detected, although the relative prominence of the dense BC changes along the E1 sequence: it accounts for the entire LIL emission *only* in the most extreme Pop. A sources. The sequence of Fig. 3 of Bachev et al. (2004) seems to be mainly a sequence of prominence of $\text{AlIII}\lambda 1860 + \text{SiIII}]\lambda 1892$ vs $\text{CIII}]\lambda 1909$.

So, a very important conclusion is that a very dense, low-ionization region exists in the wide majority of quasars. It is associated with FeII prominence, as such gas is expected to emit a strong low-ionization spectrum. The most extreme FeII emitters are also the most extreme $\text{AlIII}\lambda 1860$ emitters; in some cases where no $\text{AlIII}\lambda 1860$ emission is measured, we also fail to detect any FeII emission (Marziani et al. 2010). Where is this region located? Why there are such distinctive line profiles as Lorentzian? The second issue goes beyond the present paper; for the moment our aim is to measure line components of $\text{AlIII}\lambda 1860$, $\text{SiII}\lambda 1814$, $\text{SiIII}]\lambda 1892$ and $\text{CIV}\lambda 1549$ that come from this region and to estimate its distance from the central black hole (§9).

7.2. The Other E1 Extremum: 3C 390.3

3C 390.3 is a lobe-dominated (LD) RL source, with very broad emission lines and no optical FeII within detection limits (see Marziani et al. 2003, for the criterion used). It also shows a large peak shift in its $\text{H}\beta$ profile, and prominent narrow lines

($[\text{OIII}]\lambda 5007$, $\text{H}\beta$), but also narrow components of $\text{CIV}\lambda 1549$ and $\text{CIII}]\lambda 1909$ which are all well separated from the broad $\text{H}\beta$ profile.

To deconvolve the blends around $\text{CIII}]\lambda 1909$ and $\text{CIV}\lambda 1549$, we assume the same emission line profiles as for $\text{H}\beta$. The $\text{H}\beta$ broad profile can be described as the sum of a BC and a VBC. An unusual property of the BC is its large peak blueshift (it is unusual because of the shift amplitude: even if median spectra of Pop. B sources show a small BC redshift, there is a pretty large scatter with both red- and blueshifted peaks observed in individual sources; Zamfir et al. 2010). Applying in a self consistent way the BC and VBC to the $\text{CIII}]\lambda 1909$ and $\text{CIV}\lambda 1549$ blends, leads to very interesting results as shown in Figure 8:

- $\text{AlIII}\lambda 1860$ is very weak or even absent within the S/N limits;
- the $\text{CIV}\lambda 1549$ profile is very similar to the one of $\text{H}\beta$: BC+VBC accounts for more than 90% emission, with a possible, very weak contribution of the blueshifted component which is usually dominating in Pop. A sources;
- the red wing observed in the 1900\AA blend is accounted for only if there is a strong $\text{CIII}]\lambda 1909$ VBC, FeII and FeIII emission being below the detectability limit in this source;
- there is no evidence of a VBC in $\text{AlIII}\lambda 1860$;
- the ratio $\text{CIV}\lambda 1549/\text{CIII}]\lambda 1909$ BC is ≈ 10 , a far cry from the ratios observed in extreme Pop. A sources like I Zw 1 and SDSS J120144.36+011611.6;

- even more interesting we find a $\text{CIV}\lambda 1549/\text{CIII}\lambda 1909$ VBC ≈ 10 , as for the BC.

We conclude that this object is fundamentally different from Pop. A sources. The low ionization, high density BC seems to be absent. The similarity in the $\text{CIV}\lambda 1549/\text{CIII}\lambda 1909$ ratios suggest that we are observing a gas in conditions similar to the one associated to the VBC. We predict that FeII will remain undetected or found to be weak even with $S/N \rightarrow \infty$.

In the plane (U, n_H) of Figure 11, the line ratios converge to a point at $\log U \approx -1.5$, and $\log n_H \approx 10.1$ (the $\text{SiII}\lambda 1814$ line cannot be measured accurately since S/N is poor). In this case, the $\text{CIII}\lambda 1909/\text{CIV}\lambda 1549$ ratio also converges toward a (U, n_H) value consistent with the one indicated by the $\text{AlIII}\lambda 1860/\text{SiII}\lambda 1814$. In most other cases, this does not happen because the $\text{AlIII}\lambda 1860$ doublet is too strong to be accounted for by gas of $n_H \sim 10^{10} \text{cm}^{-3}$ even at super-solar metallicity. Emission occurs at pretty high ionization, in conditions that once upon a time were thought to be standard in quasars (Davidson and Netzer 1979). This Pop. A and B difference at the extrema was already pointed out, in a semi-quantitative way, by Sulentic et al. (2000) and Marziani et al. (2001).

It is however important not to generalize the case of 3C 390.3 to the remaining Pop. B sources. In most of them, $\text{AlIII}\lambda 1860$ is detected, and there is evidence of strong $\text{CIII}\lambda 1909$. Actually $\text{CIII}\lambda 1909$ emission seems to be appreciable in all of our VLT quasars. This means that we are in a composite situation, where low-ionization, high-density emission is present, along with significant VBC and other emission. The two extreme cases help us however to understand these more

complex cases.

7.3. The Contribution of Lower Density Gas

Once the true intensity of the BC components is retrieved, the presence of significant $\text{CIII}] \lambda 1909$ emission complicates the analysis. As pointed out, the photoionization solution for the BC suggests very high density, and in this region no $\text{CIII}] \lambda 1909$ emission is expected. Whenever $\text{CIII}] \lambda 1909$ is observed, we need to reverse the question: how much does any $\text{CIII}] \lambda 1909$ emitting gas contribute to the lines used for diagnostic ratios? Negligible contribution is expected to $\text{AlIII} \lambda 1860$. However, this is not true for $\text{CIV} \lambda 1549$ and $\text{SiIII}] \lambda 1892$. Especially among Pop. A2 and A3 objects, it is not so obvious that the profile of $\text{CIII}] \lambda 1909$ and $\text{SiIII}] \lambda 1892$ is the same. It could be well that the $\text{CIII}] \lambda 1909$ profile is narrower than the ones of $\text{SiIII}] \lambda 1892$ and $\text{AlIII} \lambda 1860$ (as found for SDSS J1201+0116), justifying the idea of $\text{CIII}] \lambda 1909$ emission from a disjoint region (§6.2). For the BAL QSOs in our sample and $\text{AlIII} \lambda 1860$ -strong sources most of what we ascribe to $\text{CIII}] \lambda 1909$ could be actually FeIII , as suggested by Hartig and Baldwin (1986).

However, objects like the typical A1 sources show $\text{SiIII}] \lambda 1892$ and $\text{CIII}] \lambda 1909$ with similar profiles, so in the following we will assume the worst condition, that is all $\text{CIII}] \lambda 1909$ emitting gas is contributing to the BC lines.

To estimate the contribution of the $\text{C III}] \lambda 1909$ emitting gas to $\text{Si III}] \lambda 1892$ and $\text{C IV} \lambda 1549$, we can consider the trends observed along E1. $\text{Si III}] \lambda 1892$ is strong when $\text{Al III} \lambda 1860$ is strong, and the $\text{Si III}] \lambda 1892 / \text{C III}] \lambda 1909$ ratio is lower when $\text{C III}] \lambda 1909$ is strong, as visible in both Baldwin et al. (1996) and Bachev et al. (2004), as well as in the present paper. The observed $\text{Si III}] \lambda 1892 / \text{C III}] \lambda 1909$ ratio in the A1 median bin seems to be as low as in Mark 335, ≈ 0.4 . Pop. B sources that often show prominent $\text{C III}] \lambda 1909$ also show a low $\text{Si III}] \lambda 1892 / \text{C III}] \lambda 1909$ ratio, as also appreciable in the median spectra of Bachev et al. (2004). These trends suggest that most $\text{Si III}] \lambda 1892$ is emitted where $\text{Al III} \lambda 1860$ is also emitted. As a consequence, any correction due to gas in different physical conditions (lower density) emitting $\text{Si III}] \lambda 1892$ is expected not to be dominant unless $\text{C III}] \lambda 1909$ is extremely strong. The $\text{C III}] \lambda 1909$ emitting gas should be at density $\log n \sim 9$, or lower. Higher density would imply increasing $\text{Si III}] \lambda 1892 / \text{C III}] \lambda 1909$ to values that would exceed the observed ones even if the LIL-BC is not emitting any significant $\text{Si III}] \lambda 1892$ (see Fig. 13).

7.3.1. Preliminary analysis of a low- z sample

To set these trends on a more quantitative basis we considered the set of pre-COSTAR recalibrated sources, for which $\text{C III}] \lambda 1909$ and $\text{C IV} \lambda 1549$ data are publicly available (Kuraszkiewicz et al 2002, Evans & Koratkar 2004). We performed measurements (interactively with the

task SPLOT of IRAF) for about 30 sources with the highest S/N, holding a CIII] λ 1909 blend that could be relatively easily deblended, and following the expectations described in §4.4. The rest frame equivalent width of AlIII] λ 1860 and SiIII] λ 1892 are found to be highly correlated (Fig. 12). The correlation is due to SiIII] λ 1892 being stronger when AlIII] λ 1860 is strong, not necessarily because CIII] λ 1909 is strong: actually, the SiIII] λ 1892/CIII] λ 1909 ratio can be low when CIII] λ 1909 is strong, and the AlIII] λ 1860/ SiIII] λ 1892 ratio achieves maximum values when CIII] λ 1909 is faintest. This is consistent with the bulk of AlIII] λ 1860 and SiIII] λ 1892 originating in the same region. At the same time the presence of CIII] λ 1909 lowers the AlIII] λ 1860/ SiIII] λ 1892, CIV] λ 1549/ SiIII] λ 1892 and SiIV] λ 1397/ SiIII] λ 1892 because of “excess” SiIII] λ 1892 emission associated to the gas emitting CIII] λ 1909.

7.3.2. *The effect of low-density gas on the product (Un_H)*

We expect that any correction will increase density (increase AlIII] λ 1860/ SiIII] λ 1892 lowering SiIII] λ 1892) and decrease ionization parameter (lowering CIV] λ 1549 more than SiIII] λ 1892), but that their product will be less affected. To show the amplitude of the effect we performed an experiment, adding to a pure, high-density solution, contribution from moderate density gas ($\log n_H \sim 9 - 10$). The Fig. 14 shows the displacement in the density – ionization parameter plane for several values of the CIII] λ 1909/ SiIII] λ 1892 intensity ratio. The

values refer to the $\text{C III}] \lambda 1909$ addition over $\text{Si III}] \lambda 1892$ in the ideal case, corresponding to observed ratios of 0.34, 0.7, 1.0, 1.1 for an addition of a $\text{C III}] \lambda 1909$ component whose intensity is 0.4, 1.0, 1.5, 2.0 the intensity of the $\text{Si III}] \lambda 1892$ component associate to the high density gas. As one can see from the figure, even if deviation for U and n_{H} taken separately are significant, deviations for the product are by far less important. The largest change for the product is found to be ≈ 0.15 , if we exclude the gray dots corresponding to $\log n_{\text{H}} = 10$ (an unlikely case, since this would imply a correction $\text{Si III}] \lambda 1892 / \text{C III}] \lambda 1909 > 1$, inconsistent with what we observe when $\text{C III}] \lambda 1909$ is strong). Following the expected line ratios of Fig.13 we apply a correction to the BC fluxes that is 0.4 and 1.5 $\text{C III}] \lambda 1909$ for $\text{Si III}] \lambda 1892$ and $\text{C IV} \lambda 1549$ respectively (Figures 15, 16 and 11), corresponding to $\log U = -2$ and $\log n_{\text{H}} = 9$. We remark that that if U is lower, the correction will have negligible effect, while assuming a larger U will lead to $\text{C IV} \lambda 1549$ flux in excess to the one observed.

To constrain the ionization parameter we can first consider that, since the $\text{C III}] \lambda 1909$ gas comes from a (relatively) low density region, the contribution to $\text{Si III} \lambda 1814$ is small: for $\log n \sim 9$ and $\log U \approx -2$, the contribution should be $\approx 0.03 \text{ C III}] \lambda 1909$. Second, another powerful feature is the $\text{Si IV} \lambda 1397$ doublet (Baldwin et al. 1996): the $\text{Si IV} \lambda 1397$ doublet is less affected by the $\text{C III}] \lambda 1909$ correction, the contribution from lower density gas being estimated $\approx 0.25 \text{ C III}] \lambda 1909$. The line ratio $\text{Si IV} \lambda 1397 / \text{Al III} \lambda 1860$ is also sensitive to ionization and less affected by any lower density correction (provided that the relative abundance of S

and Al stays the same, as it seems to be the case).

In summary, corrected BC line intensities are computed as follows: $I^c(\text{SiII}\lambda 1814)_{\text{BC}} = I(\text{SiII}\lambda 1814)_{\text{BC}} - 0.03 I(\text{CIII}\lambda 1909)_{\text{BC}}$; $I^c(\text{SiIII}\lambda 1892)_{\text{BC}} = I(\text{SiIII}\lambda 1892)_{\text{BC}} - 0.4 I(\text{CIII}\lambda 1909)_{\text{BC}}$; $I^c(\text{SiIV}\lambda 1397)_{\text{BC}} = I(\text{SiIV}\lambda 1397)_{\text{BC}} - 0.26 I(\text{CIII}\lambda 1909)_{\text{BC}}$; $I^c(\text{CIV}\lambda 1549)_{\text{BC}} = I(\text{CIV}\lambda 1549)_{\text{BC}} - 1.5 I(\text{CIII}\lambda 1909)_{\text{BC}}$.

8. Results on the $z \approx 3$ Quasars

To estimate $\log n_{\text{H}}$ and $\log U$ values, we use the CLOUDY contour plots of the ratios $\text{AlIII}\lambda 1860 / \text{SiIII}\lambda 1892$, $\text{SiII}\lambda 1814 / \text{SiIII}\lambda 1892$, $\text{CIV}\lambda 1549 / \text{SiIII}\lambda 1892$, $\text{SiIV}\lambda 1397 / \text{SiIII}\lambda 1892$ showed in Fig. 9². The data points of our objects are in regions where the ratios are well-defined. The ratios $\text{CIV}\lambda 1549 / \text{SiIII}\lambda 1892$, $\text{SiIV}\lambda 1397 / \text{SiIII}\lambda 1892$, and $\text{SiII}\lambda 1814 / \text{SiIII}\lambda 1892$ are mainly sensitive to the ionization parameter U , while $\text{AlIII}\lambda 1860 / \text{SiIII}\lambda 1892$ and $\text{CIII}\lambda 1909 / \text{SiIII}\lambda 1892$ are mainly sensitive to the electron density. We know that $\text{CIII}\lambda 1909$ is collisionally quenched at $\log n_{\text{e}} \gtrsim 10$ and in the contour plot for $\text{CIII}\lambda 1909 / \text{SiIII}\lambda 1892$ we see a step around this value.

We measure the BC intensity of $\text{SiIII}\lambda 1892$, $\text{AlIII}\lambda 1860$, $\text{SiII}\lambda 1814$, $\text{SiIV}\lambda 1397$ and $\text{CIV}\lambda 1549$; with them we compute the diagnostic ratios (for 3C390.3 we use

²Note that there are regions where the ratio values are actually undefined: close to the high U limit ($\log U \gtrsim -0.3$), ratios $\text{AlIII}\lambda 1860 / \text{SiIII}\lambda 1892$ and $\text{SiII}\lambda 1814 / \text{SiIII}\lambda 1892$ (with $n_{\text{H}} \lesssim 10^9 \text{cm}^{-3}$) should not be considered.

CIII] λ 1909 in place of SiII λ 1814; however there is no object similar to 3C390.3 among the $z \approx 3$ quasars). We present the fluxes of the line components in Tab. 3 and the equivalent width in Tab. 5. Table 4 shows the weak lines around CIV λ 1549. For CIV λ 1549 line we show the core, blue shifted and the very broad components. Errors are at a 2σ confidence level, and include the sources of uncertainty described in §4.5. Errors are then quadratically propagated according to standard practice to compute intensity ratios and their logarithm.

From Table 3 we can derive the diagnostic ratios. As we see in Fig. 1, SiII λ 1814 is absorbed by telluric B band in J00103-0037, J03036-0023, J20497-0554 (most affected). We will not consider SiII λ 1814 to compute n_H and U on those cases. However, if we take at face value the SiII λ 1814 measure on J00103-0037 and J20497-0554, it will converge close to the point set by the remaining two ratios. We display on a graph a line representing the behavior of each ratio under the assumption of solar metallicity; the ideal point where the lines representing different diagnostic ratios cross determines the values of $\log n_H$ and $\log U$. Figs. 15 and 16 shows the contour plots where we can see that the diagnostic ratios converge to rather well defined values. The cross point is very precise for the objects J00103-0037, J00521-1108, J02287+0002 (using z_{CIII}), and J20497-0554 ; for the remaining objects J01225+1339, J02287+0002 (using z_{OI}), J02390-0038, J03036-0023, and J23509-0052 the cross point is slightly different. We must not forget the errors involving the fits, such as the changing of the shape profile that makes large the peak intensity if is Lorentzian or it could be less intense if it is Gaussian; the FeII pseudo-continuum contribution that affects principally to SiII λ 1814 or the FeIII that in some cases affects CIII] λ 1909.

In principle, the crossing point of the ratios $\text{SiIV}\lambda 1397 / \text{SiIII}\lambda 1892$ and $\text{SiII}\lambda 1814 / \text{SiIII}\lambda 1892$ is independent on metallicity. Therefore, any significant disagreement between this crossing point and the ratios based on $\text{CIV}\lambda 1549$ may indicate chemical composition different from the assumed solar one (§8.1). The difficulty here is the large uncertainty of the $\text{SiII}\lambda 1814$ line. In all contour plots we show the $\pm 2\sigma$ interval as a shaded band. So, it is proper to consider deviations from metallicity only in the case of 4 sources where the crossing point excluding $\text{SiII}\lambda 1814$ is outside the uncertainty band.

For the objects J00103-0037, J03036-0023 and J20497-0554 we exclude the $\text{SiII}\lambda 1814$ line from the diagnostic ratios because it is affected by absorption. For the remaining objects, we take the average of the crossing contour plots of $\log(\text{AlIII}\lambda 1860 / \text{SiIII}\lambda 1892)$ crossing with $\log(\text{CIV}\lambda 1549 / \text{SiIII}\lambda 1892)$ and $\log(\text{AlIII}\lambda 1860 / \text{SiIII}\lambda 1892)$ crossing with $\log(\text{SiII}\lambda 1814 / \text{SiIII}\lambda 1892)$. For 3C390.3 we use $\log(\text{CIII}\lambda 1909 / \text{SiIII}\lambda 1892)$ instead of $\log(\text{SiII}\lambda 1814 / \text{SiIII}\lambda 1892)$. Table 6 summarizes the $\log n_{\text{H}}$ and $\log U$ values including their uncertainty. Since U and n_{H} are not independent quantities (their correlation coefficient is found to be 0.55), we adopt the appropriate formula for the errors on the product Un_{H} (following Bevington 1969). We present average values of the crossing points for extreme objects of Fig. 11 and 18(d). In the SDSS J12014+0116 case we give full weight to the $\text{SiII}\lambda 1814$ measurement. The crossing points disagree somewhat for SDSS J12014+0116. This could be due to an underestimate of *both* $\text{SiII}\lambda 1814$ and $\text{CIV}\lambda 1549$ in the fits. On the one hand, $\text{SiII}\lambda 1814$ is clearly seen and strong but is contaminated by FeII blend; on the other hand, $\text{CIV}\lambda 1549$ is strongly affected by

the blue-shifted component and by the assumption that it is of Gaussian shape. An increase by 30% in the measurement of the intensity of the two line would lead to a better agreement but this is somewhat an ad-hoc speculation. Rather, the significant difference between the crossing point of the $\text{SiII}\lambda 1814 / \text{SiIII}\lambda 1892$ and $\text{SiIV}\lambda 1397 / \text{SiIII}\lambda 1892$ ratios and the other ones point toward strong metal enrichment. We will show in §8.1 that this is probably the case.

At any rate, the convergence is toward a value of $\log U \approx -3$, lower than for the other $z \approx 3$ quasars. This is reflected in the $\text{CIV}\lambda 1549$ EW of this source, also significantly lower. **It is intriguing to note that the correction because of lower density drives the other sources toward values of U and n_{H} that are closer to the ones of SDSS J12014+0116.**

Table 7 reports the values of the r_{BLR} and the M_{BH} of our 8 objects and the extreme objects in the last two rows. Column 1 identifies the quasar name; Col. 2 gives the quasar proper distance in **mega parsecs [Mpc]**; Cols. 3 and 4 are the continuum specific flux value at 1350\AA and 1700\AA respectively, Col. 5 reports the FWHM in km s^{-1} for the broad components, Col. 6 is the Population designation. **Cols. (7) to (10) report the logarithm of the size of the BLR in cm obtained from: a) $1Z_{\odot}$, b) $1Z_{\odot}$ line ratios corrected because of low density emission, c) $5Z_{\odot}$, and d) $5Z_{\odot}$ line ratios corrected because of low density emission.** Cols. (11) -(14) list the logarithm of the black hole mass in solar masses in the same order as for r_{BLR} . Finally Col. (15) is M_{BH} computed from Vestergaard and Peterson (2006) formula (Equation 10). We will explain in §10 how these quantities are computed.

8.1. Effects of Metallicity

The strength of $\text{Nv}\lambda 1240$ relative to $\text{Civ}\lambda 1549$ and $\text{HeII}\lambda 1640$ suggests supersolar chemical abundances (Hamann and Ferland 1993; Hamann & Ferland 1999). Chemical abundances may be well 5 to 10 times solar (Dhanda et al. 2007), with $Z \approx 5Z_{\odot}$ reputed typical of high z quasars (Ferland et al. 1996). The E1 sequence seems to be mainly a sequence of ionization in the sense of a steady decrease in prominence of the low-ionization BC toward Population B (Marziani et al. 2001, 2010). However, this is not to neglect that metal-enrichment also plays a role, especially for the most extreme Pop. A sources i.e., those in bin A3 and higher (Sulentic et al. 2001).

The lines employed in the present study come from carbon, silicon and aluminium; all these element can be significantly depleted from gas if dust grains are formed (e. g., Mathis 1990). However, the emitting regions where our lines are produced are thought too hot to contain significant amount of dust (a definition of broad line region is right the central engine region below the dust sublimation region: e.g., Elitzur 2009). In addition Si and Al are expected to be produced under similar circumstances in the late stage of evolution of massive stars (Clayton 1983, Ch. 7). We note also that the $\text{Civ}\lambda 1549 / \text{SiIII}\lambda 1892$ and $\text{Civ}\lambda 1549 / \text{AlIII}\lambda 1860$ usually give results that are in perfect agreement in the plane (n_{H}, U) . These findings support our assumption that, if metallicity variations are present, the relative abundance Al to Si remains constant. **We considered two cases for enhanced metallicity: (1) constant solar abundance ratio Al:Si:C with $Z = 5Z_{\odot}$ (5Z) ; (2) an overabundance of Si with respect to carbon by**

a factor 3, again with $Z = 5Z_{\odot}$ (5ZSA). This condition comes from the yields listed by Woosley and Weaver (1995) from type II Supernovæ. The Si overabundance is also supported by the chemical composition of the gas returned to the interstellar medium by an evolved population with a top-loaded initial mass function simulated using STARBURST 99 (Leitherer et al. 1999). The abundance of Al should scale roughly with the one of Si. While some cases with Al scaling with C are possible from the Woosely and Weaver (1995) yields, they are rarer than cases in which Al scales with Si. This latter case is appropriate for the most massive progenitors. Also, the assumption of Al scaling with C with $[\text{Si}/\text{C}] = 0.477$ would yield to implausible high density and lack of convergence to a well-defined solution for $\log n_{\text{H}} \lesssim 14$. We therefore assume in the following that Al scales with Si in the two cases listed above.

An array of simulations as a function of ionization parameter and density was computed assuming the conditions (1) and (2) listed in the previous paragraph. As expected, if the solar metallicity is simply scaled by a factor (5Z) we find that the ratio $\text{AlIII}\lambda 1860 / \text{SiIII}\lambda 1892$ is not strongly dependent on Z : the ratio increases by about 40% passing from $Z = 1Z_{\odot}$ to $Z = 5Z_{\odot}$, for $\log n_{\text{H}} \approx 12$ and $\log U \approx -2$. The same is true for the $\text{SiII}\lambda 1814 / \text{SiIII}\lambda 1892$ and $\text{SiIV}\lambda 1397 / \text{SiIII}\lambda 1892$ ratios. Since the first ratio sets n_{H} , and the last two U , the ratios mentioned in this paragraph should be preferred because they provide n_{H} and U values that are weakly affected by a factor 5 change in metallicity. A posteriori we confirm that the effect on the product Un_{H} derived also with ratios involving $\text{CIV}\lambda 1549$ is negligible in case 5Z (and it should be even more so if a metallicity increase is $Z_{\odot} \lesssim Z \lesssim 5Z_{\odot}$).

The two extreme cases seem to be revealing also as far as metallicity is concerned. Ratios converge to a fairly well defined point in the case of 3C 390.3 (see Fig. 11, left panel, $Z = 1Z_{\odot}$ assumed). In this case there is no major evidence of supersolar metallicity. The converse is true in the case of SDSS J120144.36+011611.6. The ratios involving C IV $\lambda 1549$ indicate a lower ionization level, with $\log U \sim -3$. **This is because C^{3+} changes ionization state to C^{2+} for smaller ionization parameters, and so C IV $\lambda 1549$ rapidly disappears.** The C IV $\lambda 1549$ intensity depends weakly on Z while the Al III $\lambda 1860$ and Si III] $\lambda 1892$ lines are more sensitive. The 5Z case yields values closer to the ones obtained from the Si and Al line ratios, but not yet in concordance. If we pass to case 5ZSA with a factor 3 Si overabundance, then the concordance of the line ratios is good, especially if no correction because of low density emission is applied. As a further confirmation we checked that the metallicity-dependent C IV $\lambda 1549$ /Si IV $\lambda 1397$ ratio is in very good agreement with the crossing point of the other lines. Therefore, in this case, we have independent measures of metallicity, n_H , and U . The case of even higher metallicity, say $Z \sim 10Z_{\odot}$, remains to be explored but may not be appropriate considering the good agreement with 5ZSA.

In principle, the discrepancy in the intersection point, with Si III] $\lambda 1892$ /C IV $\lambda 1549$ and Al III $\lambda 1860$ /C IV $\lambda 1549$ yielding lower U than the Al-Si ratios, should signal a significant enrichment in Si and Al of the BLR gas. In this case the Si IV $\lambda 1397$ /C IV $\lambda 1549$ ratio should be helpful, as it can be assumed to be dependent mainly on the Si abundance relative to C. Here, more than precisely determining the exact abundance value we are interested in analyzing the effect of large metallicity changes on U , n_H , and their product. Appreciable discrepancy is visible in the

contour plots of the BAL quasar J01225+1339, J03036-0023, J20497-0554 and J23509-0052 if $Z = Z_{\odot}$ is assumed.

In the same plots made for $Z = 5Z_{\odot}$ SA, the agreement becomes better (see Fig. 18). High metallicity yields higher U and smaller n_{H} if emission line ratios involving C IV $\lambda 1549$ are considered. This reflects the increase in abundance of Si and Al with respect to C, and the fact the Si II $\lambda 1814$, Si II $\lambda 1892$, Al III $\lambda 1860$ lines are emitted at lower ionization than C IV $\lambda 1549$. In the case of sources like J02390-0038 and J20497-0554, the discrepancy of the crossing lines might indicate $Z_{\odot} \lesssim Z \lesssim 5Z_{\odot}$, more than the extreme enrichment like the one assumed in 5ZSA, as also suggested by the C IV $\lambda 1549$ /Si IV $\lambda 1397$ ratio.

In Fig. 18 and 19 the contour plots are shown for the case 5ZSA. We consider uncorrected and corrected line ratios as two independent cases. The half-tone bands also show the importance of accurate Si II $\lambda 1814$ measurements to infer unambiguous constraints on metallicity (and, by extension, to estimate n_{H} and U independently). The product $n_{\text{H}}U$ is however much less affected than n_{H} and U individually (Tab. 6).

A first r_{BLR} and M_{BH} estimate can be obtained considering only the Si II $\lambda 1814$ /Si II $\lambda 1892$ and Al III $\lambda 1860$ /Si II $\lambda 1892$ ratios. We conclude that the effect of scaling the metallicity up to $Z = 5Z_{\odot}$ is within the uncertainty of the method, and particularly small if the ratios Si II $\lambda 1814$ /Si II $\lambda 1892$, Al III $\lambda 1860$ /Si II $\lambda 1892$, and Si IV $\lambda 1397$ /Si II $\lambda 1892$ are considered to compute n_{H} and U . It is significant if strong enrichment of Al and Si over C occurs. A more refined approach could exploit the dependence of Al III $\lambda 1860$ /C IV $\lambda 1549$ (and Si II $\lambda 1892$ /C IV $\lambda 1549$ and

SiIV λ 1397/CIV λ 1549) on Z to build a 3D diagram where n_{H} , U , Z along with Si-Al enrichment can be determined independently.

8.2. Determining the best estimate of n_{H} , U

There are two sets of line ratios for each object: one comes from the SPECFIT results, and the other is the one computed after correcting the SPECFIT results because of low density contributions. Solutions with corrected value usually point toward very high density and low ionization, predicting SiII λ 1814 emission even twice as strong as SiII λ 1892. However, increasing the metallicity for corrected ratios leads to better agreement among lines and more reasonable n_{H} , U values, while leaving the product fairly unaffected. Especially the assumption of Silicon - Aluminium enrichment improves the concordance in the intriguing cases of SDSS J12014+0116, J01225+1339, J02287+0002 (using z_{oi}), the extreme objects and the two BAL QSOs in our sample. However, apart from the case of SDSS J12014+0116, the enrichment is probably excessive. From the discussion above the independent determination of n_{H} and U seems possible only if metallicity is at least roughly known. We exclude metallicity cases where we find a sizeable disagreement in the crossing points (with the exceptions of ratios involving SiII λ 1814: the ionization level can be estimated in a Z -independent way using the SiIV λ 1397/SiII λ 1814 and the SiIV λ 1397). We consider each individual source with line intensity before and after

correction to obtain two independent sets of product $n_{\text{H}}U$ values. As mentioned, changing metallicity is not affecting the product $n_{\text{H}}U$ as much as n_{H} and U individually. In case of concordance of the crossing points and of high accuracy in the $\text{SiIII}\lambda 1814$ ratio, $n_{\text{H}}U$, and Z can be considered independently determined. In Table 6 we indicate the values that are deemed most appropriate.

9. A Photoionization Method to Compute the Broad Line Region Distance and the Black Hole Mass.

The distance of the broad line region (r_{BLR}) from the central continuum source and the black hole mass (M_{BH}) are key parameters that let us understand the dynamics of the gas in the emitting region and the quasar behavior and evolution. In this work we will use a method based on the determination of n_{H} and U to compute r_{BLR} . Eq. 1 can be rewritten as

$$r_{\text{BLR}} = \left[\frac{\int_{\nu_0}^{+\infty} \frac{L_{\nu}}{h\nu} d\nu}{4\pi U n_{\text{H}} c} \right]^{1/2} \quad (3)$$

and also as

$$r_{\text{BLR}} = \frac{1}{h^{1/2} c} (U n_{\text{H}})^{-1/2} \left(\int_0^{\lambda_{\text{Ly}}} f_{\lambda} \lambda d\lambda \right)^{1/2} d_p \quad (4)$$

where h is the Plank constant, c is the light speed, d_p is the proper distance. The integral is carried out from the Lyman limit to the shortest wavelengths on the *rest frame* specific flux f_{λ} . For the integral we will use two Spectral Energy Distributions (SEDs): one described by Mathews & Ferland (1987) and one by Laor et al. (1997a), also reproduced in Fig. 20.

Eq. 4 becomes:

$$r_{\text{BLR}} \approx 93 \cdot (Un_e)_{10}^{-\frac{1}{2}} \cdot f_{\lambda_0, -15}^{\frac{1}{2}} \tilde{Q}_{H,0.1}^{\frac{1}{2}} \zeta(z, 0.3, 0.7) \quad \text{ld} \quad (5)$$

where $\tilde{Q}_H = \int_0^{\lambda_{\text{Ly}}} \tilde{n}_\lambda \lambda d\lambda$, and $\zeta(z, 0.3, 0.7)$ is an interpolation function for d_p as a function of redshift.

\tilde{Q}_H is 0.00963 cmÅ in the case the continuum of Laor et al. (1997) is considered; $\tilde{Q}_H \approx 0.02181$ cmÅ for Mathews & Ferland (1987). We use their average value, since the derived U and n_H are not sensitive to the two different shapes to a first approximation.³

Knowing r_{BLR} we can calculate the M_{BH} assuming virial motions of the gas

$$M_{\text{BH}} = f \frac{\Delta v^2 r_{\text{BLR}}}{G}. \quad (6)$$

or,

$$M_{\text{BH}} = \frac{3}{4G} f_{0.75} (FWHM)^2 r_{\text{BLR}} \quad (7)$$

with the geometry term $f \approx 0.75$, corresponding to $f_{0.75} \approx 1.0$ (Graham et al. 2011, see also Onken et al. 2004 and Woo et al. 2010). Collin et al. (2006) suggest that f is significantly different for Pop.A and B sources; we do not consider here their important result for the sake of comparison with previous work (§10.2). The resulting r_{BLR} and M_{BH} are reported in Columns 7 to 14 of Table 7. Errors are at 2σ confidence level and have been computed propagating

³Since the Laor et al. (1997) continuum produces a fewer ionizing photons, the same value of U is obtained at a smaller distance.

quadratically the major sources of uncertainty. More precisely, in addition to the error on $\log(n_{\text{H}}U)$, the r_{BLR} determination is affected by the uncertainty in the spectrophotometry (specific fluxes of Col. 3 of Tab. 7), and errors on the shape of the ionizing continuum. The two SEDs that we assumed as extreme yield a difference in ionizing photons of a factor 2.2. At a 2σ confidence level this corresponds to an uncertainty of ± 0.065 in logarithm. An additional source of uncertainty affects M_{BH} due to the FWHM determination. Errors on FWHM are quadratically added to the uncertainty on r_{BLR} in the values reported as $\log M_{\text{BH}}$ errors.

10. Discussion

10.1. Previous work

There have been several studies aimed at computing r_{BLR} and M_{BH} . A direct measure of r_{BLR} through reverberation mapping requires an enormous amount of observational effort and has only been applied to a relatively small number of quasars: slightly less than 50 objects with $z \lesssim 0.4$ (Kaspi et al. 2000, 2005, Peterson et al. 2004; Bentz et al. 2010). A second way to measure r_{BLR} uses a less direct method. Kaspi et al. (2000, 2005) and Bentz et al. (2009) used reverberation mapping results to find, in an empirical way, a relationship between r_{BLR} and the optical continuum luminosity at 5100Å,

$$r_{\text{BLR}} \propto L^{\alpha} \tag{8}$$

with $\alpha \approx 0.52$. Vestergaard & Peterson (2006) obtained a similar result for the optical continuum luminosity with an $\alpha \approx 0.50$ and for the UV continuum at 1350\AA , $\alpha \approx 0.53$. These relationships have been used to compute the r_{BLR} not only for nearby objects, but also for high redshift, high luminosity objects. There are other works that use single epoch spectra and the continuum at 3000\AA , obtaining an $\alpha \approx 0.47$ (McLure & Jarvis 2002).

We can rewrite Eq. 6 as

$$M_{\text{BH}} \propto f \frac{\text{FWHM}^2 L^\alpha}{G}. \quad (9)$$

$\text{H}\beta$ is a low ionization strong line whose FWHM has been widely used to determine the M_{BH} for objects mainly up to $z \lesssim 0.9$; above this limit IR spectrometers and large telescopes are needed to cover the redshifted line. For distant objects ($z \sim 2$), an alternative is to use $\text{CIV}\lambda 1549$, a high ionization line emitted in the UV. However, this line should be used with caution because the line is often blueshifted. This means that at least part of this line is likely emitted in an outflow (Sulentic et al. 2007; Richards et al. 2010). Thus the estimation of M_{BH} using $\text{FWHM}(\text{CIV}\lambda 1549)$ tend to be systematically higher than those using $\text{FWHM}(\text{H}\beta)$, especially for objects of Population A.

10.2. Comparison with Vestergaard and Peterson (2006)

Vestergaard & Peterson (2006) used the relationship $r_{\text{BLR}} \propto L^{0.53}$ to obtain the following formula that relates M_{BH} to the $\text{FWHM}(\text{CIV}\lambda 1549)$ and the continuum

luminosity at 1350Å:

$$\log M_{\text{BH}}(\text{CIV}) = \log \left\{ \left[\frac{\text{FWHM}(\text{CIV})}{1000 \text{ km s}^{-1}} \right]^2 \left[\frac{\lambda L_{\lambda}(1350\text{\AA})}{10^{44} \text{ ergs s}^{-1}} \right]^{0.53} \right\} + (6.66 \pm 0.01) - s_{\text{f}}. \quad (10)$$

The scale factor $s_{\text{f}} \approx -0.27$ sets the masses to the f value obtained by Graham et al. (2011). In Cols. 11 and 15 of Table 7 and in Fig. 21 we compare our M_{BH} results with those using Eq. 10. We do not apply corrections for radiation-pressure effects that are likely relevant especially for objects radiating at large Eddington ratio (Netzer 2009; Netzer & Marziani 2010). The difference between this computation and the one reported in Sulentic et al. (2007) is that in the latter work the blueshifted component was not separated from the broad component of CIV λ 1549 just to show how larger values of FWHM(CIV λ 1549) yielded M_{BH} much larger than the ones derived from FWHM(H β) in Pop. A objects.

We compare the masses obtained using our photoionization method with those of Vestergaard & Peterson (2006) in Fig. 21. We use the FWHM of the BC as an estimator of the virial line broadening. **From our results we can see that the masses agree within less than 1σ uncertainty in the luminosity correlation (0.33).** There is a systematic offset of 0.17 ± 0.10 if uncorrected ratios are used. The mass values obtained after correction for low density gas are systematically lower. This happens because the correction increases the product Un_{H} , lowering r_{BLR} and hence M_{BH} . The M_{BH} obtained after corrections are within the error bars. The systematic offset is then 0.13 ± 0.12 . It is important to consider that the computed correction is in many ways a maximum correction. CIII] λ 1909 emission is assumed

to have the same FWHM of SiIII] λ 1892 while it could be significantly narrower; in addition part of the CIII] λ 1909 emission could be due to FeIII λ 1914. In many sources of Pop. A the correction could be ignored altogether. The present results indicate that the Kaspi et al. (2000) relationships can be extended to be used in high redshift objects (or at least until $z \sim 3$) if the FWHM of the core broad line region can be well determined and measured. In order to do this, we need:

- Spectra with S/N high enough to see the profile shape that allows decomposition of the CIV λ 1549 line, especially to separate the blue component from the broad core;
- to follow the methodological considerations explained in §4 .

Fig. 21 should be looked at with two cautions. First, the correlation is dominated by the luminosity dependence of r_{BLR} , used to compute M_{BH} in both cases. Second, the spread of M_{BH} values is small, less than one order of magnitude (and most objects have statistically indistinguishable masses). Our estimated error bars are however smaller compared to the spread expected on the basis of the $r_{\text{BLR}}-L$ correlation which is, according to Vestergaard & Peterson (2006), ± 0.66 at a 2σ confidence level. The two shaded bands of Fig. 21 limit the region where we can expect to find data points on the basis of the $r_{\text{BLR}}-L$ correlation. Clearly, a proper interpretation of the CIV λ 1549 profile may help to reduce the scatter. In any case, our method should provide M_{BH} estimates with somewhat lower uncertainty. It is interesting to note that SDSS J12014+0116 appear at the largest M_{BH} , and the

agreement with the $r_{\text{BLR}}-L$ is very good. The r_{BLR} value of 3C 390.3 we obtain is fairly uncertain due to the low S/N. **The size computed in the present paper is larger than the reverberation mapping derived r_{BLR} for $\text{H}\beta$ and $\text{CIV}\lambda 1549$, although consistent with the value derived from $\text{Ly}\alpha$. 3C 390.3 has the unusual property of having a response time longer in $\text{CIV}\lambda 1549$ than in $\text{H}\beta$, although the large error bars do not exclude that the two lines respond with similar time. This behavior might be related to different physical conditions found for this object.**

10.3. The LIL-BLR

While the existence of high density and low ionization has been invoked since long to explain FeII emission (especially by S. Collin and collaborators, as mentioned in the introduction), we have provided additional evidence that high density and low ionization are indeed diagnosed from emission lines other than FeII blends, and that conditions are the one producing most line emission in extreme Pop. A quasars. Last but not least, both U and n_{H} can be observationally determined with reasonable accuracy from the diagnostic ratios $\text{SiII}\lambda 1814 / \text{SiIII}\lambda 1892$, $\text{SiIV}\lambda 1397 / \text{SiIII}\lambda 1892$, $\text{AlIII}\lambda 1860 / \text{SiIII}\lambda 1892$, and $\text{CIV}\lambda 1549 / (\text{AlIII}\lambda 1860 \text{ or } \text{SiIII}\lambda 1892)$. Metallicity can be also constrained from the previous ratios as well as from $\text{CIV}\lambda 1549 / \text{SiIV}\lambda 1397$. These ratios are pretty well defined, while estimating $\text{CIII}\lambda 1909$ and $\text{FeIII}\lambda 1914$ relative contribution is not relevant to our method (with the exceptions of sources like 3C 390.3). This low ionization BLR (or LIL BLR) has very similar properties to the OI and CaII emitting region identified by Matsuoka et al. (2008). The

LIL-BLR seems to be present in the vast majority of quasars, probably all the ones with significant FeII emission (Marziani et al. 2010). The low values of U could be a consequence of the high density rather than of a far away location of the emitting region. The assumption of a single well defined value of U and n_{H} is probably an idealization even for the LIL-BLR taken alone; however the convergence of emission line ratios toward a well defined point, along with the ability to qualitatively explain FeII and most $\text{H}\beta$ emission, indicate that the LIL-BLR might be a region with a small range of low U and high n_{H} .

Do density and ionization parameter in the LIL BLR converge to a single well defined value with a small dispersion? A tentative answer comes from the values reported in Tab. 6. Excluding 3C390.3, the range U and n_{H} span is not very large (even considering changes in metallicity): less than one order of magnitude around $\log n_{\text{H}} \sim 12.5$, and ionization parameter ~ -2.75 , and the spread is not much larger than the uncertainties in the individual measurements. The product $U \cdot n_{\text{H}}$ seems to be fairly stable. We have $\langle \log(U \cdot n_{\text{H}}) \rangle \approx 9.5$, with a sample dispersion of 0.15 (excluding 3C 390.3). We applied the same method to 14 low- z quasars (Negrete et al. 2010), and we obtain $\langle \log(U \cdot n_{\text{H}}) \rangle \approx 9.7$, with a dispersion of 0.3. Assuming $\log(U \cdot n_{\text{H}}) \approx 9.6$ could be a good approach to estimate M_{BH} if elaborate measurements on $\text{CIV}\lambda 1549$ and $\text{CIII}\lambda 1909$ are not possible, and only a rough estimate of the $\text{SiIII}\lambda 1892$ BC FWHM is available. On the other hand, there is still a major effect of measurement errors on the uncertainty derived for $\log(U \cdot n_{\text{H}})$; instrumental improvements may lead to a significant appreciation of object-by-object diversity.

The $U \cdot n_{\text{H}}$ values reported in Table 6 are not very far from the average value obtained by Padovani and Rafanelli (1988). This is not surprising since the spectra at low and high z seems to show the same diversity, classified through the E1 sequence and the Pop. A/Pop. B distinction. In other words, NLSy1-like sources whose spectrum is similar to I Zw1 appear to be present at high redshift, meaning that the LIL-BLR remains strong and prominent over a wide range of redshifts. A second reason is that Padovani and Rafanelli (1988) considered $\text{H}\beta$. Emission of $\text{H}\beta$ can be significant under a much wider range of U and n_{H} ; however, the $\text{AlIII}\lambda 1860$, $\text{MgII}\lambda 2800$, FeII emitting region should be also a strong producer of $\text{H}\beta$. This region with well-defined physical conditions is expected to be the emitter of the core of $\text{H}\beta$, i.e., the part of the line responding more strongly to continuum changes.

10.3.1. Verification on EW and Line Luminosity

Considering that we have very low ionization parameter values, a legitimate question is whether we have a sufficient number of photons to explain the EW and luminosity of the emission lines. We made a preliminary check of consistency for the EW from CLOUDY simulations. A second, a-posteriori test was to consider the predicted line luminosity assuming the actual luminosity of the quasar, the density and the distance r_{BLR} derived from our method, and spherical geometry.

A remarkable property common to all spectra is the low EW of the emission lines. The extreme source SDSS J120144.36+011611.6 has total $W(\text{CIV}\lambda 1549) \approx 19 \text{ \AA}$, which becomes $\approx 7 \text{ \AA}$ if only the LIL component is considered. The whole 1900 \AA blend has $W \approx 20 \text{ \AA}$; the individual EWs of $\text{SiIII}\lambda 1892$ and $\text{AlIII}\lambda 1860$ are

just a few Å. Similar considerations apply to the other high- z quasars, especially for Pop. A sources. In this case we have $W(\text{CIV}\lambda 1549) \approx 20 - 30$ Å, the equivalent width of the whole $1900 \text{ Å } 30 - 40 \text{ Å}$ including the uncertain contribution of FeIII and CIII] $\lambda 1909$. This has the important implication that the ionization parameter cannot be very large. From our simulations, we deduce that the LIL-BLR $\log U$ is always $\lesssim -2.0$. On the other hand, toward the low U , high density limit emission lines tend to disappear altogether. The predicted EWs become too low to account for the observed EW with a covering factor $f_c \lesssim 0.5$ if $\log U \lesssim -3$. The values obtained after correction $\log U \approx -3.25$ are still possible within the condition of $f_c \lesssim 0.5$ since the CIV $\lambda 1549$ EW is greatly diminished. Cases of very low U are rather indicative of strong metal enhancement than of extremely low ionization level (see §8.1). If we take $\log n_H \approx 12.5$, $\log U = -2.75$, the predicted equivalent width of is $W(\text{CIV}\lambda 1549) \approx 37$ Å for a covering factor 0.5, close to the largest values observed in our quasars. However, The CIV $\lambda 1549$ EW of SDSS J12014+0116 can be accounted for by the values of $\log U \approx -3.00$ and $\log n_H \sim 12.75 - 12.50$.

If we model the BLR with a spherical geometry where the emitting gas covers a fraction f_c of the continuum, CLOUDY computations confirm that the line luminosity can be accounted for. The luminosity at 1700 Å of J00103-0037 is $\log \lambda L_\lambda \approx 46.6$; the predicted luminosity of CIV $\lambda 1549$ is $\log L(\text{CIV}\lambda 1549) \approx 44.5$, under the assumption of $Z = Z_\odot$, $f_c = 0.1$, and Mathews & Ferland continuum shape. The observed CIV $\lambda 1549$ line luminosity of J00103-0037, $\approx 9 \cdot 10^{44}$ ergs s $^{-1}$, is obtained with $f_c \approx 0.3$.

10.3.2. *Analogy with η Carinæ*

The physical conditions we envisage for the BC of quasars find a correspondence in the so-called Weigelt blobs of η Carinæ, located in the equatorial plane of the system, perpendicular to the symmetry axis of the bipolar lobes forming the homunculus nebula (cf. Marziani et al. 2010). Unlike the gas of the bipolar lobes, predominantly shock heated, the Weigelt blobs are believed to be dense gas photoionized by the radiation associated to the central, massive star and to a possible companion (e.g., Johansson et al. 2000; Davidson 2005). The spectrum of the Weigelt blobs shows very weak CIII] λ 1909 along with a prominent line at λ 1914, ascribed to the $z^7P_3^0 \rightarrow a^7S_3$ FeIII transition. The line appears very strong because the upper level is populated by Ly α fluorescence. This very same process is expected to be present also in quasars. Indeed, in I Zw 1, where lines are narrow, and in SDSS J120144.36+011611.6 the peak emission at around 1914 Å is actually visible. The amount of Ly α pumping to the upper level ($z^7P_3^0$) of the UV 34 cannot be estimated through the standard edition of CLOUDY (the relevant levels of the UV 34 multiplets of Fe⁺² ion are not included). Additional photoionization computations including a suitable Fe⁺² model and line transfer should be considered. This is beyond the aim of the present study; we can conclude in a qualitative fashion that the spectrum of the η Carinæ blobs supports a view of the low-ionization part of the BLR that is not conventional: very high density gas, at very low ionization.

11. Conclusions

In this paper we presented new observations of eight high redshift quasars. The spectra were meant to provide high S/N, moderate resolution data on which the C^{IV}λ1549, Si^{III}]λ1892, Al^{III}λ1860, and Si^{II}λ1814 emission line profiles could be accurately analyzed. Line profile fits allowed us to isolate a specific component whose intensity ratios were used to derive consistent values for electron density and ionization parameter. This line component (LIL BC) seems to be emitted predominantly by low ionization, high density gas **in the majority of quasars studied thus far by us.**

These results permitted us to compute the product $n_{\text{H}} \cdot U$ and hence the size of the Broad Line Region and the central black hole mass. The method described in this paper rests on the assumption of photoionization as the mechanism of gas heating; on the assumption of isotropic luminosity, and on line ratios predicted by CLOUDY simulations. The photoionization method explored in this paper offers an estimate of r_{BLR} for each quasar, with some advantages on the r_{BLR} valued derived from the luminosity-size correlation. The luminosity correlation suffers from large scatter and is simply extrapolated to very high luminosity without any support since there are, unfortunately, no conclusive results on reverberation of high luminosity quasars even if heroic efforts are underway (e.g., Trevese et al. 2007, Botti et al. 2010). We found that the black hole masses derived from the computed r_{BLR} and from the virial assumption are in good agreement with the ones derived from the luminosity-size relationship. Actually, Fig. 21 suggests that we might have reduced the errors of the M_{BH} by a factor of two with respect to the expectation from the

Vestergaard & Peterson (2006) relationship.

We repeat that our M_{BH} and r_{BLR} results are based on the product $n_{\text{H}} \cdot U$ and not on values of n_{H} and of U taken separately. It seems that this product converges to two typical ranges of values, one of them associated to low-ionization, high density gas (the LIL-BLR). For our n_{H} and U determinations we do not use ratio $\text{CIII}] \lambda 1909 / \text{SiIII}] \lambda 1892$ except for 3C 390.3. As we discussed in §7.2, this ratio should not be considered at high density because $\text{CIII}] \lambda 1909$ is collisionally quenched if $n_{\text{H}} \gtrsim 10^{10} \text{ cm}^{-3}$. $\text{CIII}] \lambda 1909$ is produced in conditions that are very different from the ones we found for the LIL-BLR. While the method can be applied to most quasars, the application seems to be especially straightforward to quasars whose spectrum is like SDSS J120144.36+011611.6 (if high metallicity is properly taken into account) or, at the other end, 3C390.3. In the first case we have dominance by the LIL-BLR, in the second case the LIL-BLR seems to be completely absent and physical conditions look radically different: high ionization and moderate density. An inspection of SDSS spectra covering both the 1900 Å blend and $\text{CIV} \lambda 1549$ (up to $z \approx 3.5$) shows that SDSS J120144.36+011611.6 has many replicas at high redshift, accounting for at least a few percent of all quasars. These high-metallicity objects should be the first candidates to expand black hole mass computations to high redshift without relying on the $r_{\text{BLR}} - L$ correlation.

To apply the photoionization method in the most effective way, determining n_{H} and U with the lowest uncertainty, spectral data should be of moderate resolution ($\lambda/\Delta\lambda \sim 1000$) as well as of high S/N. If the $\text{SiII} \lambda 1814$ line can be measured in an accurate way, it would be possible to derive independent estimates of U , n_{H} , and

Z/Z_{\odot} in most quasars.

Especially the most extreme (in terms of $\text{AlIII}\lambda 1860$ strength) objects in bin A3 and A2 hold the promise to make possible an independent estimate of n_{H} , U , and metallicity. Clearly, objects in bin A1 resembling their median spectrum are not well suited for an application of the method. Also, any source with $\text{CIII}\lambda 1909 / \text{SiIII}\lambda 1892 > 1$ is subject to a large correction. In light of the many uncertainty, an average value of the product Un (obtained from the objects of the other spectral types) could be considered. Pop. B objects should not be avoided entirely, especially whenever $\text{SiIII}\lambda 1892 \gtrsim \text{CIII}\lambda 1909$ after VBC removal.

The present exploratory analysis emphasized several sources of uncertainty. However, the parameter needed for r_{BLR} and M_{BH} computation, the product Un_{H} , seems to be fairly stable and well-defined. Even with an error of a 0.3 in logarithm, the square root will be subject to a 0.15 uncertainty in logarithm, much lower than the uncertainty associated with the r_{BLR} luminosity correlation. The large intrinsic spread of the correlation at low luminosity, its uncertain extrapolation at very high luminosity make preferable a one-by-one determination based on physical properties of an emitting region that remains similar to itself.

A. Negrete and D. Dultzin acknowledge support from grant IN111610-3 PAPIIT, DGAPA UNAM. Funding for the SDSS and SDSS-II has been provided by the Alfred P. Sloan Foundation, the Participating Institutions, the National

Science Foundation, the U.S. Department of Energy, the National Aeronautics and Space Administration, the Japanese Monbukagakusho, the Max Planck Society, and the Higher Education Funding Council for England. The SDSS Web Site is <http://www.sdss.org>. The SDSS is managed by the Astrophysical Research Consortium for the Participating Institutions listed at the SDSS Web Site.

References

- Aoki, K., Yoshida, M. 1999, ASPC, 162, 385
- Appenzeller, I., et al. 1998, The Messenger, 94, 1
- Bachev et al. 2004, ApJ, 617, 171
- Baldwin, Ferland, Korista and Verner, 1995, ApJ, 455, L119
- Baldwin J. A. et al. 1996, ApJ, 461, 682
- Baskin, A. & Laor, A. 2005, MNRAS, 356, 1029
- Bentz, M. C., et al. 2010, ApJ, 716, 993
- Bevington, P. R. 1969, Data reduction and error analysis for the physical sciences, New York: McGraw-Hill, 1969
- Boroson, T.A. & Green, R.F., 1992, ApJS, 80, 109
- Botti, I., Lira, P., Netzer H., Kaspi, S. 2010, IAU Symposium, 267, 198
- Bottorff M.C. & Gary J.F. 2000, MNRAS, 316, 103

- Bruhweiler, F. & Verner, E., 2008, ApJ, 675, 83
- Clavel, J., et al. 1991, ApJ, 366, 64
- Clayton, D.D., 1983, Principles of Stellar Evolution & Nucleosynthesis,
Chicago:University of Chicago Press, Ch. 7
- Collin-Souffrin S. et al. 1988, MNRAS, 232, 539
- Collin, S., et al. 2006, A&A, 456, 75
- Constantin A. et al. 2002, ApJ, 565, 50
- Davidson, K. & Netzer, H., 1979, Rev. Mod. Phys. 51, 715
- Davidson, K. 2005, ASPC, 332, 101
- Dumont, A. M. & Mathez, G., 1981, A&A, 102, 1
- Dumont, A. M, & Collin-Souffrin, S., 1990 A&A 229, 292
- Edlén & Swings, 1942, ApJ, 95, 532
- Ekberg J.O. 1993, A&AS, 101, 1
- Espey, B. R., Carswell, R. F., Bailey, J. A., Smith, M. G., & Ward, M. J. 1989,
ApJ, 342, 666
- Evans & Koratkar 2004, ApJS, 150, 73
- Francis P.J. et al. 1991, ApJ, 373, 465
- Feibelman, W.A., and Aller, L.H., 1987, ApJ, 319, 407
- Feldman U. et al. 1992, ApJS, 81, 387

- Ferland G. J. et al. 1998, PASP, 110, 761
- Gaskell, C. M. 1982, ApJ, 263, 79
- Gaskell, M. et al. 1999, ASPC, 175, 423
- Graham, A. W. et al. 2011, MNRAS, 48
- Hartig, G. F. & Baldwin, J. A. 1986, ApJ, 302, 64
- Hu, C., et al. 2008, ApJ, 687, 78
- Johansson S. et al. 2000, A&A, 361, 977
- Joly, M., 1987, A&A, 184,33
- Kaspi et al. 2000, ApJ, 533, 631
- Kaspi et al. 2005, ApJ, 629, 61
- Kriss G.A., 1994, ASPC, 61, 437
- Korista K. et al. 1997, ApJS, 108, 401
- Kuraszkiewicz, J. K. et al. 2002 ApJS, 143,257
- Laor A. et al. 1994, ApJ, 420, 110
- Laor A. et al. 1997a, ApJ, 477, 93
- Laor A. et al. 1997b, ApJ, 489, 656
- Leitherer, C., et al. 1999, ApJS, 123, 2
- McLure & Jarvis 2002, MNRAS, 337, 109

- Marziani, P., Sulentic, J. W., Dultzin-Hacyan, D., Calvani, M., & Moles, M. 1996, ApJS, 104, 37
- Marziani P. et al. 2003, ApJS, 145, 199
- Marziani P. et al. 2003b, MNRAS, 345, 1133
- Marziani P. et al. 2008, RMAA serie de conferencias, 32, 69
- Marziani P. et al. 2009, A&A, 495, 83
- Marziani P. et al. 2010, MNRAS, arXiv:1007.3187v1
- Matsuoka, Y., Kawara, K., & Oyabu, S. 2008, ApJ, 673, 62
- Mathews & Ferland 1987, ApJ, 323, 456
- Metzroth, K. G., Onken, C. A., Peterson B. M. 2006, ApJ, 647, 901
- Negrete, C. A., Dultzin, D., Marziani, P., Sulentic J. W. 2010, ApJL, submitted
- Netzer, H., & Trahtenbrot, B. 2007, ApJ, 654, 754
- Netzer, H. 2009, ApJ, 695, 793
- Netzer, H. & Marziani, P. 2010, ApJ, in press, arXiv:1006.3553v2
- Onken, C. A., Peterson, B. M. 2002, ApJ, 572, 746
- Onken, C. A., Ferrarese, L., Merritt, D., Peterson, B. M., Pogge, R. W., Vestergaard, M., & Wandel, A. 2004, ApJ, 615, 645
- Osterbrock, D. E., & Ferland, G. J. 2006, Astrophysics of gaseous nebulae and active galactic nuclei, 2nd. ed. by D.E. Osterbrock and G.J. Ferland. Sausalito,

- CA: University Science Books, 2006,
- Padovani, P., 1988, A&A, 192, 9
- Padovani, P. & Rafanelli, P. 1988, A&A, 205, 53
- Padovani, P., Burg, R.I., Edelson, R.A., 1990, ApJ, 353, 438
- Peterson B. M. et al. 2004, ApJ, 613, 682.
- Punsly, B. 2010, ApJ, 713, 232
- Rees M.J. 1987, MNRAS, 228, 47
- Richards, G. T., et al. 2010, arXiv preprint 2010arXiv1011.2282R
- Richards, G. T., Vanden Berk, D. E., Reichard, T. A., Hall, P. B., Schneider, D. P.,
SubbaRao, M., Thakar, A. R., & York, D. G. 2002, AJ, 124, 1
- Sigut T.A. et al. 2004, ApJ, 611, 81
- Sulentic J. W. et al. 2000, ApJ, 536, L5
- Sulentic J. W. et al. 2001, AIP Conference Proceedings, 599, 963
- Sulentic J. W. et al. 2002, ApJ, 566, 71
- Sulentic J. W. et al. 2006, RMxAA, 42, 23
- Sulentic J. W. et al. 2006b, A&A, 456, 929
- Sulentic J. W. et al. 2007, ApJ, 666, 757.
- Trevese, D., Paris, D., Stirpe, G. M., Vagnetti, F., and Zitelli, V. 2007, A&A, 470,
491

- Tytler, D., & Fan, X.-M. 1992, ApJS, 79, 1
- Vanden Berk et al. 2001, AJ, 122, 549
- Verner E. et al. 1999, ApJS, 120, 101
- Verner E. et al. 2003, ApJ, 592, 59
- Verner E. et al. 2004, ApJ, 611, 780
- Vestergaard M. and Peterson B.M. 2006, ApJ, 641, 689.
- Vestergaard & Wilkes, 2001, ApJS, 134, 1
- Wandel, A., Peterson, B. M., Malkan, M. 1999, ApJ, 526, 579
- Wills, B. J., et al. 1999, ApJ, 515, L53
- Woo, J.-H., et al. 2010, ApJ, 716, 269
- Woosley, S. E., Weaver, T. A. 1995, ApJS, 101, 181
- Zamfir, S., Sulentic, J. W., Marziani, P., & Dultzin, D. 2010, MNRAS, 403, 1759

Table 1. Line Components in the $\lambda 1900$ blend.

Ion	λ Å	X eV	$E_l - E_u$ eV	Transition	A_{ki} s ⁻¹	n_c cm ⁻³	Note
Si II	1808.00	8.15	0.000 - 6.857	$^2D_{3/2}^o \rightarrow ^2P_{1/2}$	$2.54 \cdot 10^6$...	1
Si II	1816.92	8.15	0.036 - 6.859	$^2D_{5/2}^o \rightarrow ^2P_{3/2}$	$2.65 \cdot 10^6$...	1
Al III	1854.716	18.83	0.000 - 6.685	$^2P_{3/2}^o \rightarrow ^2S_{1/2}$	$5.40 \cdot 10^8$...	1
Al III	1862.790	18.83	0.000 - 6.656	$^2P_{1/2}^o \rightarrow ^2S_{1/2}$	$5.33 \cdot 10^8$...	1
[Si III]	1882.7	16.34	0.000 - 6.585	$^3P_2^o \rightarrow ^1S_0$	0.012	$6.4 \cdot 10^4$	1,2,3
Si III]	1892.03	16.34	0.000 - 6.553	$^3P_1^o \rightarrow ^1S_0$	16700	$2.1 \cdot 10^{11}$	1,4,5
[C III]	1906.7	24.38	0.000 - 6.502	$^3P_2^o \rightarrow ^1S_0$	0.0052	$7.7 \cdot 10^4$	1,2,6
C III]	1908.734	24.38	0.000 - 6.495	$^3P_1^o \rightarrow ^1S_0$	114	$1.4 \cdot 10^{10}$	1,2,4,5
Fe III	1914.066	16.18	3.727 - 10.200	$z^7P_3^o \rightarrow a^7S_3$	$6.6 \cdot 10^8$...	7

Note. — All wavelengths are in vacuum. (1) Ralchenko, Yu., Kramida, A.E., Reader, J., and NIST ASD Team (2008). NIST Atomic Spectra Database (version 3.1.5). Available at: <http://physics.nist.gov/asd3>. 2: Feibelman & Aller (1987). 3: n_c computed following Shaw & Dufour (1995). 4: Morton (1991). 5: Feldman (1992). 6: Zheng (1988). 7: Wavelength and A_{ki} from Ekberg (1993), energy levels from Edlén and Swings (1942).

Table 2. Basic Properties of Sources and Log of Observations.

Object name	m_B	z	Line	M_B	Flux 6cm (mJy)	Date	DIT	N_{exp}	Airmass	S/N
(1)	(2)	(3)	(4)	(5)	(6)	(7)	(8)	(9)	(10)	(11)
J00103-0037	18.39	3.1546	1	-25.68	0.40	2006-11-08	1139	3	1.16, 1.13, 1.11	60
J00521-1108	18.70	3.2364	2	-25.39	0.43	2007-01-01	1199	3	1.15, 1.21, 1.29	41
J01225+1339	18.24	3.0511	1	-25.80	*	2006-11-08	1259	2	1.36, 1.32	92
J02287+0002	18.20	2.7282	1	-25.72	0.35	2006-12-16	1259	2	1.10, 1.12	67
J02390-0038	18.68	3.0675	1	-25.36	0.43	2006-11-07	1199	3	1.35, 1.46, 1.60	57
J03036-0023	17.65	3.2319	1	-26.44	0.34	2006-12-16	1259	2	1.11, 1.14	88
J20497-0554	18.29	3.1979	1	-25.79	*	2006-11-04	1259	2	1.52, 1.70	54
J23509-0052	18.67	3.0305	1	-25.36	0.41	2006-11-07	1199	3	1.10, 1.11, 1.14	62

*Not in FIRST

Table 3. Line Fluxes ^a

Object	CII λ 1909			SiIV λ 1814			CIV λ 1549			SiIV λ 1397		
	BC	VBC	SiII λ 1892	AlIII λ 1860	SiIV λ 1814	BC	blue	VBC	BC	blue	VBC	VBC
J00103-0037	4.99 \pm 2.11	1.18 \pm 1.38 *	2.91 \pm 1.03	1.99 \pm 0.81	1.13 \pm 0.82 :	14.25 \pm 8.34	6.32 \pm 1.80	8.71 \pm 8.24	4.27 \pm 2.38	0.78 \pm 1.52	0.54 \pm 0.89	...
J00521-1108	3.08 \pm 0.36	0.01 \pm 0.12 *	2.77 \pm 0.66	1.55 \pm 0.85	1.06 \pm 0.90	10.89 \pm 2.37	1.40 \pm 2.23	8.27 \pm 2.63
J01225+1339	10.71 \pm 1.35	...	8.26 \pm 1.33	4.35 \pm 2.09	1.01 \pm 0.98	22.73 \pm 6.04	14.21 \pm 1.52	...	11.21 \pm 2.93	6.66 \pm 1.93
J02287+0002 ⁽¹⁾	5.28 \pm 1.56	0.01 \pm 0.02 *	4.70 \pm 2.01	2.29 \pm 1.13	0.98 \pm 0.79	7.64 \pm 5.00	7.66 \pm 2.32	0.77 \pm 1.63 *	4.96 \pm 1.04	1.35 \pm 0.80	0.43 \pm 0.56	...
J02287+0002 ⁽²⁾	6.86 \pm 1.56	0.02 \pm 0.02 *	2.78 \pm 2.01	1.77 \pm 1.13	0.94 \pm 0.79	11.48 \pm 5.00	2.99 \pm 2.32	0.64 \pm 1.63 *	4.88 \pm 1.04	1.24 \pm 0.80	0.57 \pm 0.56	...
J02390-0038	3.57 \pm 0.78	1.26 \pm 0.88	3.50 \pm 0.40	2.41 \pm 0.64	0.90 \pm 0.83	7.51 \pm 1.25	7.92 \pm 1.37	2.04 \pm 1.52	2.64 \pm 0.53	1.49 \pm 0.81	0.23 \pm 0.39	...
J03036-0023	13.24 \pm 1.09	...	11.82 \pm 1.21	5.17 \pm 1.48	1.53 \pm 1.16 :	29.46 \pm 3.54	20.60 \pm 3.34	...	11.13 \pm 1.86	7.37 \pm 4.12
J20497-0554	8.04 \pm 1.09	...	7.43 \pm 0.56	3.01 \pm 1.25	1.52 \pm 1.51 :	18.39 \pm 2.17	9.23 \pm 2.24	...	6.65 \pm 2.51	1.95 \pm 1.06
J23509-0052	5.24 \pm 1.21	...	4.61 \pm 1.62	1.50 \pm 0.50	0.40 \pm 0.36	9.24 \pm 1.17	7.80 \pm 2.36	...	3.61 \pm 1.49	2.93 \pm 1.34
Extreme Objects												
J12014+01161	5.52 \pm 1.07	...	16.16 \pm 5.90	14.03 \pm 2.54	4.90 \pm 2.95	21.18 \pm 12.48	29.37 \pm 9.98	...	18.45 \pm 6.55	11.81 \pm 9.08
3C 390.3	3.74 \pm 1.15	4.30 \pm 0.68	2.32 \pm 0.43	0.23 \pm 0.32 *	0.40 \pm 0.48 *	30.04 \pm 4.99	...	56.44 \pm 10.66

Note. — (a) Units are 10^{-14} ergs s $^{-1}$ cm $^{-2}$ Å $^{-1}$. (1) Considering $z_{OI\lambda 1304}$. (2) Considering $z_{CII\eta\lambda 1909}$. (.) SiIV λ 1814 approximated values due the line is affected by telluric absorptions (see Fig. 1). We do not measure SiIV λ 1397 for J00521-1108 and 3c390.3 because they have low S/N. (*) Consistent with no emission.

Table 4. Weak lines around C IV $\lambda 1549$. ^a

Object	N IV] $\lambda 1486$	Si II $\lambda 1533$	He II $\lambda 1640$	
			<i>BC</i>	<i>blue</i>
J00103-0037	2.4 ± 1.9	1.1 ± 0.8	1.3 ± 0.4	2.0 ± 1.8
J00521-1108	0.1 ± 0.2	1.1 ± 1.1	1.6 ± 1.2	0.1 ± 0.2
J01225+1339	...	1.0 ± 1.8	3.2 ± 3.4	4.3 ± 1.8
J02287+0002 ⁽¹⁾	...	1.0 ± 0.8	0.3 ± 0.1	0.2 ± 0.2
J02287+0002 ⁽²⁾	...	0.9 ± 0.8	0.2 ± 0.1	0.0 ± 0.2
J02390-0038	0.5 ± 0.9	0.9 ± 0.9	0.2 ± 0.4	1.6 ± 1.1
J03036-0023	...	1.5 ± 1.2	0.5 ± 0.5	9.2 ± 3.4
J20497-0554	0.3 ± 0.6	1.5 ± 1.5	1.8 ± 0.8	4.6 ± 2.7
J23509-0052	...	0.4 ± 0.4	0.2 ± 0.9	2.5 ± 1.6
Extreme Objects				
J12014+01161	3.0 ± 3.5	4.9 ± 5.8	1.5 ± 1.7	10.3 ± 9.2
3C 390.3	5.6 ± 2.7	1.6 ± 1.5	2.8 ± 1.5	...

Note. — (a) Units are 10^{-14} ergs s⁻¹ cm⁻² Å⁻¹. (1) Considering $z_{OI\lambda 1304}$. (2) Considering $z_{CIII]\lambda 1909}$. We do not show He II $\lambda 1640_{VBC}$ because is very weak, when is considered.

Table 5. Equivalent Widths.

Object	CIII] λ 1909 _{BC}	CIII] λ 1909 _{Tot}	SiII] λ 1892	AlII] λ 1860	SiII] λ 1814	CIV] λ 1549 _{BC}	CIV] λ 1549 _{Tot}	SiIV] λ 1397 _{BC}	SiIV] λ 1397 _{Tot}
J00103-0037	13.7 \pm 5.8	17.1 \pm 7.2	7.9 \pm 3.0	5.3 \pm 2.8	2.9 \pm 2.5 :	29.0 \pm 16.1	59.6 \pm 24.4	7.4 \pm 4.32	9.68 \pm 6.74
J00521-1108	8.2 \pm 1.5	8.2 \pm 2.4	7.3 \pm 2.5	4.0 \pm 2.6	2.6 \pm 3.1	21.0 \pm 18.9	40.1 \pm 26.8
J01225+1339	15.3 \pm 3.5	...	11.6 \pm 3.1	6.0 \pm 3.6	1.4 \pm 2.3	25.5 \pm 9.1	41.6 \pm 9.7	11.1 \pm 3.95	17.74 \pm 4.71
J02287+0002 ⁽¹⁾	15.9 \pm 5.3	15.9 \pm 5.3	14.1 \pm 6.6	6.8 \pm 4.0	2.9 \pm 2.6	20.4 \pm 10.5	42.9 \pm 16.8	12.7 \pm 3.04	17.30 \pm 4.03
J02287+0002 ⁽²⁾	20.5 \pm 5.3	20.5 \pm 5.3	8.3 \pm 6.6	5.2 \pm 4.0	2.7 \pm 2.6	30.8 \pm 10.5	40.6 \pm 16.8	12.7 \pm 3.04	17.85 \pm 4.03
J02390-0038	10.8 \pm 3.3	14.7 \pm 4.5	10.4 \pm 2.0	7.0 \pm 2.4	2.5 \pm 2.5	16.3 \pm 4.1	37.7 \pm 7.0	4.9 \pm 1.32	11.72 \pm 4.15
J03036-0023	12.4 \pm 1.8	...	10.9 \pm 1.8	4.6 \pm 1.6	1.3 \pm 1.1 :	19.7 \pm 3.7	33.3 \pm 4.8	6.4 \pm 1.46	10.71 \pm 2.94
J20497-0554	15.5 \pm 3.5	...	14.1 \pm 2.3	5.6 \pm 2.9	2.7 \pm 2.9 :	25.4 \pm 5.6	38.1 \pm 7.1	8.0 \pm 3.75	10.34 \pm 4.04
J23509-0052	15.8 \pm 4.0	...	13.7 \pm 5.3	4.4 \pm 1.8	1.1 \pm 0.9	22.0 \pm 4.2	40.5 \pm 10.6	7.7 \pm 3.73	14.02 \pm 5.10
Extreme Objects									
J12014+0116	2.9 \pm 0.9	...	8.4 \pm 4.1	7.1 \pm 2.0	2.4 \pm 1.9	8.2 \pm 5.6	19.4 \pm 7.4	6.03 \pm 2.76	9.85 \pm 4.37
3C 390.3	13.1 \pm 4.3	28.4 \pm 6.2	7.9 \pm 3.3	0.7 \pm 0.8	1.2 \pm 1.3	49.1 \pm 8.1	147.2 \pm 19.4

Note. — (1) Considering $z_{OI\lambda 1304}$. (2) Considering $z_{CIII\lambda 1909}$. (:) SiII] λ 1814 approximated values due the line is affected by telluric absorptions.

Table 6. Hydrogen Density and Ionization Parameter.

Object	$\text{Log} n_H$				$\text{Log} U$				$\text{Log} n_H \cdot U$			
	$1Z_\odot$	$1Z_\odot$ low dens	$5Z_\odot$	$5Z_\odot$ low dens	$1Z_\odot$	$1Z_\odot$ low dens	$5Z_\odot$	$5Z_\odot$ low dens	$1Z_\odot$	$1Z_\odot$ low dens	$5Z_\odot$	$5Z_\odot$ low dens
J00103-0037 *	12.50 ± 0.17	-2.79 ± 0.19	9.71 ± 0.22
J00521-1108	12.43 ± 0.26	12.84 ± 0.23	-2.86 ± 0.15	-3.00 ± 0.11	9.58 ± 0.26	9.85 ± 0.22
J00103-0037 *	12.50 ± 0.17	-2.79 ± 0.19	9.71 ± 0.22
J00521-1108	12.43 ± 0.26	12.84 ± 0.23	-2.86 ± 0.15	-3.00 ± 0.11	9.58 ± 0.26	9.85 ± 0.22
J01225+1339	12.45 ± 0.22	13.24 ± 0.20	11.47 ± 0.28	12.62 ± 0.25	-2.96 ± 0.09	-3.42 ± 0.18	-1.83 ± 0.11	-2.79 ± 0.68	9.49 ± 0.21	9.82 ± 0.23	9.64 ± 0.27	9.83 ± 0.66
J02287+0002 ⁽¹⁾	12.35 ± 0.16	...	11.64 ± 0.33	12.28 ± 0.28	-2.81 ± 0.28	...	-2.33 ± 0.25	-2.58 ± 0.98	9.55 ± 0.28	...	9.31 ± 0.36	9.70 ± 0.94
J02287+0002 ⁽²⁾	12.47 ± 0.16	-2.81 ± 0.28	9.67 ± 0.28
J02390-0038	12.75 ± 0.12	13.42 ± 0.21	11.97 ± 0.15	13.20 ± 0.13	-3.18 ± 0.05	-3.60 ± 0.07	-2.19 ± 0.08	-3.29 ± 0.13	9.57 ± 0.11	9.82 ± 0.20	9.78 ± 0.15	9.91 ± 0.15
J03036-0023	12.32 ± 0.14	12.92 ± 0.15	-2.92 ± 0.06	-3.34 ± 0.05	9.40 ± 0.14	9.58 ± 0.15
J20497-0554	12.26 ± 0.25	12.82 ± 0.18	-2.89 ± 0.12	-3.29 ± 0.13	9.37 ± 0.25	9.53 ± 0.19
J23509-0052	12.13 ± 0.24	12.90 ± 0.17	10.86 ± 0.23	12.12 ± 0.58	-2.89 ± 0.09	-3.51 ± 0.21	-1.93 ± 0.13	-2.99 ± 0.82	9.24 ± 0.24	9.39 ± 0.23	8.93 ± 0.23	9.13 ± 0.86
Extreme Objects												
J12014+01161	12.81 ± 0.29	12.95 ± 0.16	12.34 ± 0.11	12.90 ± 0.42	-2.85 ± 0.18	-2.87 ± 0.08	-2.41 ± 0.25	-3.20 ± 0.58	9.97 ± 0.30	10.09 ± 0.16	9.93 ± 0.25	9.70 ± 0.62
3C 390.3	10.05 ± 0.34	-1.48 ± 0.34	8.57 ± 0.41

Note. — We also show the values considering the correction by the contribution of low density regions (§7.3), $Z = 5Z_\odot$ (§8.1), and $Z = 5Z_\odot$ with the correction by the contribution of low density regions. (1) Considering $z_{O\text{I}\lambda 1304}$. (2) Considering $z_{C\text{III}\lambda 1909}$. (*) For J00103-0037 the correction is too large to be reliable. We show in bold numbers the ones that we consider the best.

Table 7. The Size of the Broad Line Region and the Black Hole Masses.

Object	$d_p [Mpc]$		$f(1700\text{\AA})^a$		$f(1350\text{\AA})^a$		FWHM _{BC}	Pop.	$\text{Log}(r_{BLR}) [\text{cm}]^b$				$\text{Log}(M_{BH}) [M_\odot]^b$						
	X_{10}^{15}	(2)	(3)	X_{10}^{-15}	(4)	(5)			(6)	original	low dens	(8)	(9)	$5Z_\odot$	$5Z_\odot$ low dens	original	low dens	(12)	(13)
(1)	(2)	(3)	(4)	(5)	(6)	(7)	(8)	(9)	(10)	(11)	(12)	(13)	(14)	(15)					
J00103-0037	6.51	4.8 ± 1.0	6.8 ± 1.4	4500 ± 800	B	18.10 ± 0.12	9.16 ± 0.20	9.11					
J00521-1108	6.59	6.1 ± 1.5	8.8 ± 2.1	5300 ± 1600	B	18.23 ± 0.14	18.09 ± 0.13	9.43 ± 0.30	9.29 ± 0.29	9.32					
J01225+1339	6.42	8.1 ± 1.6	10.9 ± 2.2	4400 ± 1000	A [†]	18.32 ± 0.12	18.16 ± 0.13	18.25 ± 0.15	18.15 ± 0.33	9.36 ± 0.23	9.20 ± 0.23	9.29 ± 0.25	9.19 ± 0.39	9.19					
J02287+0002 (1)	6.09	7.4 ± 2.7	8.4 ± 3.0	4700 ± 1000	A [†]	18.25 ± 0.16	...	18.37 ± 0.20	18.17 ± 0.48	9.35 ± 0.25	...	9.47 ± 0.27	9.27 ± 0.51	9.17					
J02287+0002 (2)						18.19 ± 0.16	9.29 ± 0.25						
J02390-0038	6.45	6.9 ± 2.1	9.9 ± 3.0	5400 ± 1000	B	18.25 ± 0.09	18.12 ± 0.12	18.14 ± 0.10	18.08 ± 0.10	9.46 ± 0.18	9.34 ± 0.20	9.36 ± 0.19	9.30 ± 0.19	9.35					
J03036-0023	6.58	20.5 ± 5.7	30.0 ± 8.4	3700 ± 600	A	18.58 ± 0.10	18.49 ± 0.10	9.47 ± 0.17	9.38 ± 0.17	9.30					
J20497-0554	6.55	6.6 ± 1.3	9.5 ± 1.9	3800 ± 600	A	18.34 ± 0.13	18.26 ± 0.11	9.25 ± 0.19	9.17 ± 0.18	9.04					
J23509-0052	6.40	4.8 ± 1.0	6.1 ± 1.2	3600 ± 800	A	18.33 ± 0.13	18.25 ± 0.12	18.49 ± 0.13	18.38 ± 0.43	9.19 ± 0.23	9.12 ± 0.23	9.35 ± 0.23	9.25 ± 0.47	8.88					
Extreme Objects																			
J12014+01161	6.58	21.8 ± 2.3	31.9 ± 3.2	4000 ± 800	A	18.31 ± 0.15	18.25 ± 0.09	18.33 ± 0.13	18.44 ± 0.31	9.26 ± 0.23	9.20 ± 0.19	9.28 ± 0.22	9.40 ± 0.43	∞					
3C 390.3	0.24	4.2 ± 0.7	9.9 ± 1.6	6400 ± 2200	B	17.23 ± 0.21	8.60 ± 0.37	7.99					

Note. — (a) Units of the flux at 1350 and 1700Å are in ergs s⁻¹ cm⁻² Å⁻¹. (b) The showed values are the average ± 0.17 dex of the computation using both SED of Laor (1997) and Mathews & Ferland (1987) (see Fig. 20. (c) We show the comparison between our computations and those using the Vestergaard & Peterson (2006) mehtod. They report an uncertainty of 0.66 dex. (†) According to the FWHM it is clasified as pop B, but has other spectral characteristics of pop. A objects. See §5. (1) Considering $z_{OII}\lambda 1304$. (2) Considering $z_{CIII}\lambda 1909$

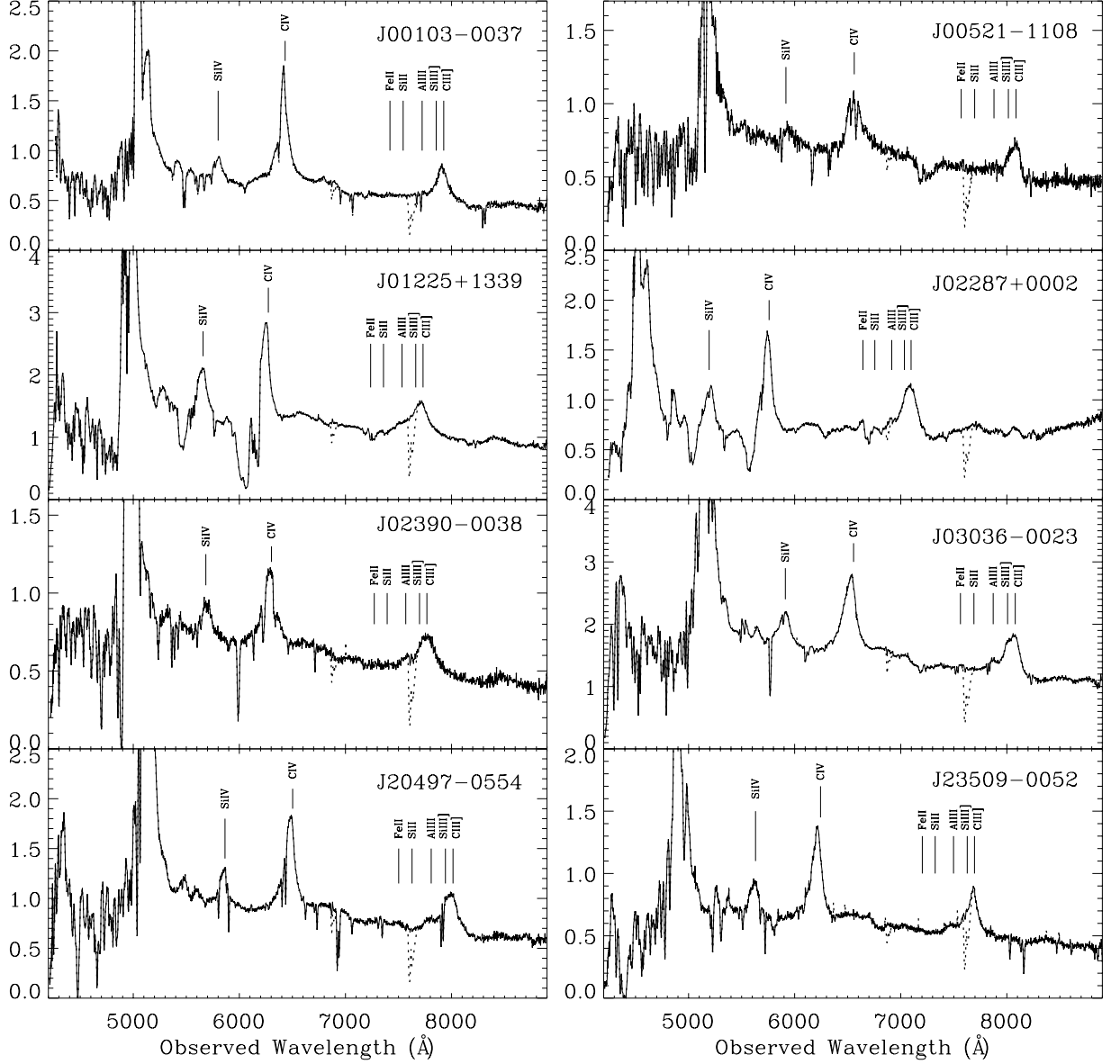


Fig. 1.— Sample of 8 VLT spectra. Abscissa is observed wavelength in Å, ordinate is specific flux in units 10^{-16} ergs s $^{-1}$ cm $^{-2}$ Å $^{-1}$ corrected for Milky Way Galactic extinction. The superimposed dotted line is before atmospheric bands subtraction. We show the positions of the lines of our interest CIII]λ1909, SiIII]λ1892, AlIIIλ1860, SiIIλ1814, FeIIλ1787, CIVλ1549 and SiIVλ1397. J01225+1339 and J02287 are BAL quasars.

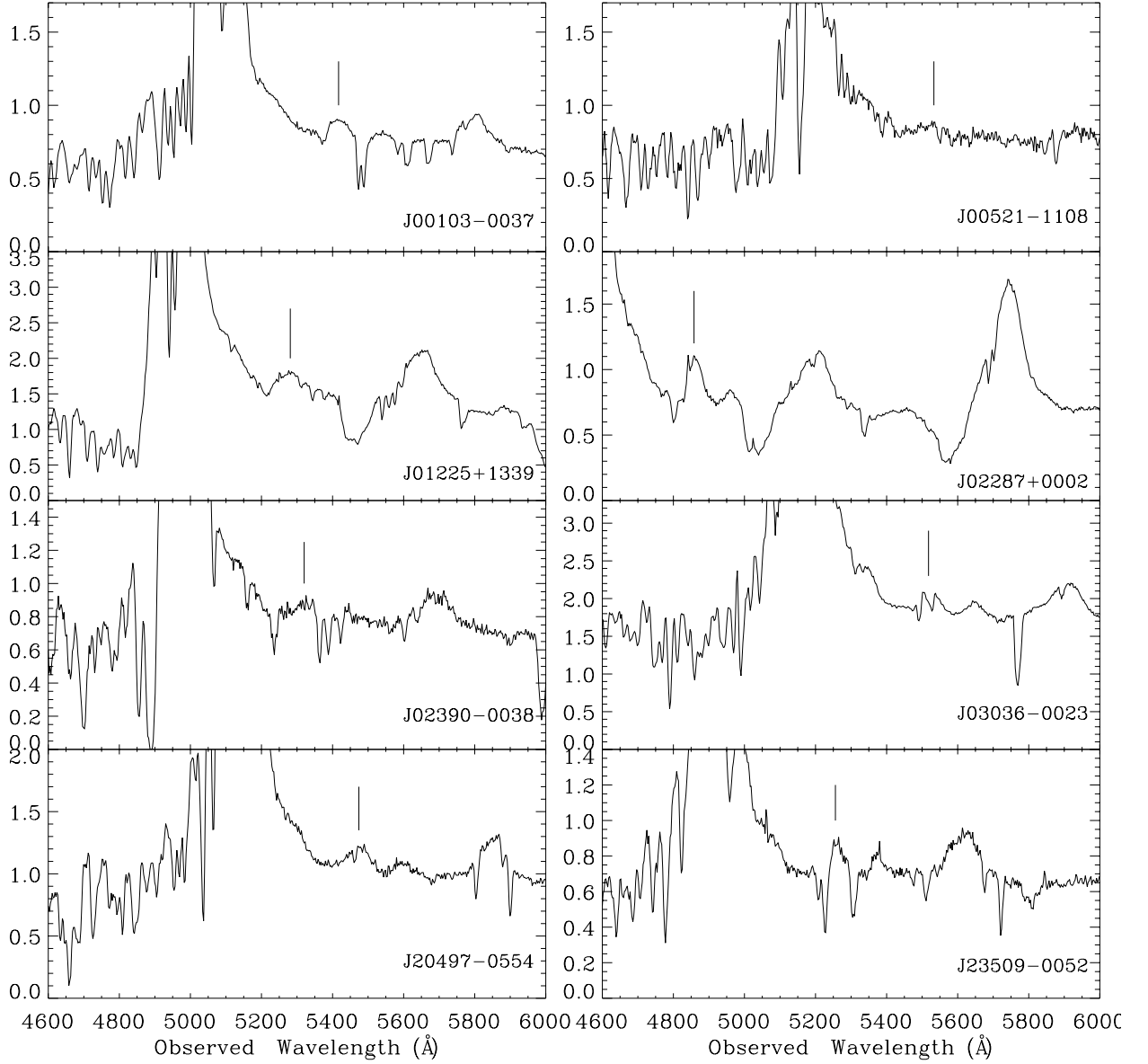


Fig. 2.— $\text{OI}\lambda 1304.8$ used to place the restframe showed by the mark. Abscissa is rest frame wavelength in \AA , ordinate is specific flux in units $10^{-16} \text{ ergs s}^{-1} \text{ cm}^{-2} \text{ \AA}^{-1}$ corrected for Milky Way Galactic extinction. In J00521-1108 and J02390-0038 the peak of $\text{OI}\lambda 1304.8$ is not observed clearly. In J00103-0037, J02287+0002 and J20497-0554, the redshift results, using both $\text{OI}\lambda 1304.8$ and $\text{CIII]}\lambda 1909$, are ambiguous. In J01225+1339, J03036-0023 and J23509-0052, the redshifts obtained using $\text{OI}\lambda 1304.8$ or $\text{CIII]}\lambda 1909$ are consistent.

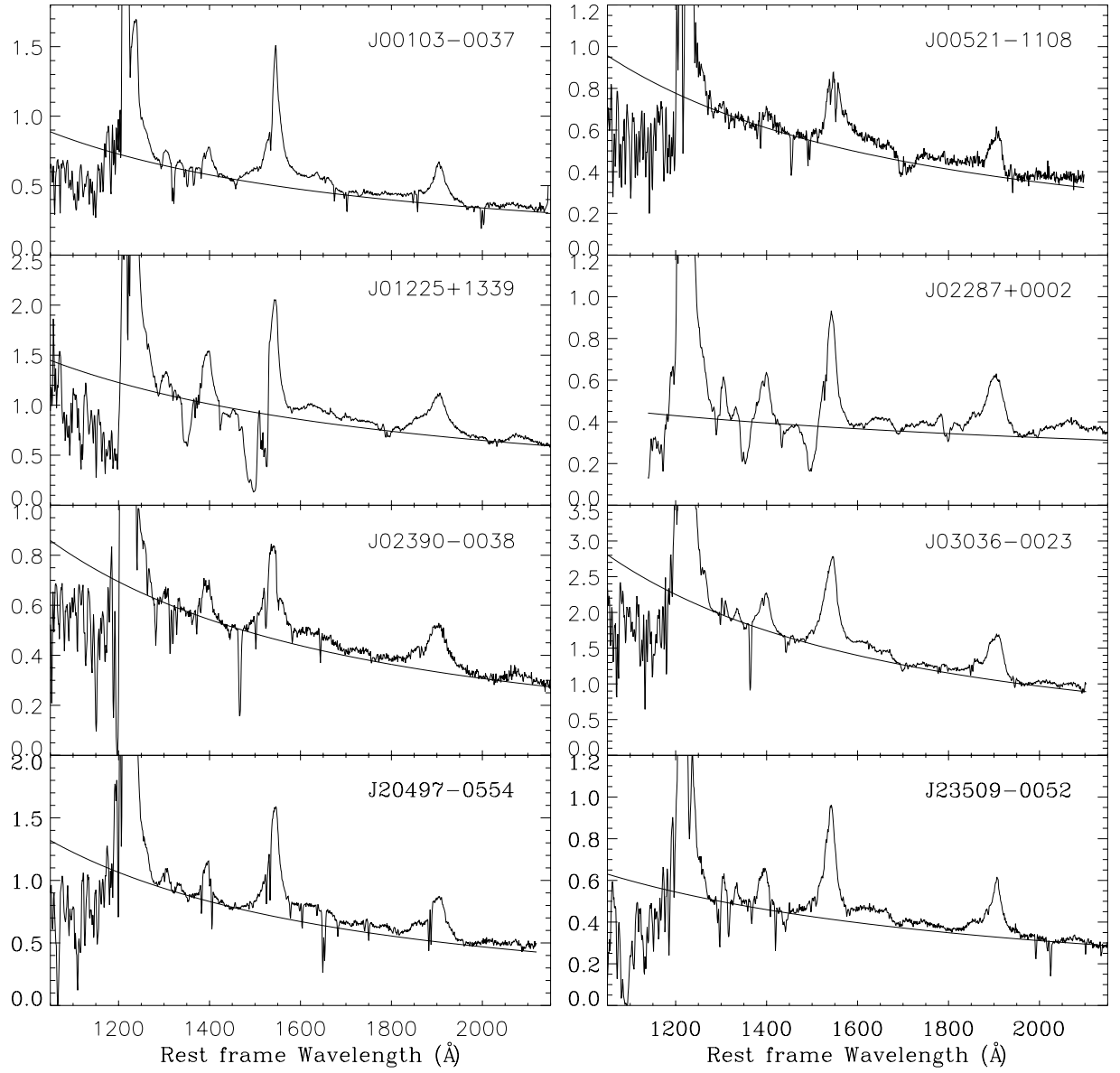


Fig. 3.— Sample of 8 VLT spectra in rest frame wavelength. Abscissa is rest frame in \AA , ordinate is specific flux in the rest frame in units $10^{-13} \text{ ergs s}^{-1} \text{ cm}^{-2} \text{ \AA}^{-1}$.

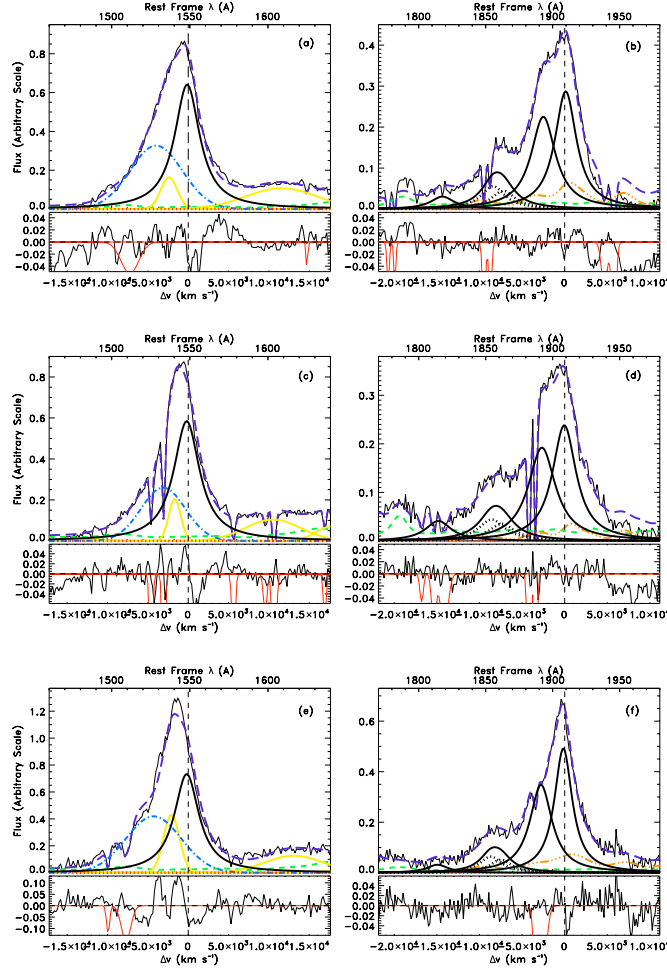


Fig. 4.— Fits for Pop. A objects: J03036-0023 (a, b), J20497-0554 (c, d), J23509-0052 (e, f). Upper panels show the fits and the lower pannels under the fits show the residuals and also the fitted absorptions lines. Upper abscissa is rest frame wavelength in Å, lower abscissa is in velocity units, ordinate is specific flux in arbitrary units. Vertical dashed line is the restframe for CIVλ1549 and CIII]λ1909. Long dashed line is the fit, solid dark lines are the broad components: CIVλ1549 in left panels and CIII]λ1909, SiIII]λ1892, AlIIIλ1860, SiIIIλ1814 in right panels. Dotted dark lines under AlIIIλ1860 show the doublet. Short dashed line is FeII. FeIII is shown in dash-triple-dot line in the right panels. Dash-dot line in the left panels is the blue-shifted component of CIVλ1549 while dotted line is the very broad component, present also in CIII]λ1909 for Pop. B objects. In the left panels we show with faint lines the contribution of NIVλ1486, SiIIIλ1533 and HeIIλ1640 core and blue-shifted components. For colors see online figures.

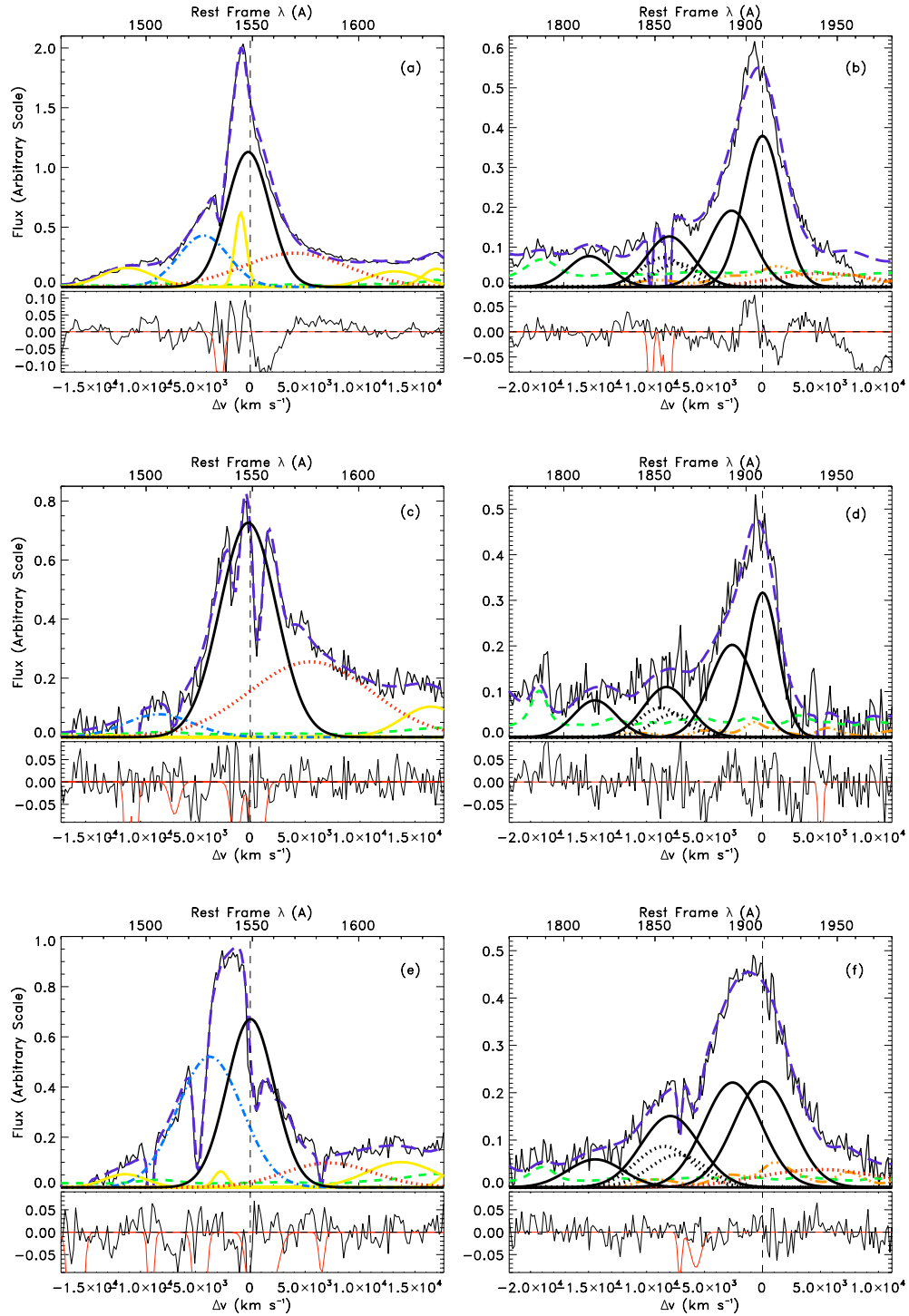


Fig. 5.— Fits for Pop. B objects: up J00103-0037, middle J00521-1108, low J02390-0038. Units and meaning of symbols are the same of Fig. 4.

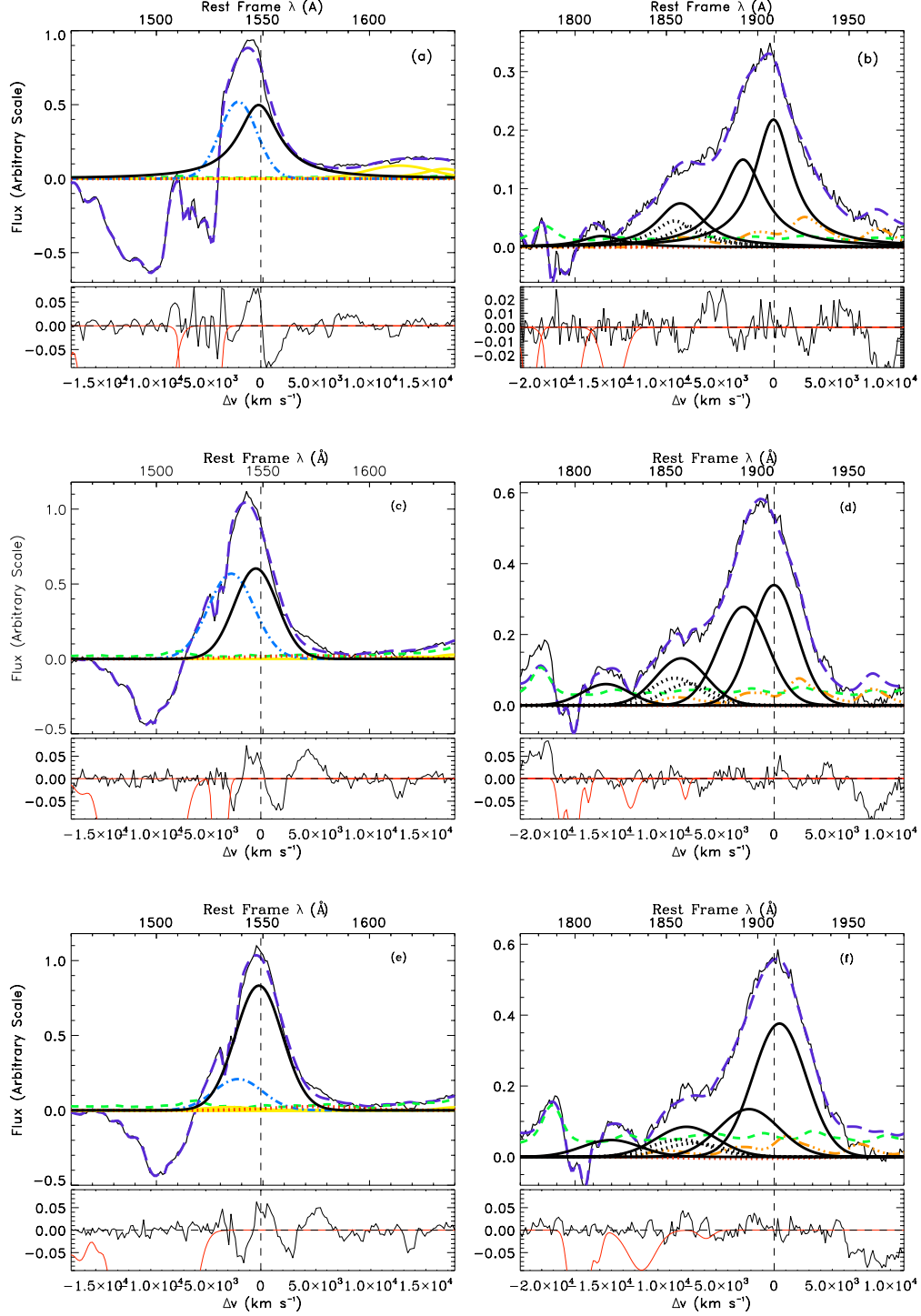


Fig. 6.— Fits for BAL quasars: up J01225+1339, middle J02287+0002 using $z_{\text{O}i\lambda 1304}$ rest frame, low J02287+0002 using $z_{\text{C}iii\lambda 1909}$ rest frame. Note in J02287+0002 the line displacement with the consequently line intensity changes, specially in CIII] λ 1909, SiIII] λ 1892 and CIV λ 1549 broad and blue-shifted components. Units and symbols are the same as in Fig. 4.

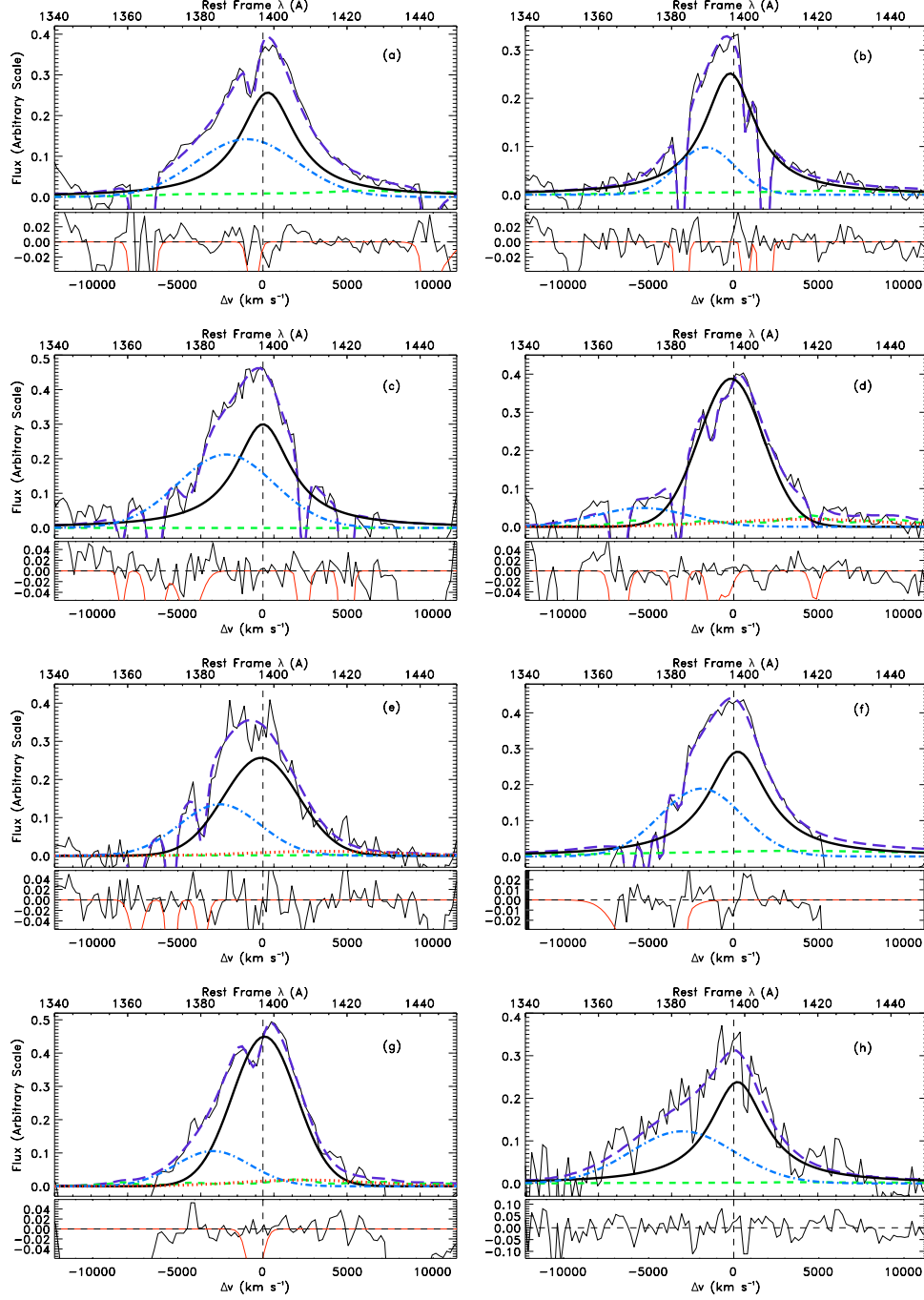


Fig. 7.— Fits for Si IV $\lambda 1397$: (a) J03036-0023, (b) J20497-0554, (c) 23509-0052, (d) J00103-0037, (e) J02390-0038, (f) J01225+1339, (g) J02287+0002 and (h) J12014+0116. We do not measure Si IV $\lambda 1397$ for J00521-1108 and 3C 390.3 because they have low S/N. We assume that the profile of Si IV $\lambda 1397$ can be fitted with the same three possible components (core, blue-shifted and red-shifted) as in the case of C IV $\lambda 1549$. Units and symbols are the same as in Fig. 4.

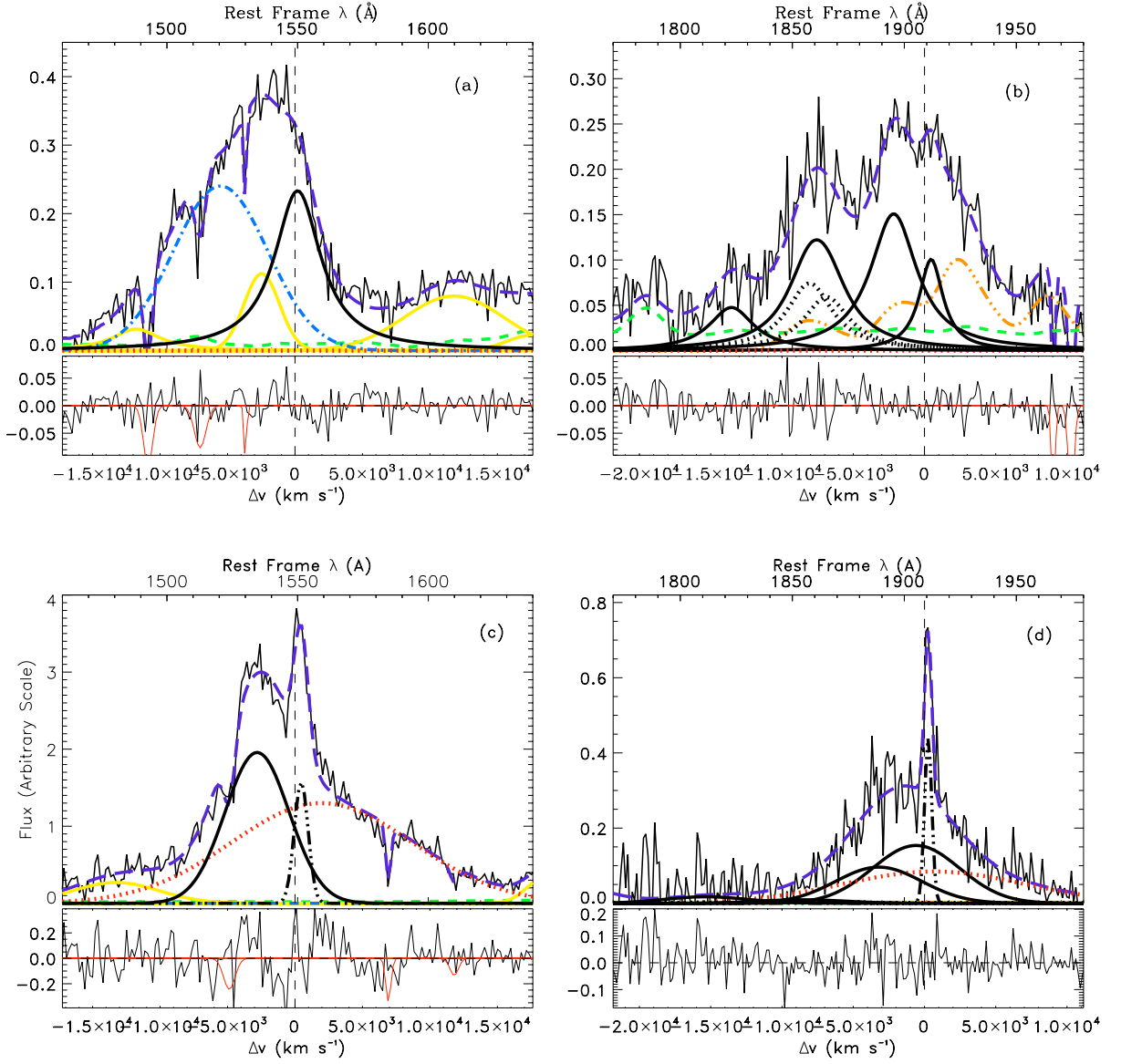


Fig. 8.— Fits for the two extreme objects: up J120144.36+011611.6, low 3C390.3. Units and meaning of symbols are the same of Fig. 4. For 3C390.3 it was needed to fit a narrow unshifted component that we show in dash-dot-dot line. Note for 3C390.3 SiII λ 1814 is almost absent.

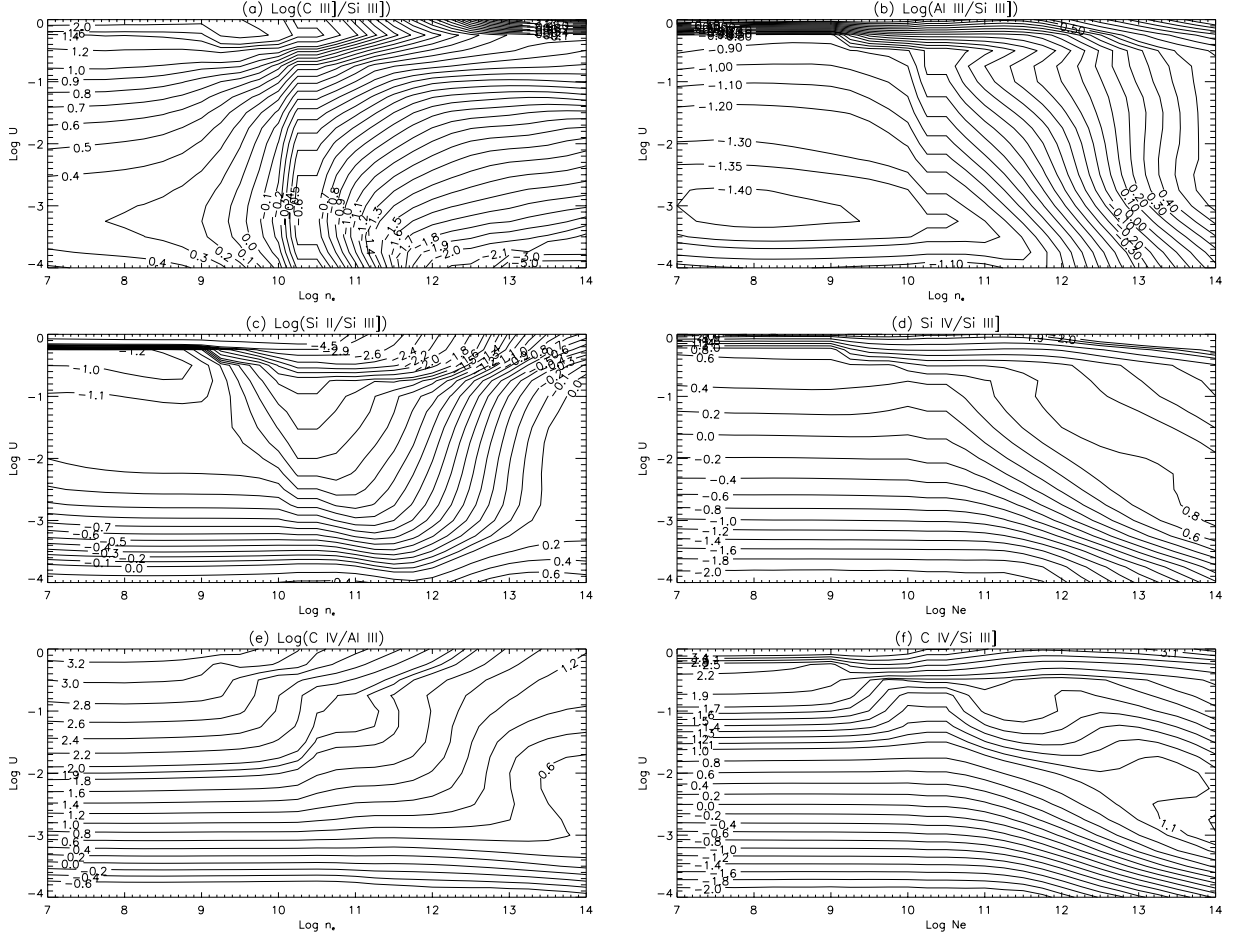


Fig. 9.— Isocontours for the ratios (a) $\log(\text{C III}] \lambda 1909 / \text{Si III}] \lambda 1892)$, (b) $\log(\text{Al III}] \lambda 1860 / \text{Si III}] \lambda 1892)$, (c) $\log(\text{Si II}] \lambda 1814 / \text{Si III}] \lambda 1892)$, (d) $\log(\text{Si IV} \lambda 1397 / \text{Si III}] \lambda 1892)$, (e) $\log(\text{C IV}] \lambda 1549 / \text{Al III}] \lambda 1860)$, and (f) $\log(\text{C IV}] \lambda 1549 / \text{Si III}] \lambda 1892)$ derived from CLOUDY simulations. Abscissa is electron density in cm^{-3} , ordinate is the ionization parameter, both in logarithm scale.

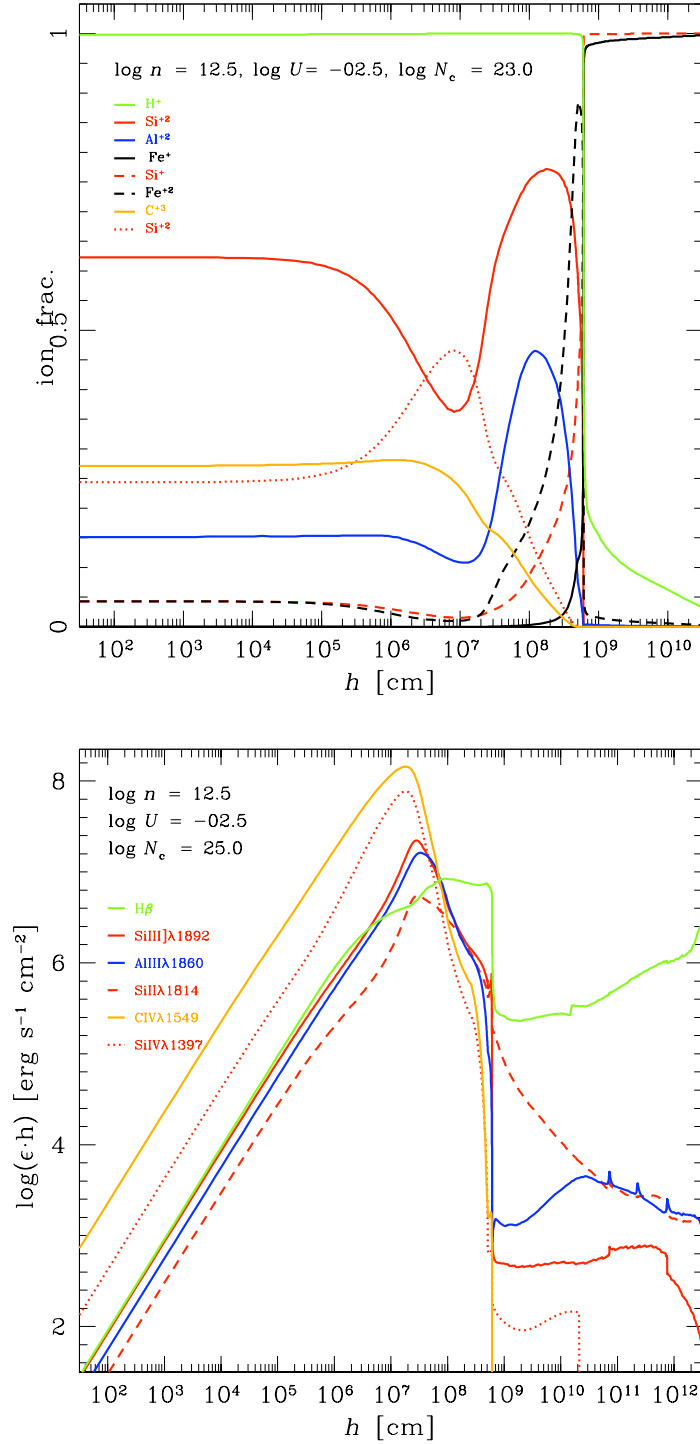


Fig. 10.— Top: Ionic Fractions as a function of the geometric depth h in the gas slab. Bottom: Line emissivity per unit volume in units of $\text{ergs s}^{-1} \text{ cm}^{-3}$ multiplied by depth.

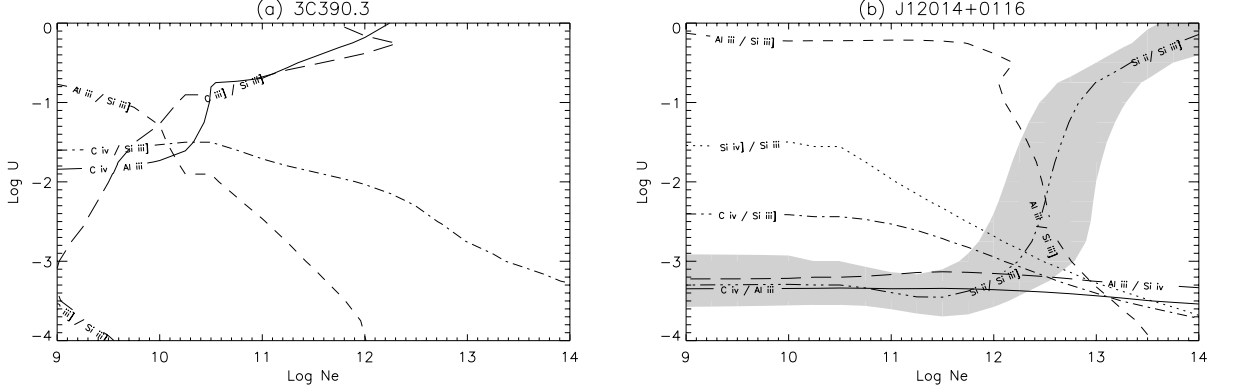


Fig. 11.— Contour plots for the extreme objects (a) 3C390.9 and (b) J12014+0116. Abscissa is electron density in cm^{-3} , ordinate is the ionization parameter, both in logarithm scale. Solid line is for $\log(\text{C IV } \lambda 1549 / \text{Al III } \lambda 1860)$, dot line is for $\log(\text{Si IV } \lambda 1397 / \text{Si III } \lambda 1892)$, dash line is for $\log(\text{Al III } \lambda 1860 / \text{Si III } \lambda 1892)$, long dash line is for $\log(\text{Al III } \lambda 1860 / \text{Si IV } \lambda 1909)$, dash dot line is for $\log(\text{C IV } \lambda 1549 / \text{Si III } \lambda 1892)$ and dash-triple-dot line is for $\log(\text{Si II } \lambda 1814 / \text{Si III } \lambda 1892)$. The point where the iso-contours cross determines the values of $\log n_e$ and $\log U$. The shaded area is the error bands for $\text{Si II } \lambda 1814$. In 3C390.3 we add a long dash line for $\log(\text{C III } \lambda 1909 / \text{Si III } \lambda 1892)$. In J12014+0116 the shaded area is the error bands for $\text{Si II } \lambda 1814$. See text for further details.

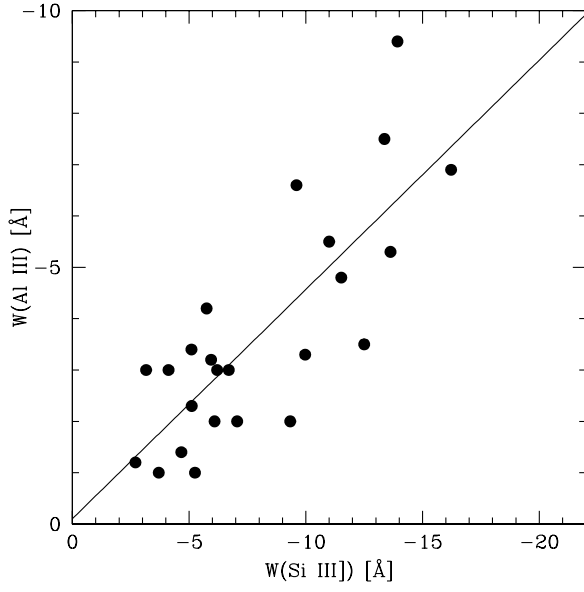


Fig. 12.— Correlation between rest frame equivalent width of AlIIIλ1860 and SiIIIλ1892. Line in unweighted least square best fit.

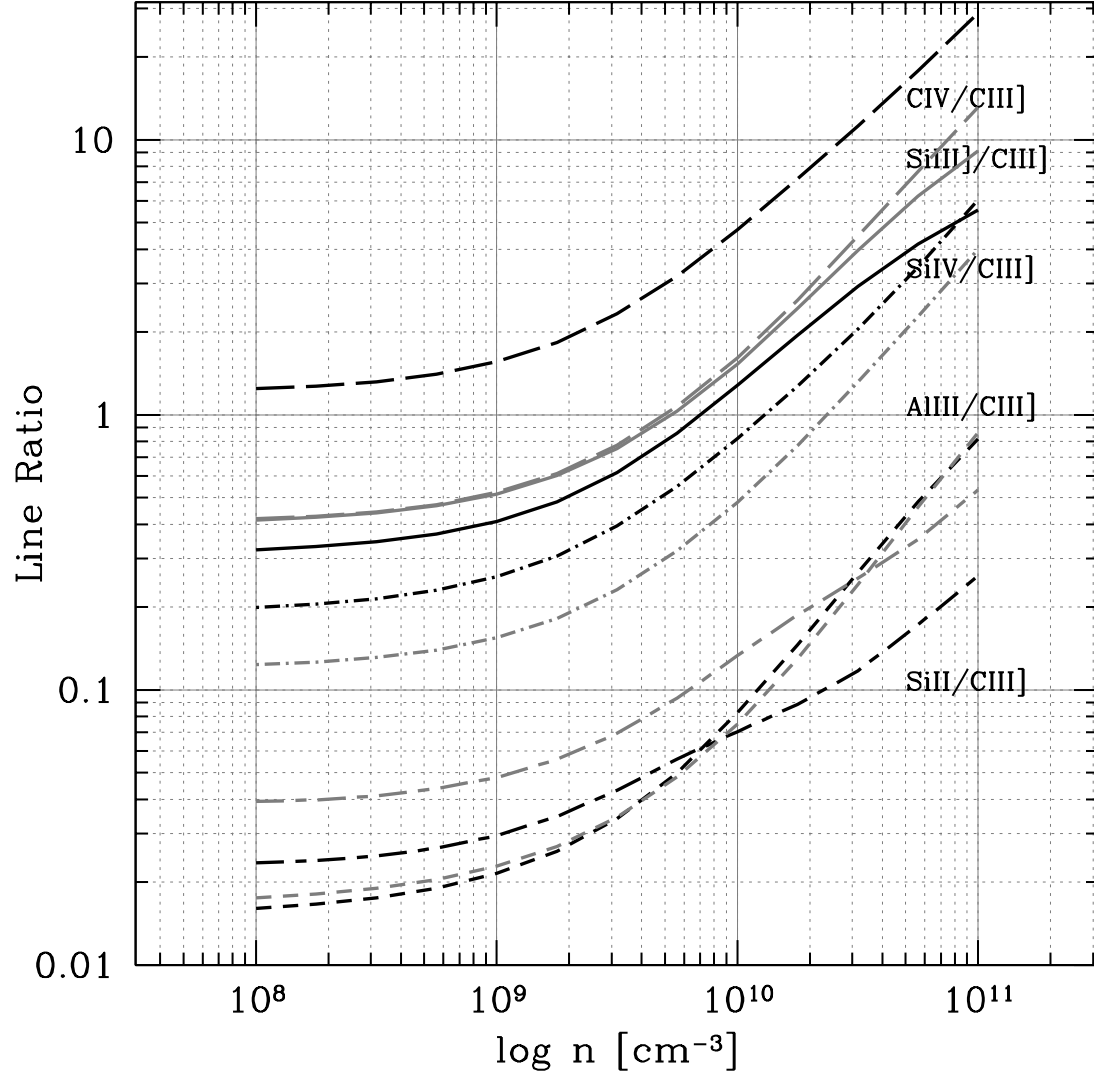


Fig. 13.— Expected contribution from moderate density emitting gas as a function of density for ionization parameters $\log U = -2$ (black lines) and $\log U = 2.5$ (grey lines).

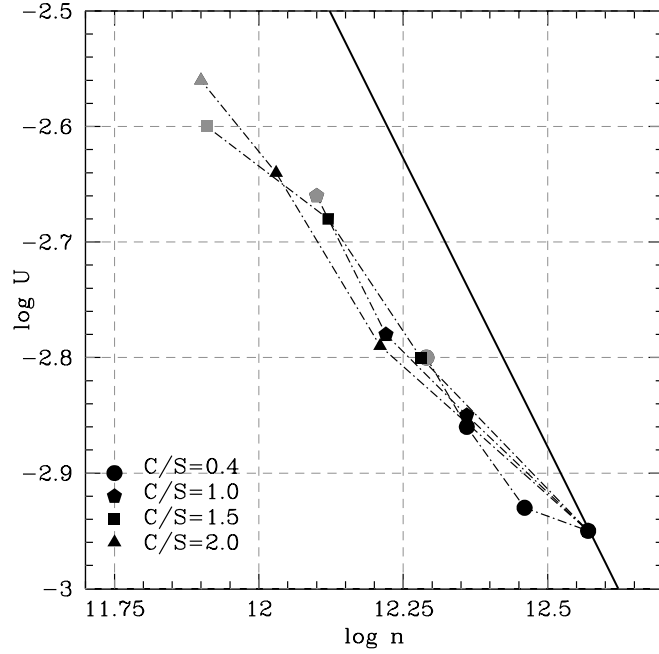


Fig. 14.— Plane $\log U - \log n$ in an expanded scale. The lower-left dot corresponds to a high density solution. Moderate density emitting gas is then added with increasing intensity of a $\text{CIII}] \lambda 1909$ component with the four $\text{CIII}] \lambda 1909 / \text{SiIII}] \lambda 1892$ ratios reported in the figure. Connected positions corresponds to increasing density of $\text{CIII}] \lambda 1909$ emitting gas, $\log n = 9, 9.5, 10$. Note that the case $\log n = 10$ (grey symbols) is not appropriate for the observed data.

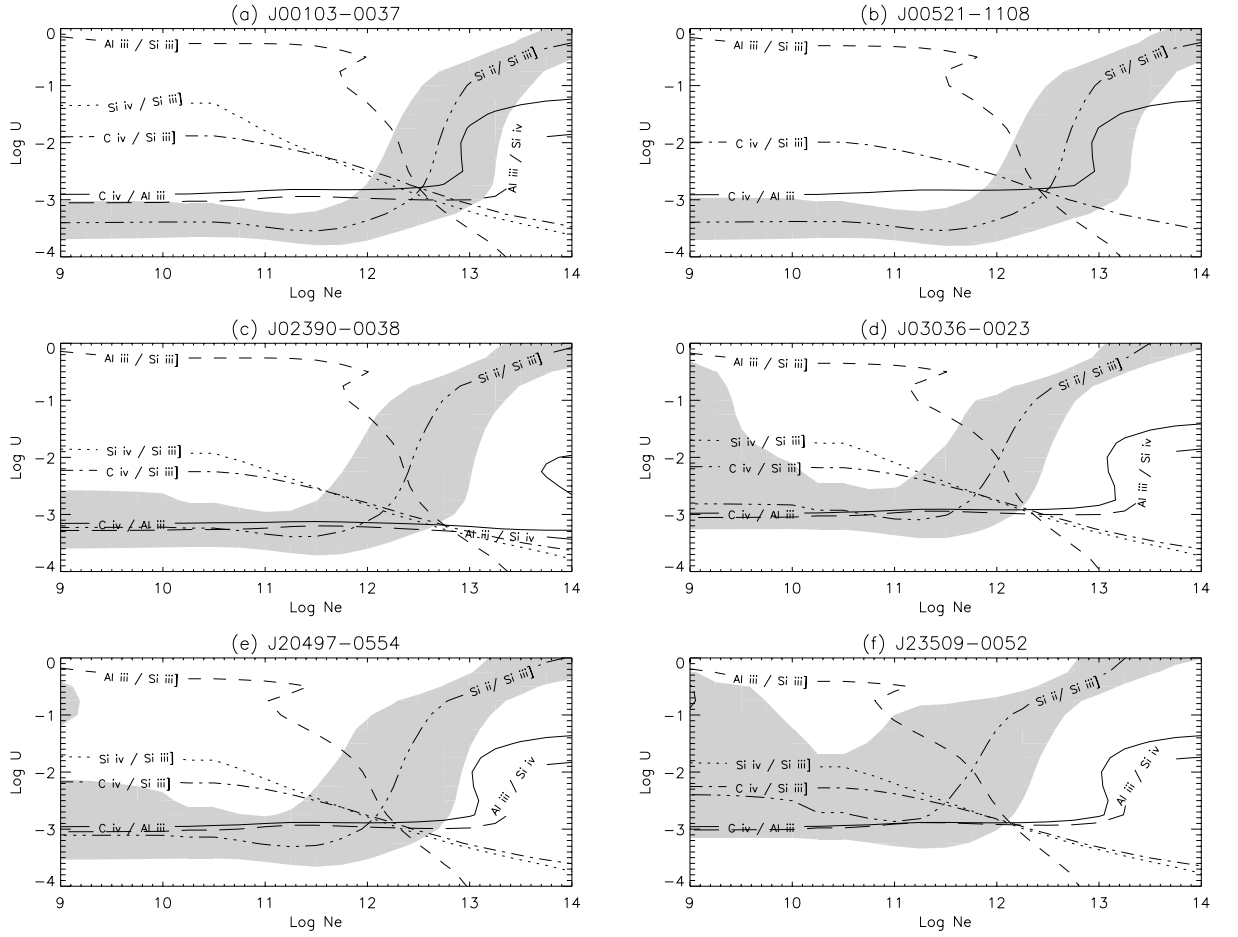


Fig. 15.— Contour plots for (a) J00103-0037, (b) J00521-1108, (c) J02390-0038, (d) J03036-0023, (e) J20497-0554 and (f) 23509-0052. Units and meaning of symbols are the same of Fig. 11. In the case of the objects shown in panels (c) and (f) the $\text{Si ii} \lambda 1814$ line is very weak and thus unreliable. For the objects in panels (a), (d) and (e) the line is also affected by the telluric absorption. For these objects we rely on the $\text{Si iv} \lambda 1397$ line.

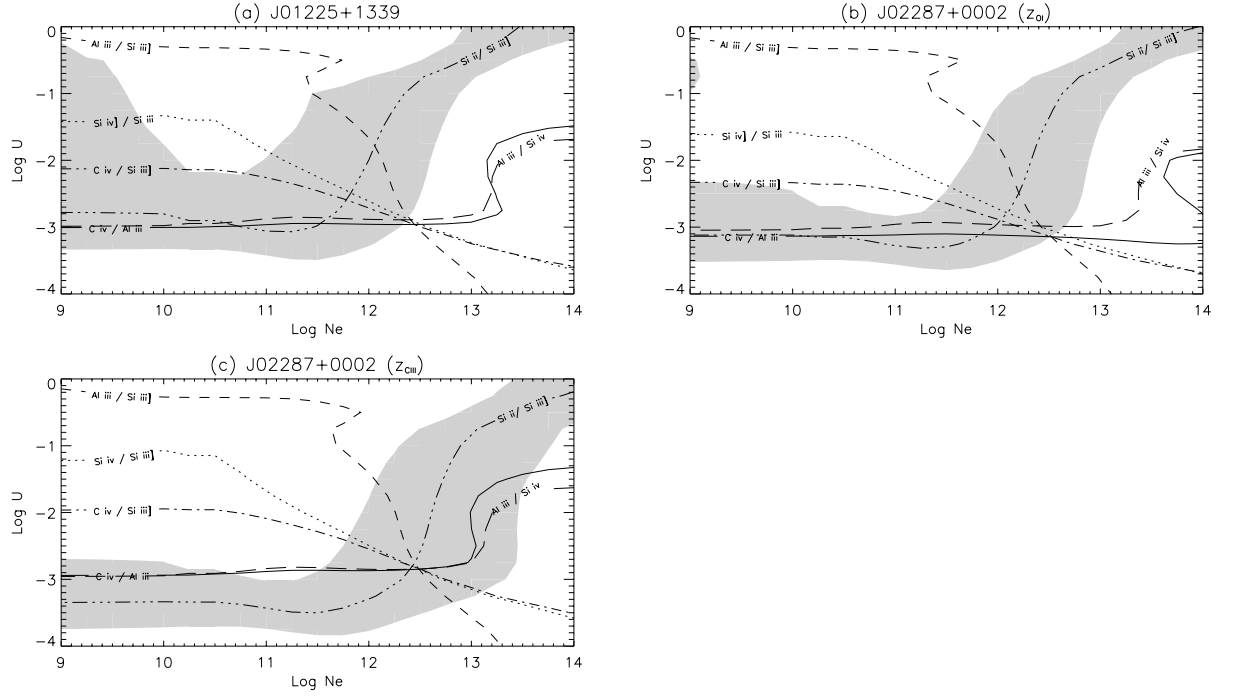


Fig. 16.— Contour plots for BAL quasars (a) J01225+1339 and (b) J01225+1339 using $z_{OI\lambda 1304}$ and (c) J01225+1339 using $z_{CIII\lambda 1909}$. Units and meaning of symbols are the same of Fig. 11.

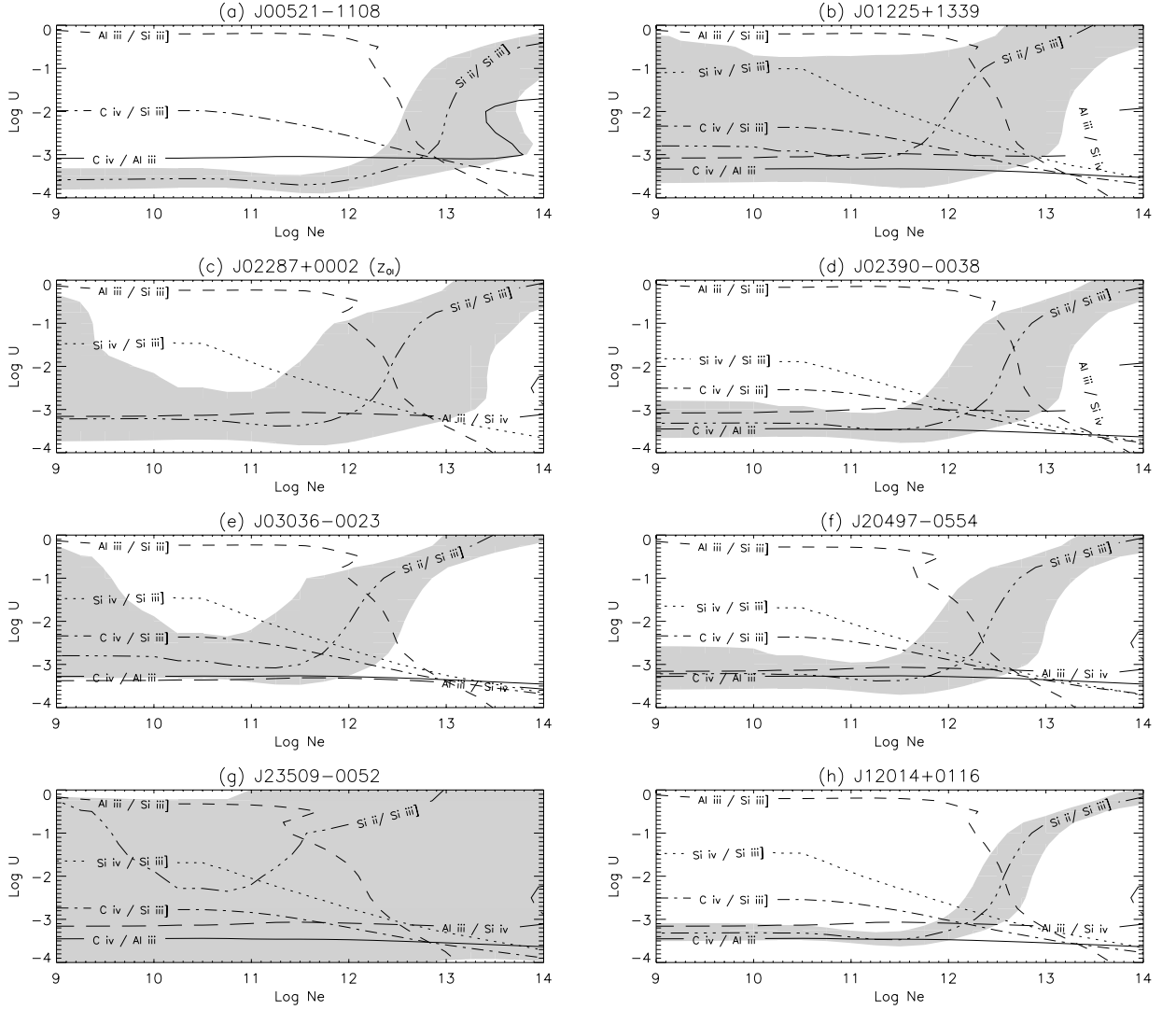


Fig. 17.— Contour plots for corrected values considering the low density emission contribution of $\text{CIII}\lambda 1909$. Contour plot for J00103-0037 is not shown because the correction is so large to be reliable. For the objects in panels (e) and (f) the $\text{SiII}\lambda 1814$ line is also affected by the telluric absorption. Abscissa, ordinate and symbols are the same as Fig. 11.

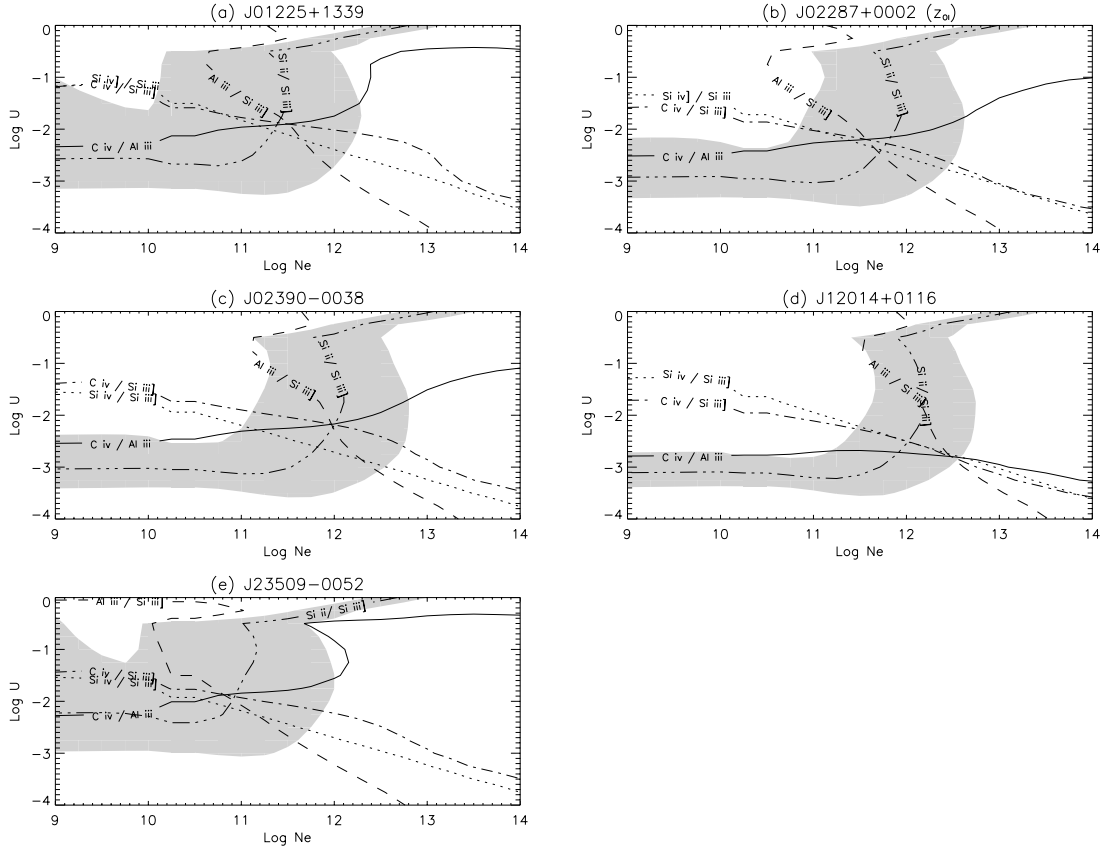


Fig. 18.— Contour plots for (a) J01225+1339, (b) J02287+0002 using $z_{\text{CIII}}]_{\lambda 1909}$, (c) J02390-0038, the extreme object (d) J12014+0116, and (e) J23509-0052, from the array of simulations computed for $Z = 5Z_{\odot}$. Coordinates and symbols are as for Fig. 11. The intersection point improves in certain cases, but in others is the same.

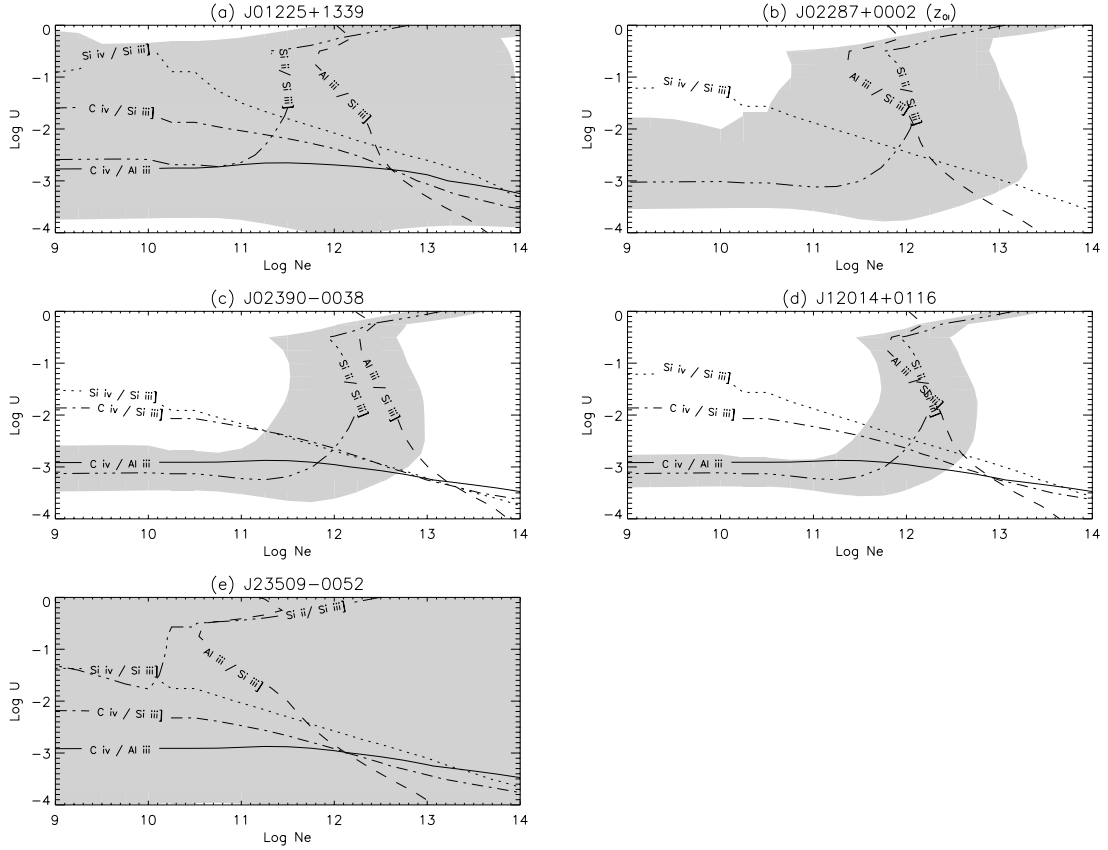


Fig. 19.— Contour plots for the same objects of the previous figure from the array of simulations computed for $Z = 5Z_\odot$ with ratios corrected because of low-density emission. Coordinates and symbols are as for Fig. 11.

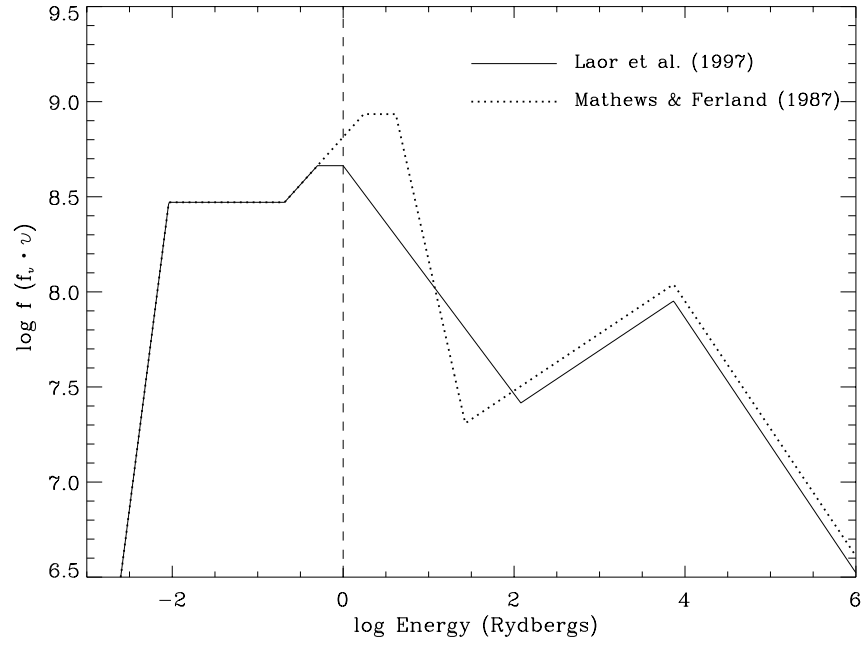


Fig. 20.— Spectral energy distribution used to compute the number of ionizing photons for Laor et al. (1997) in solid line and Mathews & Ferland (1987) in dotted line. Dashed line shows the Lyman limit.

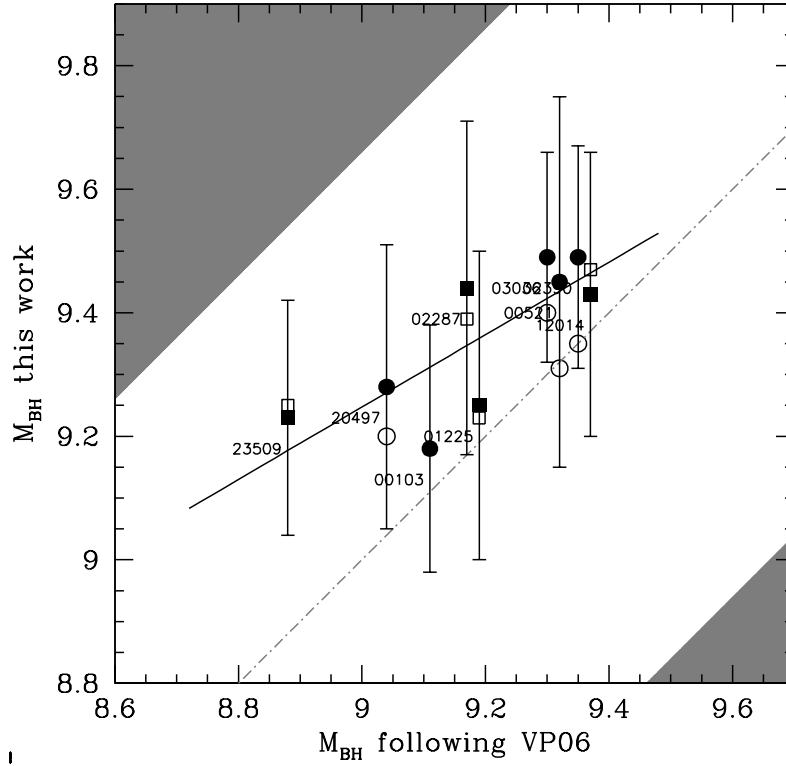


Fig. 21.— M_{BH} comparison for the high- z sample. Filled symbols refer to uncorrected intensity ratios; open symbols are for intensity ratios corrected because of low-density emission. Circles refer to solar metallicity; squares to 5 times solar metallicity and Si-Al enrichment. Abscissa and ordinate are logarithm of M_{BH} in solar masses. Each point is labeled with the object name in short format. In ordinate we report M_{BH} values obtained with the method of this paper; in abscissa those obtained employing the Vestergaard & Peterson relationship described in the text. The shaded bands limit the 2σ confidence level spread expected on the basis of the Vestergaard & Peterson relationship.